

1 Title: “Thermo-Chemical Dynamics in Earth’s Core Arising from Interactions with
2 the Mantle”.

3 Authors: Christopher J. Davies and Sam Greenwood, School of Earth and Environ-
4 ment, University of Leeds, Leeds LS2 9JT, UK.

5 This article is an invited review that has been submitted for publication to the AGU
6 Monograph “Core-Mantle Coevolution - A multidisciplinary approach”. It has not
7 yet undergone peer-review.

8 Thermo-Chemical Dynamics in Earth’s Core Arising from
9 Interactions with the Mantle

10 Christopher J. Davies^a, Sam Greenwood^a

11 ^a*School of Earth and Environment, University of Leeds, Leeds LS2 9JT, UK (tel: +44 (0) 113 34*
12 *31140; email: c.davies@leeds.ac.uk*

13 **Abstract**

Thermo-chemical interactions at the core-mantle boundary (CMB) play an integral role in determining the dynamics and evolution Earth’s deep interior. This review considers the processes in the core that arise from heat and mass transfer at the CMB, with particular focus on thermo-chemical stratification and the precipitation of oxides. A fundamental parameter is the thermal conductivity of the core, which we estimate as $k = 70 - 110 \text{ W m}^{-1} \text{ K}^{-1}$ at CMB conditions based on consistent extrapolation from a number of recent studies. These high conductivity values imply the existence of an early basal magma ocean (BMO) overlying a hot core and rapid cooling potentially leading to a loss of power to the dynamo before the inner core formed around 0.5 – 1 Gyrs ago, the so-called “new core paradox”. Coupling core thermal evolution modelling and calculations of chemical equilibrium between liquid iron and silicate melts suggests that FeO dissolved into the core after its formation, creating a stably stratified chemical layer below the CMB, while precipitation of MgO and SiO₂ was delayed until the last 2–3 Gyrs and was therefore not available to power the early dynamo; however, once initiated, precipitation supplied ample power for field generation. We also present a possible solution to the new core paradox without requiring precipitation or radiogenic heating using $k = 70 \text{ W m}^{-1} \text{ K}^{-1}$. The model matches the present inner core size and heat flow and temperature at the top of the

convecting mantle. It predicts a present-day CMB heat flow of 8.5 TW, a chemically stable layer 100 km thick, and a BMO lifetime of 2 Gyrs.

14 *Keywords:*

15 **1. Introduction**

16 The core-mantle boundary (CMB) accommodates one of the most significant
17 transitions in the structure and dynamics of the Earth system. The Preliminary
18 Reference Earth Model (PREM Dziewonski and Anderson, 1981) shows that the
19 horizontally-averaged density ρ and compressional wave speed V_p change by $\sim 40\%$
20 across the CMB. In terms of physical properties the lower mantle is a poor ther-
21 mal and electrical conductor and has a viscosity that is perhaps $10^{15} - 10^{20}$ times
22 larger than that of the core, which allows it to sustain temperature variations of
23 thousands of Kelvin and support large-scale dynamic structures such as the Large
24 Low Velocity Provinces (LLVPs) that sit on the CMB (e.g. Garnero et al., 2016).
25 The core, by contrast, is an excellent thermal and electrical conductor, while the low
26 viscosity, similar to that of water (Pozzo et al., 2013), implies that the bulk of the
27 core is undergoing turbulent convection. This stark contrast between structural and
28 dynamical properties leads to thermo-chemical interactions at the CMB that provide
29 power for generating the geomagnetic field and are important for determining the
30 long-term evolution of the core and mantle systems.

31 In this paper we review recent progress in understanding core mantle interactions
32 with a focus on the thermodynamics and fluid dynamics of the upper core; a comple-
33 mentary perspective from the mantle side can be found in Nakagawa (2020). Many
34 excellent reviews of the CMB region already exist and so we focus on the main devel-
35 opments since the authoritative Treatise on Geophysics reviews by Nimmo (2015a,b);
36 Buffett (2015); Hernlund and McNamara (2015) and Jaupart et al. (2015). Relevant

37 background on geodynamo simulations has also been recently reviewed by Wicht and
38 Sanchez (2019). To ensure a concise presentation we further focus on thermal and
39 chemical interactions. Core-mantle interactions also influence the rotational dynam-
40 ics of the Earth, a topic that was reviewed by Tilgner (2015) and more recently by
41 Dumberry (2018), and the shape of the core-mantle boundary, which has recently
42 been discussed in connection with the anomalously low (Koelemeijer et al., 2017)
43 or high (Lau et al., 2017) density of LLVPs. Here we will assume that the CMB is
44 spherical and that the core and mantle are co-rotating.

45 The dynamo process that maintains the geomagnetic field is ultimately driven by
46 heat extracted across the CMB. Syntheses of paleointensity data show that the field
47 has been continuously generated for at least the last 3.5 Gyrs (Tarduno et al., 2010;
48 Biggin et al., 2015; Tauxe and Yamazaki, 2015; Bono et al., 2019), while recordings
49 dating back to 4.2 Ga (Tarduno et al., 2015) are currently debated (Tang et al., 2019;
50 Tarduno et al., 2020). Heat loss at the CMB drives vigorous convection that main-
51 tains the bulk core in a state close to adiabatic temperature and uniform composition
52 (e.g. Braginsky and Roberts, 1995; Nimmo, 2015a). Compared to the mean CMB
53 temperature of ~ 4000 K (Lay et al., 2009; Davies et al., 2015) the thermal anomalies
54 associated with core convection are $O(10^{-3})$ K (Stevenson, 1987; Bloxham and Jack-
55 son, 1990), while the convective chemical anomalies are many orders of magnitude
56 smaller than the mean light element mass fraction of ~ 10 wt%. Consequently, even
57 small thermo-chemical anomalies resulting from interactions at the CMB can have a
58 significant effect on core dynamics.

59 The dynamics that result from thermo-chemical core-mantle coupling are dictated
60 by the fluxes of heat and mass at the CMB. The total CMB heat flow Q^c is poorly
61 constrained even for the present day, with current estimates suggesting the range
62 $Q^c = 7 - 17$ TW (Lay et al., 2009; Nimmo, 2015a), which amounts to $\sim 15 - 50\%$ of

63 Earth’s total heat budget (Jaupart et al., 2015). Back in time Q^c must be inferred
 64 from numerical models of mantle dynamics (Jaupart et al., 2015; Nakagawa, 2020).
 65 The key quantity for core dynamics is the superadiabatic heat flow $Q^c - Q_a^c$. The
 66 adiabatic heat flow on the core side of the CMB (radius $r = r_c$) is

$$Q_a^c = -4\pi r_c^2 k^c \left. \frac{\partial T_a^c}{\partial r} \right|_{r=r_c}, \quad (1)$$

where T_a is the adiabatic temperature, k^c is the thermal conductivity and superscripts
 c and m denote quantities on the core and mantle side of the CMB respectively
 (parameter values are given in Table 2). The total heat flow on the core side of the
 CMB is

$$Q^c = -4\pi r_c^2 k^m \left. \frac{\partial T^m}{\partial r} \right|_{r=r_c} - 4\pi r_c^2 [R_i^c - R_i^m] \mathbf{n} \cdot \mathbf{i}_i$$

$$Q^c = Q^m + Q_h \quad (2)$$

67 (Davies et al., 2020), where \mathbf{i}_i is the mass flux per unit area of element i (e.g. Mg, Si,
 68 O), \mathbf{n} is the outward unit normal to the CMB and $[R_i^c - R_i^m] < 0 (> 0)$ is the amount
 69 of heat released (absorbed) as one formula unit of i is transferred from the core to the
 70 mantle or vice versa (Pozzo et al., 2019). Here $R_i = \mu_i - T(\partial\mu_i/\partial T)_{P,T}$ is the heat of
 71 reaction coefficient with μ_i the chemical potential of element i and P the pressure.
 72 If the heat of reaction $Q_h < 0$, corresponding for example to an exothermic reaction
 73 with accompanying mass transfer into the core ($\mathbf{n} \cdot \mathbf{i} < 0$) then the heat flow available
 74 to core convection is reduced below the heat Q^m conducted through the lower mantle
 75 boundary layer, while $Q_h > 0$ acts as a heat source, increasing Q^c for a given Q^m . If
 76 $Q^c > Q_a^c$ then thermal convection probably occurs throughout the core. Conversely,
 77 if $Q^c < Q_a^c$ then a thermally stratified layer exists below the CMB in which heat

78 is transported by conduction and vertical motion is strongly impeded. Depending
 79 on the radial variation of $k(r)$ and the distribution of buoyancy sources within the
 80 core, which are both uncertain at present, it is possible to produce stratification at
 81 intermediate depths (Gomi et al., 2013). In this review we will mainly consider the
 82 case where stratification arises directly below the CMB.

83 The total chemical flux I_i of species i at the CMB is given by

$$I_i = -4\pi r_c^2 \rho D_i \left. \frac{\partial w_i^c}{\partial r} \right|_{r=r_c} + 4\pi r_c^2 \alpha_i^c \alpha_i^D g, \quad (3)$$

84 where D_i , w_i^c , α_i^c and α_i^D are respectively the self-diffusion coefficient, mass fraction,
 85 compositional expansion coefficient and barodiffusion coefficient of species i and g
 86 is radial gravity. Unlike the heat flux, I_i is continuous at the CMB if the small
 87 effect of core contraction is neglected (Gubbins et al., 2003; Davies et al., 2020). In
 88 equation (3) the second term on the right-hand side is the barodiffusion, representing
 89 transport of light element down the hydrostatic pressure gradient $dP/dr = -\rho g$,
 90 while element transport along the temperature gradient (thermodiffusion) is small
 91 and has been omitted (Gubbins et al., 2004). I is very hard to estimate because
 92 global mass balance constrains the bulk chemical composition of the core and mantle
 93 but not the compositional gradient at the CMB. Therefore much recent work has
 94 focused on establishing the equilibrium chemical conditions at the CMB, which relate
 95 compositions on either side of the interface (e.g. Fischer et al., 2015; Badro et al.,
 96 2018; Pozzo et al., 2019). If $I_i < 0$ then light elements leave the mantle, which
 97 almost certainly results in chemical stratification below the CMB since the chemical
 98 anomalies associated with core convection are minute and are hence unable to mix
 99 the anomalously light fluid downwards (Buffett and Seagle, 2010; Davies et al., 2018,
 100 2020). Conversely, $I_i > 0$ implies that light elements precipitate out of solution

101 (as oxides) and underplate onto the base of the mantle; the residual fluid, slightly
102 iron-rich compared to the fluid below, will sink via Rayleigh-Taylor instability thus
103 helping to drive core flow (O’Rourke and Stevenson, 2016).

104 The lower mantle is thermally and chemically heterogeneous and so heat and
105 mass exchange should vary with location on the CMB. Lateral variations in CMB
106 heat flow are expected from seismic tomography and geodynamic simulations (see for
107 example Gubbins, 2003; Olson et al., 2015, for reviews), which drive baroclinic flows
108 at the top of the core (e.g. Zhang, 1992) that might affect the observed magnetic
109 field (Gubbins et al., 2007; Aubert et al., 2007). CMB heat flow heterogeneity can
110 also alter a pre-existing stable layer (e.g. Olson et al., 2017; Christensen, 2018; Cox
111 et al., 2019) or even induce regional stratification if the anomalies are strong enough
112 to make the heat flow locally subadiabatic (Olson et al., 2018; Mound et al., 2019).
113 Lateral variations in chemical flux also seem likely if LLVPs are compositionally
114 distinct (Garnero et al., 2016), though this effect does not appear to have been
115 studied to date.

116 The existence of stratification and/or precipitation has important implications for
117 the dynamics and evolution of the core. Stratified layers suppress radial motion and
118 may support strong toroidal fields (Hardy et al., 2020) and distinct classes of wave
119 motions (Braginsky, 1999) that are observed as periodic variations of the geomagnetic
120 field (Buffett, 2014; Buffett et al., 2016). Such a layer also acts to filter the field that
121 is generated in the bulk core (Christensen, 2006; Gastine et al., 2020), effectively
122 filtering our view of the dynamo process, which is primarily based on observations
123 that only probe CMB field. Precipitation has recently been advocated as the primary
124 long-term power source for Earth’s magnetic field (O’Rourke and Stevenson, 2016;
125 Hirose et al., 2017), while precipitation products may have been incorporated into the
126 mantle via Rayleigh-Taylor instability (Helfrich et al., 2018). However, at present,

127 a definitive observation of either stratification or precipitation is lacking. Therefore,
128 in this review we focus on predictions from modelling studies, such as the thickness
129 and strength of stratification and the thermal and magnetic history of the core, that
130 add further constraints to complement the observational evidence.

131 Broadly speaking, there are presently 2 scenarios for thermo-chemical core-mantle
132 interactions that depend to a large extent on the core thermal conductivity k (see
133 Table 1). In the “low conductivity” scenario the core cooled slowly over geological
134 time, powering the geomagnetic field by thermal convection until the onset of inner
135 core freezing around 1 billion years ago, which provided additional power for field
136 generation through release of latent heat and light elements (e.g. Buffett et al., 1996;
137 Labrosse et al., 2001; Gubbins et al., 2003, 2004; Nimmo et al., 2004). Due to the low
138 conductivity the present adiabatic heat flow is predicted to be around 4 – 6 TW and
139 hence thermal convection probably operated throughout the core until the present-
140 day. In this scenario, thermal history models indicate that the core temperature
141 remained below the mantle solidus over the last 4 Gyrs, though a Basal Magma
142 Ocean (BMO Labrosse et al., 2007) could still have formed via mantle crystallisation
143 that proceeded from the middle outwards (Stixrude et al., 2009). With low k , models
144 predict that the BMO can survive to the present-day while still providing enough
145 power to the geodynamo (via Q^c) to sustain the magnetic field (Blanc et al., 2020).
146 This situation would facilitate efficient long-term chemical exchange between the core
147 and mantle owing to the much higher self-diffusion coefficients of chemical species in
148 the liquid (e.g. Adjaoud et al., 2011; Posner et al., 2018; Caracas et al., 2019).

149 The second scenario for thermo-chemical core-mantle evolution corresponds to a
150 high thermal conductivity exceeding around $90 \text{ W m}^{-1}\text{K}^{-1}$. In order to maintain
151 the geomagnetic field for the last 3.5 Gyrs the core must cool faster to offset the
152 enhanced power losses from thermal conduction, leading to an estimated inner core

153 age of $\sim 0.5-0.7$ Gyrs (Driscoll and Bercovici, 2014; Davies, 2015; Davies et al., 2015;
154 Labrosse et al., 2015; Nimmo, 2015a). The high conductivity values predict $Q_a^c = 14-$
155 16 TW, comparable to the upper estimates of Q^c at the present day and suggesting
156 thermal stratification of the upper core. Rapid cooling further implies early core
157 temperatures that far exceeded current estimates of the lower mantle solidus and
158 hence the presence of a BMO. However, since release of latent and radiogenic heat
159 in the BMO stifled heat loss from the core (Labrosse et al., 2007), maintaining the
160 early magnetic field with high k may require that the BMO was short-lived (Davies
161 et al., 2020).

162 The major problem posed by the high conductivity scenario is illustrated by
163 parameterised models of coupled core-mantle evolution (Driscoll and Bercovici, 2014;
164 O’Rourke et al., 2017) and could have been appreciated from the early study by
165 Nimmo et al. (2004). With high k , classical parameterised mantle evolution models
166 based on boundary layer theory predict an approximately exponential decline in CMB
167 heat flow over time, which can lead to a loss of power to the dynamo before inner
168 core nucleation around 1-2 Ga, in contradiction with paleomagnetic data (Biggin
169 et al., 2015; Bono et al., 2019). However, the obvious remedy, increasing CMB heat
170 flow and hence core cooling rate, leads to an old inner core that grows larger than
171 its present size as determined by seismology. The apparent contradiction between
172 observations and the fundamental model of core evolution has been termed the “new
173 core paradox”. The term “paradox” is used because higher k generally implies higher
174 electrical conductivity in metals (Chester and Thellung, 1961) and hence weaker
175 magnetic diffusion, which should be beneficial to dynamo action. Driscoll and Du
176 (2019) show that the ratio of magnetic induction to diffusion declines in both high
177 and low electrical conductivity limits and suggest that Earth’s core came close to
178 this “no dynamo” state prior to inner core nucleation. Thermal history models have

	low conductivity	high conductivity
k	$\lesssim 50 \text{ W m}^{-1}\text{K}^{-1}$	$\gtrsim 90 \text{ W m}^{-1}\text{K}^{-1}$
Q_a^c	4 – 6 TW	14 – 16 TW
Core cooling rate	Slow	Fast
Inner core age	~ 1 Gyr	~ 0.5 Gyrs
Thermal stratification	Never	Likely at present
Basal magma ocean (BMO)	Maybe, possibly long-lived	Likely, probably short-lived
Pre-inner core dynamo power	Secular cooling	Secular cooling, but precipitation maybe also required
Chemical exchange	Efficient with BMO	Efficient only in early times

Table 1: Two scenarios for core-mantle evolution described in the text. The CMB heat flow is estimated as $Q^c = 7 - 17$ TW (Nimmo, 2015a).

179 attempted to overcome the new core paradox by invoking additional effects such as
180 a significant amount of radiogenic heating (e.g. from ^{40}K , Driscoll and Bercovici,
181 2014) or gravitational power provided by the precipitation of MgO (O’Rourke et al.,
182 2017) or SiO_2 (Hirose et al., 2017), though the viability of all of these processes has
183 been questioned (Xiong et al., 2018; Du et al., 2019; Arveson et al., 2019).

184 In this review we first discuss the material properties of the core that are required
185 to model the processes of stratification and precipitation, focusing on the composi-
186 tion on either side of the CMB and the core thermal conductivity (Section 2). This
187 motivates us to consider the high conductivity scenario in the remainder of the re-
188 view. In section 3 we describe recent studies of core-mantle chemical equilibrium and
189 discuss constraints on the onset and rate of chemical precipitation and stratification
190 below the CMB. Section 4 reviews thermal and chemical stratification at the top of
191 the core, while Section 5 discusses recent studies of chemical precipitation. Finally,
192 in Section 6 we discuss potential resolutions to the “new core paradox”.

193 2. Material Properties of the Core

194 The dynamics and evolution of the CMB region are intimately linked to pro-
195 cesses in the bulk core. The standard tools used to investigate core evolution on Gyr
196 timescales are thermal history models, which are 2D (radius and time) parameteri-
197 sations of the complex 4D processes that arise in direct numerical simulation (DNS)
198 of core dynamics. The primary constraints on these models, and the predictions of
199 stratification and precipitation processes they make, are 1) the continuous generation
200 of a magnetic field for at least the last 3.5 Gyrs (Tarduno et al., 2010) and; 2) to match
201 the present-day radius r_i of the inner core, $r_i = 1221$ km. Therefore constraining
202 the evolution of the CMB region requires knowledge of the material properties of the
203 whole core. The growth rate of the inner core depends on the rate at which the core
204 cools and also the slopes of the melting temperature T_m and ambient temperature
205 T of the core alloy. The power available to the dynamo depends on many factors,
206 including the cooling rate and the thermal conductivity k .

207 The challenge of estimating core material properties arises from the extreme
208 conditions that must be replicated. The pressure ranges from $P = 135$ GPa to
209 $P = 330$ GPa across the core (Dziewonski and Anderson, 1981), T is several thou-
210 sands of Kelvin, while the mass fractions w_i^c of light element i are themselves de-
211 termined by partitioning behaviour at high P and T . The main experimental tool
212 used to access these conditions is the laser-heated diamond anvil cell. Here the
213 challenges include minimising temperature gradients across small samples (Sinmyo
214 et al., 2019), identifying melting (Anzellini et al., 2013), and the potential for ox-
215 idation of the sample at high $P - T$ (Frost et al., 2010). *Ab initio* calculations
216 can sample core $P - T$ conditions, but also contain uncertainties such as the form
217 of the exchange-correlation functional and must ultimately be ground-truthed by

218 experiments. Hence, determinations of core properties do come with appreciable
219 uncertainties. In this review we will explicitly discuss uncertainties arising in deter-
220 minations of core thermal conductivity and partitioning behaviour, but we will not
221 provide a systematic survey of all parameters. We will also focus on models of the
222 core that are consistent with seismic observations (Badro et al., 2014; Davies et al.,
223 2015).

224 Present-day constraints on P , T and w_i^c come from the liquid core density ρ ,
225 which is about 10 wt% lighter than pure iron, and also from the density jump $\Delta\rho$
226 at the inner core boundary (ICB, radius r_i). Fluctuations in ρ due to convection are
227 small (Stevenson, 1987) while time variations in core composition are tiny (Davies,
228 2015) and so the pressure gradient is determined from hydrostatic balance with ρ
229 and gravity g derived from 1D seismic models of the core (Dziewonski and Anderson,
230 1981; Irving et al., 2018). Part of the observed density jump, $\Delta\rho_m = 240 \text{ kg m}^{-3}$
231 (Alfè et al., 2002c), arises from the phase change at the ICB; the rest determines
232 the excess concentration of light elements in the liquid core compared to the solid
233 core. Matching candidate compositions derived from partitioning behaviour at ICB
234 conditions to observational constraints on $\Delta\rho$ allows to estimate the present core
235 composition and hence the melting temperature T_m of the iron alloy at the CMB (e.g.
236 Alfè et al., 2002a). The core temperature T is usually assumed to vary adiabatically
237 outside thin boundary layers and stable regions. The anchor point for T is the
238 value of T_m at the ICB. The chemical properties α_i^c , α_i^D and R_i are calculated from
239 chemical potentials at fixed P , T and composition. Finally, transport properties such
240 as the core viscosity ν , self-diffusion coefficients D_i and thermal conductivity can be
241 calculated for specified composition at points along core $P - T$ curves (e.g. Pozzo
242 et al., 2013).

243 The ICB density jump $\Delta\rho$ is rather uncertain (see Wong et al., 2021, for a recent

244 review). In this work we take the range obtained from normal modes of $\Delta\rho =$
245 $800 \pm 200 \text{ kg m}^{-3}$ (Masters and Gubbins, 2003) and consider the three values $\Delta\rho =$
246 600 kg m^{-3} , 800 kg m^{-3} and 1000 kg m^{-3} . The parameter values for each $\Delta\rho$
247 are listed in Table 2. These are generally taken from Davies et al. (2015) where
248 more details can be found. In the following subsections we review constraints on
249 the core and magma ocean compositions that are relevant for understanding mass
250 exchange at the CMB. We then consider the core temperature structure and sketch
251 a derivation of the core energy balance before discussing recent estimates of core
252 thermal conductivity.

253 *2.1. Bulk Composition of the Core and Basal Magma Ocean*

254 The composition of the core and the nature and abundance of mineral phases
255 at the base of the mantle are still rather uncertain at present (Hirose et al., 2013;
256 Garnero et al., 2016). Core formation models suggest that O, Si and S are likely to
257 partition into metal (Rubie et al., 2015a; Badro et al., 2015), though at very high
258 temperatures other elements such as Mg can also become siderophile (O’Rourke and
259 Stevenson, 2016). Carbon has also been considered (Rubie et al., 2015a), but recent
260 work suggests C partitions weakly into metal at high P and T (Fischer et al., 2020).
261 Calculations attempting to match the present-day core mass and $\Delta\rho$ show that O
262 and C partition almost exclusively into liquid at ICB conditions (Alfè et al., 2002a;
263 Li et al., 2019) and so matching the overall mass of the core requires another element
264 that partitions evenly such as S or Si (Alfè et al., 2002a). Hydrogen may also be
265 present if the core temperature is on the lower end of present estimates (Umemoto
266 and Hirose, 2020). The main stable phase in the present lower mantle is (Mg,Fe)SiO₃
267 silicate perovskite, with $\sim 15\%$ ferropericlase and some calcium silicate perovskite
268 (Garnero et al., 2016). Bridgmanite composition is dominated by the oxides SiO₂

Symbol	100%Fe	82%Fe-8%O-10%Si	79%Fe-13%O-8%Si	81%Fe-17%O-2%Si
$\Delta\rho$ (kg m ⁻³)	240	600	800	1000
w_{O}^{S}	-	0.0002	0.0004	0.0006
w_{Si}^{S}	-	0.0554	0.0430	0.0096
w_{O}^{L}	-	0.0256	0.0428	0.0559
w_{Si}^{L}	-	0.0560	0.0461	0.0115
C_p (J/kg/K)	715—800	-	-	-
$L(r_i)$ (MJ/kg)	0.75	-	-	-
$T_m(r_i)$ (K)	6350	5900	5580	5320
$\left.\frac{dT_m}{dP}\right _{r_i}$ (K/GPa)	9.01	9.01	9.01	9.01
$\alpha_T(r_i)$ ($\times 10^{-5}$ /K)	1.0	-	-	-
$T_a(r_c)$ (K)	4735	4290	4105	3910
$\left.\frac{\partial T_a}{\partial P}\right _{r_i}$ (K/GPa)	6.96	6.25	6.01	5.81
$\left.\frac{\partial T_a}{\partial r}\right _{r_c}$ (K/km)	-1.15	-1.03	-1.00	-0.96
k (W/m/K)	-	See	Text	-
D_{O} ($\times 10^{-8}$ m ² /s)	-	1.31	1.30	-
D_{Si} ($\times 10^{-8}$ m ² /s)	-	0.52	0.46	-
ν ($\times 10^{-7}$ m ² /s)	6.9	6.8	6.7	-
$\alpha_{\text{O}}^{\text{D}}$ ($\times 10^{-12}$ kg/m ³ s)	-	0.72	0.97	1.11
$\alpha_{\text{Si}}^{\text{D}}$ ($\times 10^{-12}$ kg/m ³ s)	-	1.19	1.10	40.6
		O	Si	
α_i^c	-	1.1	0.87	
$R^c - R^m$ (eV/f.u.)	-	-2.5		

Table 2: Core material properties for pure iron and three Fe-O-Si mixtures denoted by their molar concentrations in the header line. Superscripts c have been suppressed for clarity. Gravity g , pressure P and gravitational potential ψ are derived from the PREM density ρ . Quantities in the first section define the core chemistry model. Numbers in the second section determine the core temperature properties in the third section, which are given for the present day. The core temperature is assumed to follow an adiabat, denoted T_a , and the melting temperature of the core alloy is denoted T_m . L denotes the latent heat of fusion and α_T is the thermal expansion coefficient. CMB values for transport properties calculated along the corresponding adiabats are given in section four. The CMB radius is denoted $r_c = 3480$ km, the present-day ICB radius is $r_i = 1221$ km. α_i^c are the compositional expansion coefficients, $R^c - R^m$ is the heat of reaction coefficient [equation (2)] from Pozzo et al. (2019) and α_i^{D} is the barodiffusion coefficient [equation (3)] from Gubbins and Davies (2013). Adapted from Davies et al. (2015).

269 and MgO (Garnero et al., 2016).

270 Much recent work has focused on the partitioning of Mg, Si and O between the
271 core and mantle. Mg and Si are of interest because they may become saturated in the
272 core as the planet cools, precipitating as oxides MgO and SiO₂ respectively, which
273 releases gravitational energy that is available to power the geodynamo (O’Rourke
274 and Stevenson, 2016; Badro et al., 2016; Hirose et al., 2017; Mittal et al., 2020). The
275 study of FeO has attracted attention because it provides a mechanism for oxygen to
276 enter the core, either from FeO in ferropericlasite in the present Earth (Frost et al.,
277 2010) or from an FeO-enriched basal magma ocean in the past (Davies et al., 2020),
278 which leads to a stable stratification below the CMB (Buffett and Seagle, 2010;
279 Davies et al., 2020). We will therefore focus on the interactions between Fe, Mg, Si
280 and O in the remainder of this review. Note that the material properties listed in
281 Table 2 were obtained without Mg, though the error is probably not significant since
282 the fraction of Mg dissolved in the core is probably much less than Si or O.

283 The initial bulk compositions of the core and mantle were set during planetary
284 differentiation. Recent multi-stage core formation models find broadly consistent
285 initial oxygen concentrations in the range 2 – 5 wt% (Badro et al., 2015; Rubie
286 et al., 2015b), but diverge on the estimated silicon content with Badro et al. (2015)
287 finding 2 – 3.6 wt% Si while Rubie et al. (2015b) obtaining 8 – 9 wt% Si. The
288 difference is partly due to the inferred oxidation state (oxidising or reducing) of
289 accretion materials, though other uncertainties in the core formation process mean
290 that initial Si and O core concentrations in the range 1 – 10 wt% cannot be ruled
291 out (Fischer et al., 2017). Partitioning of Mg has generally been omitted in core
292 formation studies. Badro et al. (2016) ran multi-stage core formation models and
293 found 0.8 wt% MgO could be delivered to the core without a late giant impact, while
294 1.6 – 3.6 wt% MgO could be delivered depending on the mass of a late impactor.

295 O'Rourke and Stevenson (2016) estimated 0.5 wt% Mg in the core for a single stage
296 model with equilibration at 3500 K while a 2-stage model with second equilibration
297 at higher T permitted up to 2 wt% Mg in the core. Recently Helffrich et al. (2020)
298 estimated that 0.3 wt% Mg could be delivered via single-stage core formation. The
299 initial BMO composition is also hard to constrain. Andrault et al. (2017) conclude
300 that deep mantle melts near the eutectic temperature may have had compositions
301 similar to pyrolite, i.e. 40 mol% SiO₂, 50 mol% MgO and 10 mol% FeO (Eggins
302 et al., 1998). Caracas et al. (2019) calculate a change in melt composition between
303 0 and 30% melt fraction of 10 mol% SiO₂, 5 mol% MgO and 37 mol% FeO.

304 2.2. Core Temperature and Energy Balance

305 The temperature at the inner core boundary is obtained from the melting point of
306 pure iron, T_m^{Fe} , depressed by an amount ΔT to account for the presence of impurities.
307 In this work we take $T_m^{Fe} = 6360$ K from the *ab initio* study of Alfè et al. (2002a),
308 which is consistent with the experimental results of Anzellini et al. (2013), though
309 higher than recent estimates of 5500 K from Sinmyo et al. (2019). The gradient
310 of the melting curve, dT_m^{Fe}/dP is more important for thermal history calculations,
311 which is more consistent between the Sinmyo et al. (2019) and Anzellini et al. (2013)
312 studies when accounting for uncertainties in extrapolating the experimental results
313 to ICB pressure.

314 The effect of impurities on T_m is clearly hard to constrain given current uncer-
315 tainties on the core composition. Here we employ the linear melting point depression
316 derived by Alfè et al. (2002a) using a truncated expansion of the chemical potentials
317 at ICB conditions. The total ΔT is assumed to be a linear combination of the values
318 for O and Si (ignoring any effect from Mg).

319 The adiabatic temperature gradient is given by

$$\frac{\partial T_a}{\partial r} = -\frac{\alpha_T g T_a}{C_p}. \quad (4)$$

320 T_a is anchored to T_m at the ICB and calculated as a function of radius using the
 321 values of the thermal expansion coefficient α_T and specific heat capacity C_p quoted
 322 in Gubbins et al. (2003) and reported in Table 2. Gubbins et al. (2003) noted that
 323 cooling on the adiabat is independent of radius to a good approximation such that

$$\frac{DT_a}{Dt} = \frac{T_a}{T_c} \frac{dT_c}{dt}, \quad (5)$$

324 where subscripts i and c denote the ICB and CMB respectively. The power Q_s
 325 released by heat stored in the core in the core can then be written

$$Q_s = C_p \frac{T_i}{T_c} \frac{dT_c}{dt} \int \rho T_a dV. \quad (6)$$

326 The rate of growth of the inner core is give by

$$\frac{dr_i}{dt} = \frac{1}{(dT_m/dP)_{r=r_i} - (\partial T_a/\partial P)_{r=r_i}} \frac{1}{\rho(r_i)g(r_i)} \frac{T_i}{T_c} \frac{dT_c}{dt}, \quad (7)$$

327 (Gubbins et al., 2003), which together with the latent heat coefficient L defines the
 328 total heat released by latent heat at the ICB:

$$Q_L = 4\pi r_i^2 \rho(r_i) L \frac{dr_i}{dt}. \quad (8)$$

329 Using mass balance, the rate of change of light element fraction in the core is also

330 related to the ICB growth rate by

$$\frac{Dw_i^l}{Dt} = \frac{4\pi r_i^2 \rho(r_i)}{M_{oc}} (w_i^l - w_i^s) \frac{dr_i}{dt}, \quad (9)$$

331 (Gubbins et al., 2004), where M_{oc} is the mass of the outer core and the superscripts
 332 l and s here define quantities in the liquid and solid cores respectively. The gravita-
 333 tional energy release due to light elements mixing the core is

$$Q_g = \int \rho \psi \alpha_i^c \frac{Dw_i^l}{Dt} dV \quad (10)$$

334 (Gubbins et al., 2004), where ψ is the gravitational potential.

335 Together with the power Q_p produced by precipitation (defined precisely below),
 336 Q_s , Q_L and Q_g are the dominant terms in the core energy balance. It is therefore
 337 appropriate to write the total core energy balance as

$$Q^c = Q_s + Q_L + Q_g + Q_p = A \frac{dT_c}{dt} \quad (11)$$

338 (Gubbins et al., 2004; Nimmo, 2015b), where A represents integrals over core proper-
 339 ties that can be calculated from Table 2. Equation (11) is the basis of the core-mantle
 340 interaction model developed by Greenwood et al. (2021) that is used frequently be-
 341 low.

342 *2.3. Core thermal conductivity*

343 A detailed comparison of different methodologies for determining k is both be-
 344 yond the scope of this article and the expertise of the authors and so we refer the
 345 reader to Williams (2018), Zhang et al. (2020) and Pourovskii et al. (2020) for recent
 346 discussions. We consider experimental studies comprising direct determinations of k

347 in hcp iron (Konôpková et al., 2016) and solid Fe-Si alloys (Hsieh et al., 2020) and
 348 inferences of k based on measured electrical conductivity σ of hcp iron (Ohta et al.,
 349 2016; Xu et al., 2018; Zhang et al., 2020) and hcp Fe-Si alloys (Inoue et al., 2020)
 350 using the Wiedemann-Franz Law

$$k = LT\sigma, \quad (12)$$

351 where L is the Lorenz number. Equation (12) assumes that free electrons are pre-
 352 dominantly scattered elastically by phonons; in the case of perfect scattering L takes
 353 the Sommerfeld value of $L = L_0 = 2.44 \times 10^{-8} \text{ W } \Omega \text{ K}^{-2}$ (e.g. Secco, 2017). Recent
 354 computational studies also include inferences of k from the Wiedemann-Franz law
 355 (Xu et al., 2018) as well as direct determinations of k in liquid iron (Pozzo et al.,
 356 2012; de Koker et al., 2012; Pozzo and Alfè, 2016) and iron alloys (Pozzo et al., 2013;
 357 de Koker et al., 2012).

358 Figure 1 shows k values obtained directly (top) and inferred from the Wiedemann-
 359 Franz law (bottom) at the $P - T$ conditions reported in the above studies, i.e.
 360 without extrapolation to core conditions. Only selected high $P - T$ results are
 361 shown and so the $P - T$ trends obtained by individual studies are not represented.
 362 When comparing the various data, several factors need to be taken into account.
 363 Increases in k arise from increasing pressure and temperature. Decreasing k arises
 364 from the solid-liquid transition, presence of impurities, the effect of electron-electron
 365 scattering (for calculations), and a non-ideal value of L (for electrical conductivity
 366 measurements). We consider each of these factors in turn:

367 Pressure: Pozzo and Alfè (2016) provide the pressure-dependence of electrical
 368 conductivity of pure iron at 4350 K. Inoue et al. (2020) show P -dependence of a 4
 369 wt% Si alloy at 300 K and also at the similar temperatures of 1570 K and 1650 K.

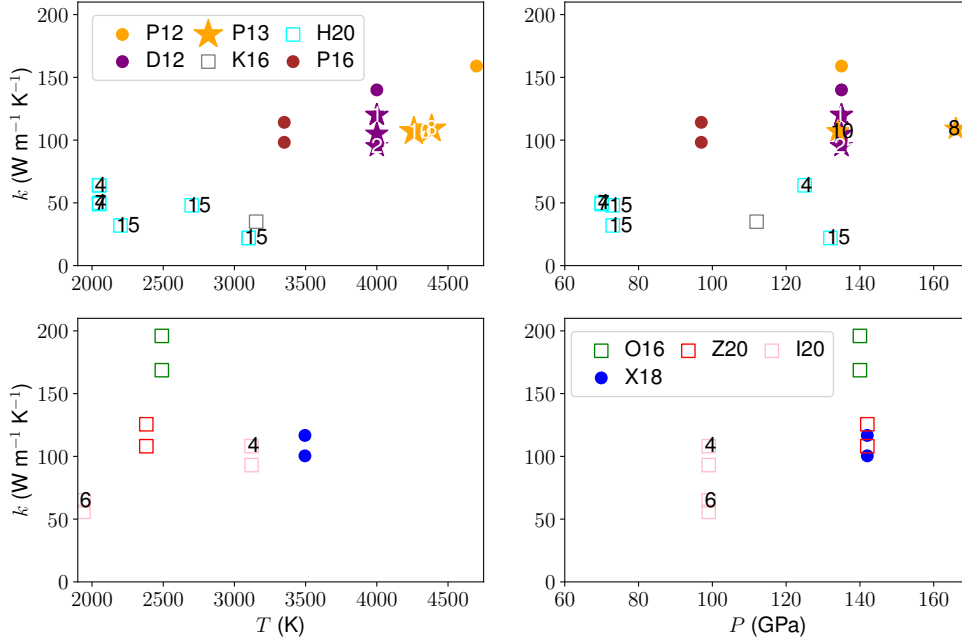


Figure 1: Summary of recent studies of core thermal conductivity k . The top row shows direct determinations of k while the bottom row shows inferences of k using electrical conductivity and the Wiedemann-Franz law. Left column shows the dependence on temperature T at the pressure P shown in the right column. Colours distinguish studies: open/closed symbols denote the method employed (experiment, calculation); shape denotes the material (square=solid, circle=liquid), stars distinguish alloys with the Si molar concentration denoted as a number inside the symbol. The considered studies are: P12 (Pozzo et al., 2012); D12 (de Koker et al., 2012); P13 (Pozzo et al., 2013); K16 (Konôpková et al., 2016); O16 (Ohta et al., 2016); P16 (Pozzo and Alfè, 2016); X18 (Xu et al., 2018); Z20 (Zhang et al., 2020); I20 (Inoue et al., 2020); H20 (Hsieh et al., 2020).

370 Converting to k values using equation (12) with $L = L_0$ yields mean dk/dP values of
371 $0.4 \text{ W m}^{-1} \text{ K}^{-1} \text{ GPa}^{-1}$ for Pozzo and Alfè (2016) and $0.13 \text{ W m}^{-1} \text{ K}^{-1} \text{ GPa}^{-1}$ and
372 $0.5 \text{ W m}^{-1} \text{ K}^{-1} \text{ GPa}^{-1}$ for Inoue et al. (2020) corresponding to an increase in k of
373 $15\text{--}20 \text{ W m}^{-1} \text{ K}^{-1}$ from 95 GPa to 135 GPa. We use $dk/dP = 0.4 \text{ W m}^{-1} \text{ K}^{-1} \text{ GPa}^{-1}$
374 below.

375 Temperature: The expected T behaviour depends critically on the validity of
376 equation (12) and the role of saturation effects (Konôpková et al., 2016; Pozzo and
377 Alfè, 2016). In the absence of saturation, the Bloch-Grüneisen formula predicts that
378 the electrical conductivity due to electron-phonon scattering varies as T^{-1} at high T ,
379 and hence $k = L \sim \text{constant}$ according to equation (12). Saturation can arise at high
380 T when the electron mean free path becomes comparable to the inter-atomic distance,
381 at which point σ stops decreasing with temperature and equation (12) predicts that
382 k increases with T . The relevance of saturation to Earth’s core properties was first
383 recognised by Gomi et al. (2013) and has been observed by Pozzo and Alfè (2016)
384 and Inoue et al. (2020), though not by Zhang et al. (2020). As a simple estimate
385 of dk/dT we use the results from de Koker et al. (2012), who found $dk/dT \approx$
386 $0.01 \text{ W m}^{-1} \text{ K}^{-1} \text{ K}^{-1}$ for FeO_3 at 135 GPa and $dk/dT \approx 0.02 \text{ W m}^{-1} \text{ K}^{-1} \text{ K}^{-1}$
387 for FeO_7 in the pressure range 130 – 160 GPa. In order to produce a conservative
388 increase in k we adopt $dk/dT = 0.01 \text{ W m}^{-1} \text{ K}^{-1} \text{ K}^{-1}$ below.

389 Phase transition: Zhang et al. (2020) discuss recent literature and invoke a 10%
390 decrease in σ on melting. Pozzo et al. (2013) find a change in σ of 18 – 25%, which is
391 mainly due to the solid structure, but also contains a contribution from the uneven
392 partitioning of elements at the ICB. We take the value of 18% below since this is
393 roughly halfway between the two extremes.

394 Impurities: Few studies have systematically compared the effect of different ele-
395 ments on k , but those that have find that the identity of the impurity is of secondary

396 importance compared to their abundance as should be expected from relatively in-
 397 sulating impurities acting as disruptions to metallic structure. Inoue et al. (2020)
 398 found that up to 6.5 wt% Si could reduce k by 10 – 20% while de Koker et al. (2012),
 399 Pozzo et al. (2013) and Zhang et al. (2020) found that various combinations of Si
 400 and O could reduce k by up to 30%. The recent work by Hsieh et al. (2020) suggests
 401 that the effect could be much more severe if there is a high Si concentration in the
 402 core. Here we assume a 20% reduction.

403 Electron-electron scattering (EES) and non-ideal L : EES can reduce both the
 404 k calculated from classical density functional theory (Pozzo et al., 2013; de Koker
 405 et al., 2012) and the L in equation (12) below the ideal value L_0 . At high $P - T$ for
 406 hcp iron Zhang et al. (2020) find a 20% decrease in σ due to EES and estimate $L \approx$
 407 $2.0 - 2.1 \times 10^{-8} \text{ W } \Omega \text{ K}^{-2}$, while Pourovskii et al. (2020) obtain a 20% decrease in k for
 408 bcc and hcp iron and estimate $L = 2.28 \times 10^{-8} \text{ W } \Omega \text{ K}^{-2}$ at ICB conditions. de Koker
 409 et al. (2012) also obtain $L \approx 1.8 - 2.4 \times 10^{-8} \text{ W } \Omega \text{ K}^{-2}$ without EES, indicating
 410 non-negligible inelastic scattering effects. In view of the current uncertainty we use
 411 $L = L_0$ and $L = 2.1 \times 10^{-8} \text{ W } \Omega \text{ K}^{-2}$ and adopt a 20% drop in k due to EES.

412 Figure 2 shows the extrapolated values of k for the studies in Figure 2. The major-
 413 ity of values fit within the range $70 \leq k \leq 110 \text{ W m}^{-1} \text{ K}^{-1}$. Notable outliers are the
 414 extrapolations from direct conductivity measurements for the pure hcp (Konôpková
 415 et al., 2016) and Si-rich Fe-Si solid (Hsieh et al., 2020). Future work is needed to
 416 understand the reasons for this, and to better constrain the extrapolation, which is
 417 subject to significant uncertainties as discussed above. For the rest of this article we
 418 focus on two values of conductivity: $k = 70 \text{ W m}^{-1} \text{ K}^{-1}$ and $k = 100 \text{ W m}^{-1} \text{ K}^{-1}$ as
 419 suggested by Figure 2. As such we will henceforth focus on the “high conductivity”
 420 scenario in Table 1.

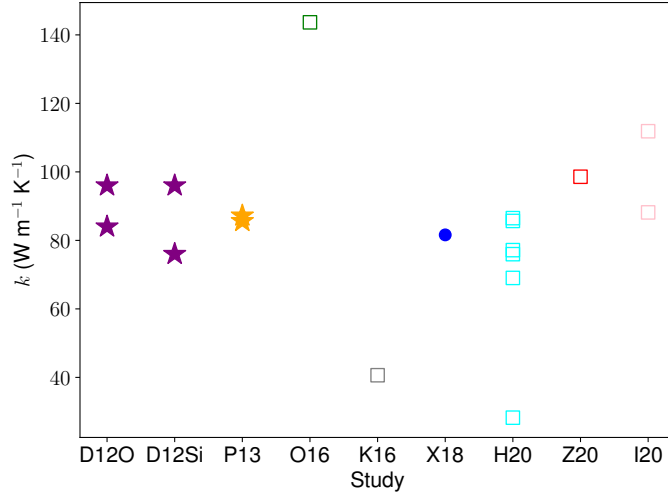


Figure 2: Extrapolation of k values in Figure 1 to CMB pressure of 135 GPa and temperature of 4000 K. The symbol styles are the same as in Figure 1.

421 3. Mass Transfer at the CMB

422 In general the chemical compositions of material in contact at the CMB will
 423 differ from the bulk compositions of the core and mantle, which gives rise to a
 424 chemical flux given by equation (3). The process of mass transfer at the CMB
 425 therefore depends on the chemical compositions of the core and mantle, both in the
 426 bulk and on either side of the CMB. Since we are primarily interested in the “high
 427 conductivity” scenario (see Table 1) we will focus on the interaction between the
 428 core and silicate melts in a basal magma ocean. This scenario is expected to yield
 429 greater chemical exchange than the interaction between the core and solid mantle
 430 because the significant increase in diffusion coefficient between solid mantle and BMO
 431 overwhelms any potential reduction in partition coefficient due to entropic effects in
 432 the melt (Pozzo et al., 2019).

433 Elements are usually assumed to be well-mixed by vigorous convection in the

434 proto-core (e.g. Rubie et al., 2015a), though it is possible that a stratified layer de-
435 veloped near the end of core formation (Landeau et al., 2016; Jacobson et al., 2017)
436 as discussed in Section 4.4. Self diffusion coefficients of O and Si in the liquid are
437 very small (see Pozzo et al., 2013, and Table 2) and so chemical diffusion in a primor-
438 dial stratified layer was probably too slow to produce significant time variations in
439 the bulk composition. An early BMO was also presumably well-mixed (Solomatov,
440 2015); however, its bulk composition could evolve over time. In the simple case of
441 fractional crystallisation the melt should become depleted in MgO and enriched in
442 FeO as the ocean shrinks (Labrosse et al., 2007; Caracas et al., 2019). However,
443 different scenarios for BMO evolution, such as compaction of an Fe-depleted mush
444 layer, could produce alternative compositional evolution. Therefore, the distinction
445 between precipitation and stratification scenarios depends primarily on the compo-
446 sitional evolution of a BMO and interactions at the CMB.

447 Chemical stratification of the upper core can arise when the equilibrium concen-
448 tration of an element i at the CMB exceeds its bulk concentration. The flux I_i is
449 negative and light element enters the core. Precipitation arises when the equilib-
450 rium concentration of i falls below the bulk concentration; I_i is positive and light
451 element leaves the liquid. In this case the lowest energy configuration (corresponding
452 to equality of the chemical potentials) is the co-existence of liquid with a solid phase,
453 usually assumed to be an oxide of the supersaturated element. If precipitation arises
454 at the CMB then the oxide, which is lighter than the bulk core liquid, will under-
455 plate onto the CMB, leaving behind a residual liquid at the top of the core that is
456 depleted in light element and hence denser than the core fluid below. Owing to the
457 low viscosity of the core, the dense residual liquid will rapidly sink via a Rayleigh-
458 Taylor instability, presumably mixing throughout the core. The gravitational energy

459 released by precipitation of element i is

$$Q_p = \int \rho \psi \alpha_i^c \frac{dw_i^c}{dt} dV \approx \int \rho \psi \alpha_i^c \frac{dw_i^c}{dT} \frac{dT}{dt} dV, \quad (13)$$

460 where V is the liquid core volume. The primary quantities of interest are therefore w_i^c ,
 461 which is critical for determining the onset and evolution of stratification/precipitation,
 462 and dw_i^c/dT , which determines the power released by precipitation. w_i^c and dw_i^c/dT
 463 are obtained from the equilibrium conditions at the CMB.

464 In this section we first present the calculation of equilibrium conditions at the
 465 CMB. The results will show that the fluxes I_i vary between elements i and also
 466 vary over time for a given element. Moreover, the flux of a given element depends
 467 not only on pressure P and temperature T but also on the abundance of other
 468 elements. We demonstrate the case of precipitation ($I_i > 0$) for MgO partitioning
 469 and stratification ($I_i < 0$) for FeO partitioning in isolation. Finally, we consider the
 470 coupled equilibrium conditions for MgO, FeO and SiO₂.

471 3.1. Chemical Equilibrium at the CMB

Departures from chemical equilibrium for materials in contact at the CMB should be very small since the timescale for diffusion is very short over such small length-scales. Chemical equilibrium at the CMB requires equality of chemical potentials μ_i for each species i , while mass conservation (ignoring thermal contraction of the core) implies that the total flux of mass from the mantle I_i equals the mass added to the core (Braginsky and Roberts, 1995; Davies et al., 2020). These conditions can be

written

$$\begin{aligned}
\mu_1^m(P, T, c_1^m, \dots, c_{N^m}^m) &= \mu_2^c(P, T, c_1^c, \dots, c_{N^c}^c), \\
\mu_2^m(P, T, c_1^m, \dots, c_{N^m}^m) &= \mu_2^c(P, T, c_1^c, \dots, c_{N^c}^c), \\
&\dots \\
\mu_{N^m}^m(P, T, c_1^m, \dots, c_{N^m}^m) &= \mu_{N^c}^c(P, T, c_1^c, \dots, c_{N^c}^c); \tag{14} \\
I_1^m(P, T, c_1^m, \dots, c_{N^m}^m) &= I_2^c(P, T, c_1^c, \dots, c_{N^c}^c), \\
I_2^m(P, T, c_1^m, \dots, c_{N^m}^m) &= I_2^c(P, T, c_1^c, \dots, c_{N^c}^c), \\
&\dots
\end{aligned}$$

$$I_{N^m}^m(P, T, c_1^m, \dots, c_{N^m}^m) = I_{N^c}^c(P, T, c_1^c, \dots, c_{N^c}^c). \tag{15}$$

472 where superscripts m and c denote the mantle and core respectively, $i, = 1, \dots, N^m$
473 and $j = 1, \dots, N^c$ represent the number of chemical species in the mantle and core
474 respectively and c_i denotes the mole fraction of species i . Here the pressure and
475 temperature correspond to conditions at the CMB. Note that equation (15) does not
476 imply equality of the chemical compositions.

477 The key quantity for determining equilibrium conditions at the CMB is the equi-
478 librium constant K , which is defined as

$$K = \frac{\prod_i a_i}{\prod_j a_j} = \frac{\prod_i c_i}{\prod_j c_j} \cdot \frac{\prod_i \gamma_i}{\prod_j \gamma_j} = K_d \cdot \frac{\prod_i \gamma_i}{\prod_j \gamma_j}, \tag{16}$$

479 where K_d is the distribution coefficient, $a_i = c_i \gamma_i$ are the activities and γ_i are the
480 activity coefficients. Here the i denotes the products that appear on the right side of
481 the reaction and j denotes the reactants. At equilibrium K is related to the Gibbs

482 free energy change across the reaction ΔG_r by

$$K = \exp\left(-\frac{\Delta G_r}{k_B T}\right) = \exp\left(-\frac{\Delta H_r - T\Delta S_r + P\Delta V_r}{k_B T}\right), \quad (17)$$

483 where k_B is the Boltzmann constant and ΔH_r , ΔS_r and ΔV_r , are respectively the
 484 standard state change in enthalpy, entropy and volume across the reaction. Equa-
 485 tion (17) is usually written as

$$\log K_d = a + \frac{b}{T} + c\frac{P}{T} - \sum_i (\log \gamma_i) + \sum_j (\log \gamma_j), \quad (18)$$

486 where the coefficients a , b , c and γ_i are to be determined from recovered phases that
 487 are analysed at known $P - T$ -composition conditions. Note for consistency with
 488 previous work we have retained the notation for the coefficient c , which should not
 489 be confused with mole fraction.

490 Computer simulations can be used to calculate chemical potentials for each species
 491 (e.g. Alfè et al., 2002b; Pozzo et al., 2019) and hence the equilibrium concentrations
 492 can be obtained directly from equations (14). Separating out the configurational
 493 part of the chemical potential, i.e. $\mu_i = k_B T \ln c_i + \tilde{\mu}_i$, the equilibrium becomes

$$\sum_i [k_B T \ln c_i^m + \tilde{\mu}_i^m] = \sum_j [k_B T \ln c_j^c + \tilde{\mu}_j^c], \quad (19)$$

494 OR

$$k_B T \ln \left[\frac{\prod_j c_j^c}{\prod_i c_i^m} \right] = k_B T \ln K_d = \sum_i \tilde{\mu}_i^m - \sum_j \tilde{\mu}_j^c, \quad (20)$$

495 (Davies et al., 2018; Pozzo et al., 2019). Since the chemical potentials are completely
 496 determined, this formulation can be shown to be equivalent to equation (17) by
 497 separating the chemical potentials as $\mu_i = \mu_i^0 + k_B T \ln Y_i$, where μ_i^0 is the value of μ_i

498 in standard state.

499 The form of K (and K_d) is determined by the nature of the chemical reaction.
500 The reactions that have generally been considered in the literature are dissolution,
501 dissociation and exchange (e.g. Badro et al., 2018). These are summarised in Table 3.
502 In principle numerical simulations could be used to distinguish between the different
503 possibilities, however the simulation sizes required to obtain meaningful concentra-
504 tions have traditionally been prohibitively costly in *ab initio* calculations. Another
505 approach is to compare large datasets against the predictions from equation (18),
506 which has been done recently for MgO by Badro et al. (2018). We reproduce the
507 workflow of Badro et al. (2018) below to demonstrate the steps involved in obtain-
508 ing equilibrium concentrations and precipitation rates and to provide a consistent
509 framework with which to compare recent studies. Compositional variations in sili-
510 cate activity coefficients are neglected and hence the γ_j^m can be absorbed into the
511 parameters a and b ; the γ_i below therefore refer to the metal. Silicate activities can
512 be included in the modelling (Frost et al., 2010; Helffrich et al., 2020), but at the
513 expense of introducing more fitting parameters.

514 3.2. Partitioning of MgO at the CMB

The equations determining $\log K_d$ for MgO dissolution, dissociation and exchange are respectively

$$\log \frac{c_{MgO}^c}{c_{MgO}^m} = \log K_{dl}^{MgO} = a + \frac{b}{T} + c \frac{P}{T} - \log \gamma_{Mg}^c - \log \gamma_O^c, \quad (21)$$

$$\log \frac{c_{Mg}^c c_O^c}{c_{MgO}^m} = \log K_{dc}^{MgO} = a + \frac{b}{T} + c \frac{P}{T} - \log \gamma_{Mg}^c - \log \gamma_O^c, \quad (22)$$

$$\log \frac{c_{Mg}^c c_{FeO}^m}{c_{Fe}^c c_{MgO}^m} = \log K_e^{MgO} = a + \frac{b}{T} + c \frac{P}{T} - \log \gamma_{Mg}^c + \log \gamma_{Fe}^c. \quad (23)$$

Reaction	K_d	Ref
$\text{MgO}^m \rightleftharpoons \text{Mg}^c + \text{O}^c$	$\frac{c_{\text{Mg}}^c c_{\text{O}}^c}{c_{\text{MgO}}^m}$	B16 B18 M20 H20
$\text{MgO}^m \rightleftharpoons \text{MgO}^c$	$\frac{c_{\text{MgO}}^c}{c_{\text{MgO}}^m}$	B18
$\text{MgO}^m + \text{Fe}^c \rightleftharpoons \text{FeO}^m + \text{Mg}^c$	$\frac{c_{\text{FeO}}^m c_{\text{Mg}}^c}{c_{\text{Fe}}^c c_{\text{MgO}}^m}$	OS16, D17, D19
$2\text{MgO}^m + \text{Si}^c \rightleftharpoons \text{SiO}_2^m + 2\text{Mg}^c$	$\frac{c_{\text{SiO}_2}^m (c_{\text{Mg}}^c)^2}{c_{\text{Si}}^c (c_{\text{MgO}}^m)^2}$	H20
$\text{FeO}^m \rightleftharpoons \text{Fe}^c + \text{O}^c$	$\frac{c_{\text{Fe}}^c c_{\text{O}}^c}{c_{\text{FeO}}^m}$	F10 OS16 D18 M20 F15
$\text{SiO}_2^m \rightleftharpoons \text{Si}^c + 2\text{O}^c$	$\frac{c_{\text{Si}}^c (c_{\text{O}}^c)^2}{c_{\text{SiO}_2}^m}$	H17 M20 H20
$\text{SiO}_2^m \rightleftharpoons \text{SiO}_2^c$	$\frac{c_{\text{SiO}_2}^c}{c_{\text{SiO}_2}^m}$	
$\text{SiO}_2^m + 2\text{Fe}^c \rightleftharpoons 2\text{FeO}^m + \text{Si}^c$	$\frac{(c_{\text{FeO}}^m)^2 c_{\text{Si}}^c}{(c_{\text{Fe}}^c)^2 c_{\text{SiO}_2}^m}$	OS16, F15

Table 3: Summary of chemical reactions between MgO, SiO₂, FeO and metallic alloys considered in recent literature. The cited studies are Badro et al. (2016, B16), Badro et al. (2018, B18), Du et al. (2017, D17), Du et al. (2019, D19), Fischer et al. (2015, F15), Frost et al. (2010, F10), Helffrich et al. (2020, H20), Hirose et al. (2017, H17), Mittal et al. (2020, M20), and O’Rourke and Stevenson (2016, O16).

515 Equations (21)–(23) are evaluated using the values of a , b and c reported in several
516 previous studies and reproduced in Table 4. When accounting for compositional
517 effects O’Rourke and Stevenson (2016) set all activity coefficients to 1, Du et al.
518 (2019) model the effect of O and Si, while Badro et al. (2018) consider interactions
519 between O, Si, Mg, C, and S. Figure 3 shows K_{dl}^{MgO} and K_e^{MgO} calculated for MgO
520 dissociation and exchange reactions using the Badro et al. (2018) dataset. It is
521 clear that accounting for the composition-dependence of partitioning via the activity
522 coefficients, specifically oxygen and magnesium content of the metal, produces a
523 significant reduction in data scatter. The importance of oxygen content was noted
524 by Du et al. (2017), while the composition-dependence on joint solubility of Si, Mg
525 and O is clearly demonstrated in Helffrich et al. (2020).

526 The γ_i^c are quite sensitive to the values of the parameters ϵ_i^j , which describe the
527 interaction between elements i and j in the liquid (e.g. Badro et al., 2018). For ease

Study	Reaction	a_{Mg}	b_{Mg}	c_{Mg}
O16	e	0.1	-10851	0
B16	dl	1.23	-18816	0
B18	ds	0.1	-14054	0
B18	e	1.06	-12842	0
D19	e	-3.0	-2314	26
		a_O	b_O	c_O
O16	e	0.6	-3800	22
M20	ds	-0.3	0.0	-36.8
		a_{Si}	b_{Si}	c_{Si}
O16	e	1.3	-13500	0
M20	See text			

Table 4: Values of the constant parameters used in this study to fit empirically determined distribution coefficients. The sections show from top to bottom Mg, O and Si. For O and Si the values denoted by O16 (O’Rourke and Stevenson, 2016) were obtained from Fischer et al. (2015), while the values for Mg were estimated from experiments in Takafuji et al. (2005). For Mittal et al. (2020, M20) the values for O come from Hirose et al. (2017). Abbreviations ‘e’, ‘ds’ and ‘dl’ denote exchange, dissociation and dissolution reactions and are used as superscripts in the text.

528 of comparison these parameters are listed in Table 5 from the studies of Badro et al.
529 (2018), Fischer et al. (2015) and Liu et al. (2020). Overall there is general consistency
530 between the three studies, though with some notable exceptions such as ϵ_{Si}^{Si} and ϵ_O^C .
531 We test the effect by conducting two calculations that use the same parameters as
532 in Figure 3 and differ only by using the ϵ_i^j values of Liu et al. (2020) in place of
533 the respective values from Badro et al. (2018). At 6000 K we obtain $\gamma_O^c = 4.125$,
534 $\gamma_{Mg}^c = 0.74$ and $w_{Mg}^c = 1.1$ for Badro et al. (2018) and $\gamma_O^c = 3.40$, $\gamma_{Mg}^c = 0.61$ and
535 $w_{Mg}^c = 1.78$ for Liu et al. (2020); at 4200 K we obtain $\gamma_O^c = 1.20$, $\gamma_{Mg}^c = 0.65$ and
536 $w_{Mg}^c = 0.52$ for Badro et al. (2018) and $\gamma_O^c = 0.91$, $\gamma_{Mg}^c = 0.50$ and $w_{Mg}^c = 0.96$ for
537 Liu et al. (2020). This calculation is not entirely self-consistent because the γ_i^c are
538 fit to the data alongside the values of a , b and c and are therefore not independent;
539 nevertheless, it does show the that uncertainties in the γ_i^c could propagate into a
540 $\sim 30 - 40\%$ change in the predicted equilibrium concentration.

ϵ_i^j	B18	F15	L20
$\epsilon_{\text{O}}^{\text{O}}$	-1.0	-7.0	-5.8
$\epsilon_{\text{Si}}^{\text{Si}}$	12.4	0.0	0.0
$\epsilon_{\text{Mg}}^{\text{Mg}}$	0.0	–	0.0
$\epsilon_{\text{C}}^{\text{C}}$	12.8	–	–
$\epsilon_{\text{S}}^{\text{S}}$	-5.7	–	–
$\epsilon_{\text{O}}^{\text{Si}}$	-5.0	-7.0	-8.3
$\epsilon_{\text{O}}^{\text{C}}$	-20.0	8.0	–
$\epsilon_{\text{O}}^{\text{S}}$	-17.1	–	–
$\epsilon_{\text{O}}^{\text{Mg}}$	-12.2	–	-16.4
$\epsilon_{\text{S}}^{\text{Si}}$	9.0	–	–
$\epsilon_{\text{S}}^{\text{C}}$	4.9	–	–
$\epsilon_{\text{Mg}}^{\text{Mg}}$	4.4	–	0.0
$\epsilon_{\text{S}}^{\text{Mg}}$	13.8	–	–
$\epsilon_{\text{C}}^{\text{Mg}}$	24.3	–	–
$\epsilon_{\text{C}}^{\text{Si}}$	3.6	–	–

Table 5: Comparison of values for the interaction parameters ϵ_i^j between element i and j in liquid iron used in the studies of Badro et al. (2018, B18), Fischer et al. (2015, F15) and Liu et al. (2020, L20). The B18 values correspond to the dissolution reaction.

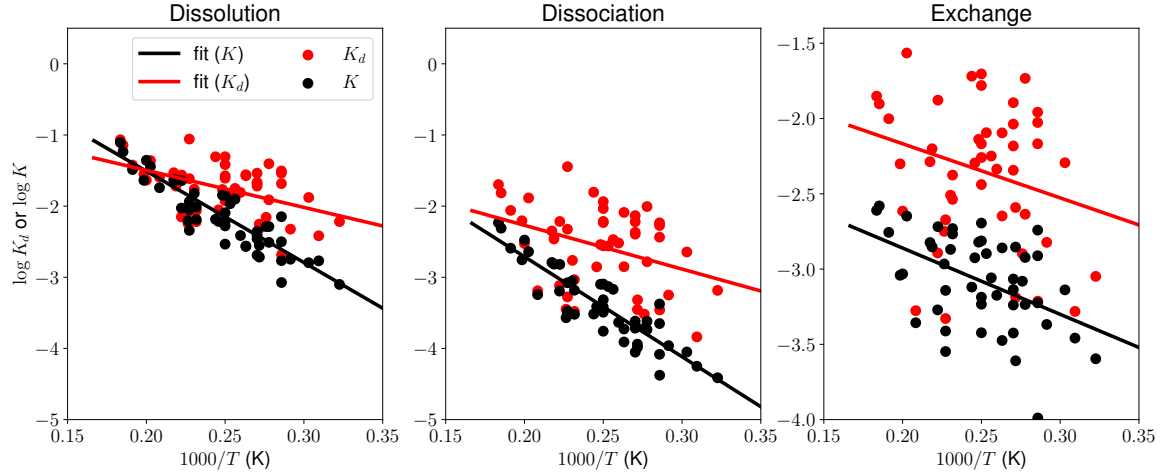


Figure 3: Calculated equilibrium constants for MgO dissolution (left), dissociation (centre) and exchange (right) reactions using the dataset in Badro et al. (2018, Table S1). Red points show $K = K_d$, i.e. with all activity coefficients set to one, while black points show K values calculated using the methodology of Badro et al. (2018) and data in their Table S2. Black and red lines are fits to the respectively datasets using Equations (21)–(23).

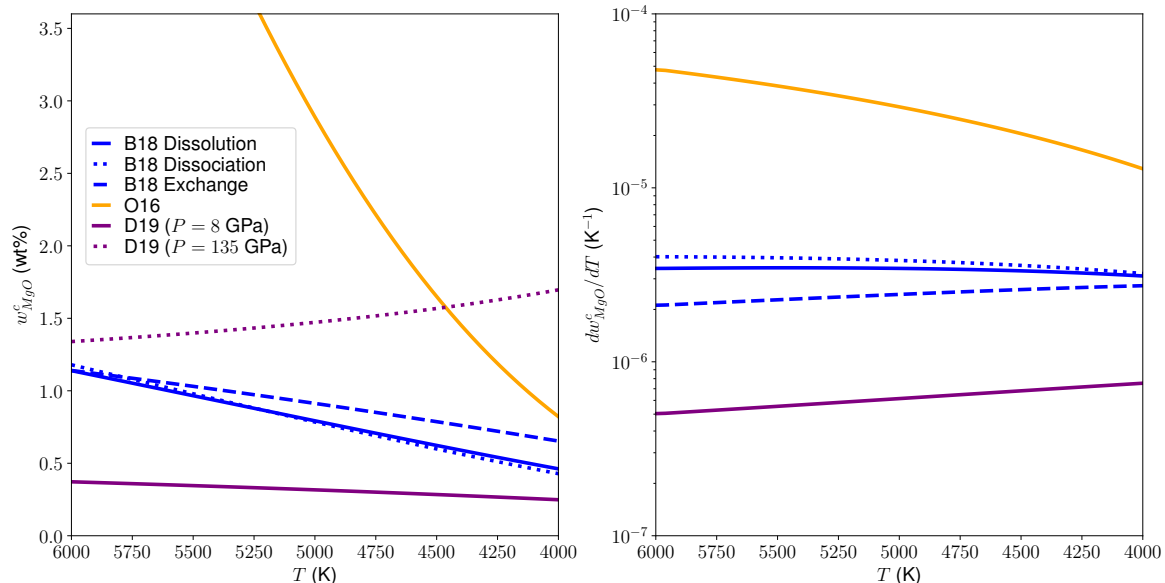


Figure 4: Equilibrium mass fraction of MgO (left) and precipitation rate dw_{MgO}^c/dT for a constant core composition of 3 wt% O and 3 wt% Si and a constant BMO composition of 50 mol% MgO and 10 mol% FeO. Considered studies are O’Rourke and Stevenson (2016, O16), Badro et al. (2018, B18) and Du et al. (2019, D19).

541 In order to compare results from different assumed reactions and modelling strate-
542 gies Figure 4 shows the core weight fraction of MgO, w_{MgO}^c , vs temperature. We
543 consider the same compositions as Badro et al. (2018): a constant 3 wt% O and 3
544 wt% Si in the core and 50 mol% MgO in the mantle. Using the Badro et al. (2018)
545 method and dataset the dissociation and dissolution reactions produce almost iden-
546 tical results while all three reactions yield similar dw_{MgO}^c/dT as found by Du et al.
547 (2019), though the exchange reaction yields a worse fit to their data (see Badro
548 et al., 2018, and Figure 3). O’Rourke and Stevenson (2016) obtain a much larger
549 equilibrium concentration and dw_{MgO}^c/dT than the more recent studies that include
550 composition-dependence on the equilibrium conditions. This result underscores the
551 importance of accounting for the light element content of the core when modelling
552 precipitation rates.

553 The pressure-dependence of equilibrium is a critical issue because this governs
554 the depth in the core at which precipitation will commence. Badro et al. (2016),
555 Badro et al. (2018) and Du et al. (2017) find that the K^{MgO} are independent of
556 P and hence precipitation must begin at the CMB. Du et al. (2019) obtained a
557 statistically significant pressure variation for K_e^{MgO} , which has a significant impact
558 on the equilibrium behaviour obtained from their model. Figure 4 shows that at
559 8 GPa and 10 mol% FeO the equilibrium composition from Du et al. (2019) is almost
560 independent of temperature as advocated in their earlier study (Du et al., 2017).
561 However, when evaluated at CMB pressure this model predicts that precipitation
562 would begin at the lowest temperature, i.e. the present day, and would therefore
563 have been unavailable to provide power to the dynamo in the past.

564 The equilibrium concentrations in Figure 4 should be compared to the initial Mg
565 content of the core, estimated to lie in the range 0.3 – 3.6 wt% (Section 2). Tak-
566 ing the higher end of these estimates, all studies in Figure 4 except O’Rourke and
567 Stevenson (2016) predict that the core was over-saturated in Mg for all tempera-
568 tures below 6000 K; the bulk core Mg content was then higher than the CMB value
569 corresponding to a positive (outward) flux I_{Mg} and the precipitation of MgO from
570 the core. Conversely, using the lowest value, 0.3 wt% Mg, all studies predict that
571 the core was under-saturated in Mg for all temperatures above 4000 K; the bulk
572 core Mg content has then always been lower than the CMB value corresponding to a
573 negative (inward) I_{Mg} and stratification of the uppermost core due to enrichment in
574 Mg. Therefore, for fixed core and mantle compositions, Mg could either dissolve or
575 precipitate at the top of the core within the uncertainties in partitioning behaviour
576 and initial core composition.

577 Focusing on the precipitation case, Figure 4 shows that the individual modelling
578 approaches and datasets used by different groups result in a spread of MgO precipi-

579 tation rates dw_{MgO}^c/dT that span almost two orders of magnitude. The high values
 580 from O'Rourke and Stevenson (2016) are likely due to their assumption that O and
 581 Mg activity coefficients could be set to zero, which was reasonable at the time when
 582 few experimental data were available. More recent work suggests lower precipitation
 583 rates, which correspondingly reduces the efficiency of precipitation as a mechanism
 584 for sustaining the ancient geomagnetic field. However, as shown in Section 3.4 below,
 585 higher dw_{MgO}^c/dT can be obtained when the coupled reaction between MgO, SiO₂
 586 and FeO are considered.

587 Figure 5 shows MgO precipitation rate as a function of temperature for the dis-
 588 solution reaction and different constant core and mantle compositions that span the
 589 ranges described in Section 2. It is clear that both the core O content and the mantle
 590 MgO composition significantly affect dw_{MgO}^c/dT , which should be taken in the con-
 591 text of the $\sim 40\%$ uncertainties on the calculated equilibrium concentration (Badro
 592 et al., 2018). In these calculations the amount of Si in the core has a relatively minor
 593 effect; however, this is not the case if an exchange reaction involving MgO and SiO₂
 594 governs the partitioning behaviour of Mg (Helffrich et al., 2020). Interestingly the
 595 precipitation rate is almost independent of T in all cases considered. However, this
 596 turns out not to be the case when the joint equilibrium of Mg, O and Si is considered
 597 in Section 3.4.

598 3.3. Partitioning of FeO at the CMB

599 Previous studies have generally modelled FeO transfer using a dissolution reaction
 600 with distribution coefficient $K_d^{FeO} = c_{Fe}^c c_O^c / c_{FeO}^m$. As with Mg, the most significant
 601 interaction parameters involve Si and O because of their expected high concentrations
 602 in the core. However, Fischer et al. (2015) found that their fitted ϵ_{Si}^O and ϵ_O^O values
 603 produced an unstable parameterisation in which partitioning of O into metal would

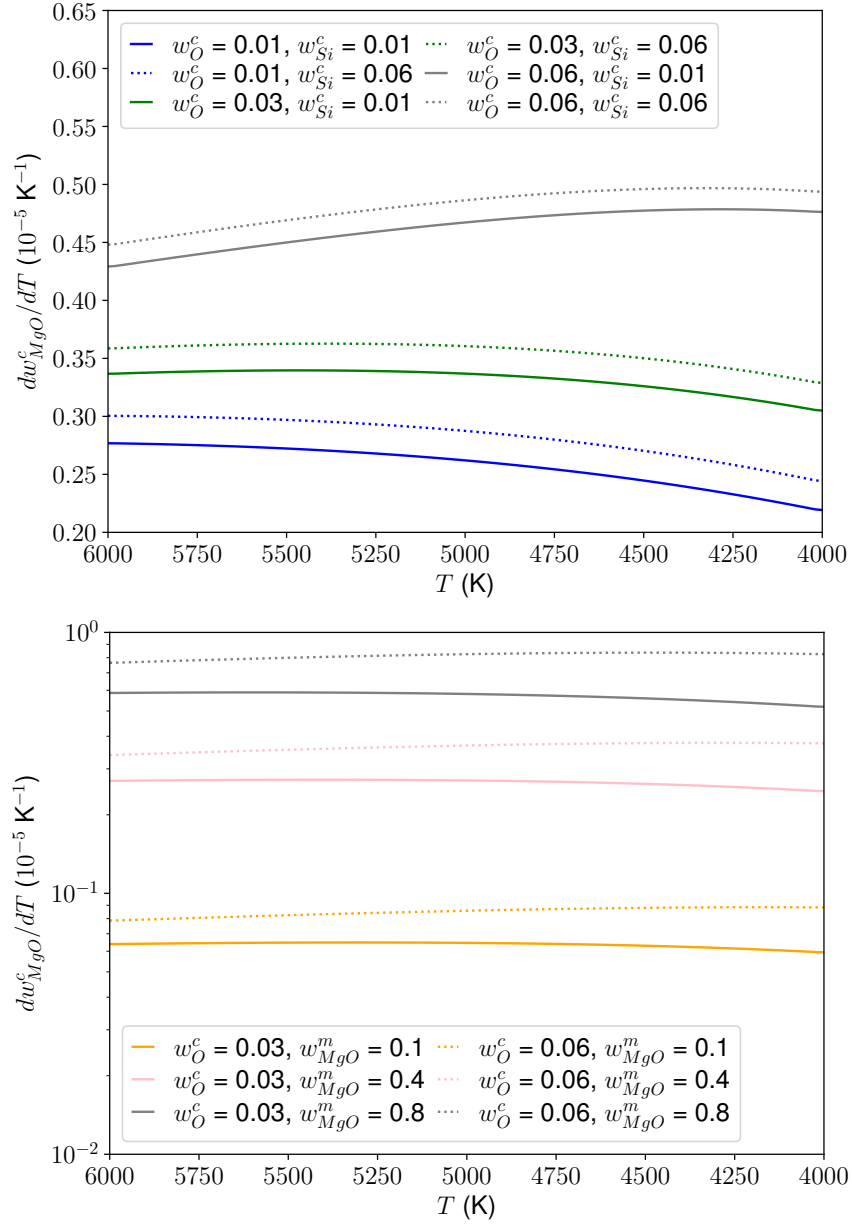


Figure 5: Precipitation rate dw_{MgO}^c/dT as a function of temperature T for various starting compositions in the core (top) and BMO (bottom).

604 cause ever more O and Si to enter the core. Considering the interaction between
 605 an Fe-O metal and ferropericlase, Davies et al. (2018) found that K_d^{FeO} is a weak
 606 function of oxygen concentration in the range $0 \leq c_{\text{O}}^c \leq 30$ mol%, while adding 7.6
 607 mol% Si to the metal produced a strong increase of K_d^{FeO} with c_{O}^c , consistent with
 608 the findings of Tsuno et al. (2013) and Fischer et al. (2015) for the case of silicate
 609 melts. Pozzo et al. (2019) performed first principles molecular dynamics calculations
 610 to determine K_d^{FeO} at CMB $P - T$ conditions for a silicate melt comprising 50 mol%
 611 SiO_2 , 44 mol% MgO , and 6 mol% FeO and a liquid metal comprising 95 mol% Fe and
 612 5 mol% O; however, they were not able to determine the composition-dependence of
 613 K_d^{FeO} owing to the large system sizes needed to robustly estimate free energy changes.
 614 Here we ignore the composition-dependence on FeO partitioning and focus on K_d^{FeO} ,
 615 noting that improved constraints by future studies will be very valuable.

616 Figure 6 shows the temperature and pressure dependence of K_d^{FeO} from a number
 617 of recent experimental and computational studies. Davies et al. (2018) have shown
 618 that simulations at 134 GPa and 3200 K agree well with experiments at the same
 619 conditions with a starting composition consisting of a powdered mixture of pure
 620 metal and $\text{Mg}_{81}\text{Fe}_{19}\text{O}$ (Ozawa et al., 2008). Therefore any discrepancy between the
 621 two types of study are likely due to differences in the starting compositions and
 622 uncertainties in determining exact $P - T$ conditions. These factors produce a scatter
 623 of 0.5 – 1 log units over much of the moderate T range and are consistent with the
 624 differences observed at high T . The results show that K_d^{FeO} increases with both P
 625 and T and that O tends to favour the metal as core conditions of $T > 4000$ K are
 626 approached.

627 Figure 7 shows the equilibrium concentration of O in the core for different core and
 628 BMO Fe concentrations spanning the ranges discussed in Section 2. Here K_d^{FeO} has
 629 been fit using the black line in Figure 6, which yields values on the lower end of the

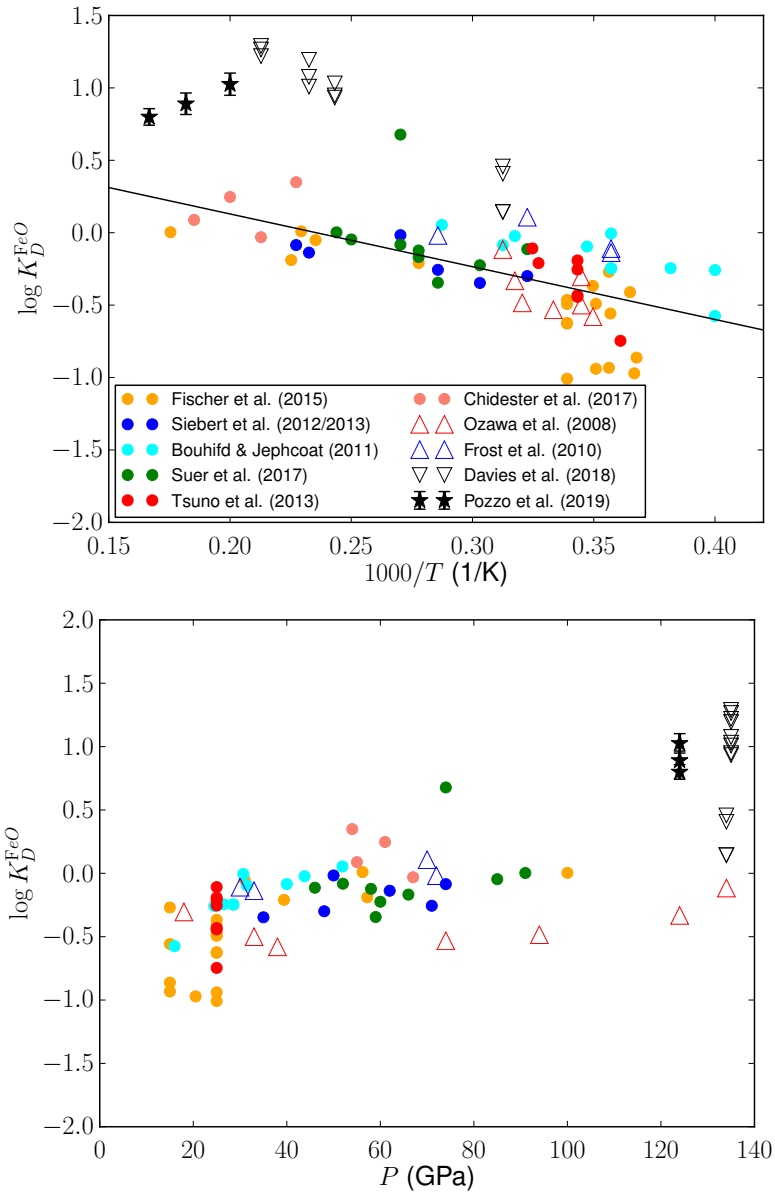


Figure 6: Comparison of published FeO distribution coefficients. Panels show values of the distribution coefficient K_D^{FeO} plotted against inverse temperature (top) and pressure (bottom) for solid-silicate-liquid-metal partitioning (open symbols) and silicate-melt-liquid-metal partitioning (closed symbols). The plotted studies are: Fischer et al. (2015), Siebert et al. (2012), Bouhifd and Jephcoat (2011), Suer et al. (2017), Tsuno et al. (2013), Chidester et al. (2017), Ozawa et al. (2008), Frost et al. (2010), Davies et al. (2018) and Pozzo et al. (2019). Figure adapted from Pozzo et al. (2019).

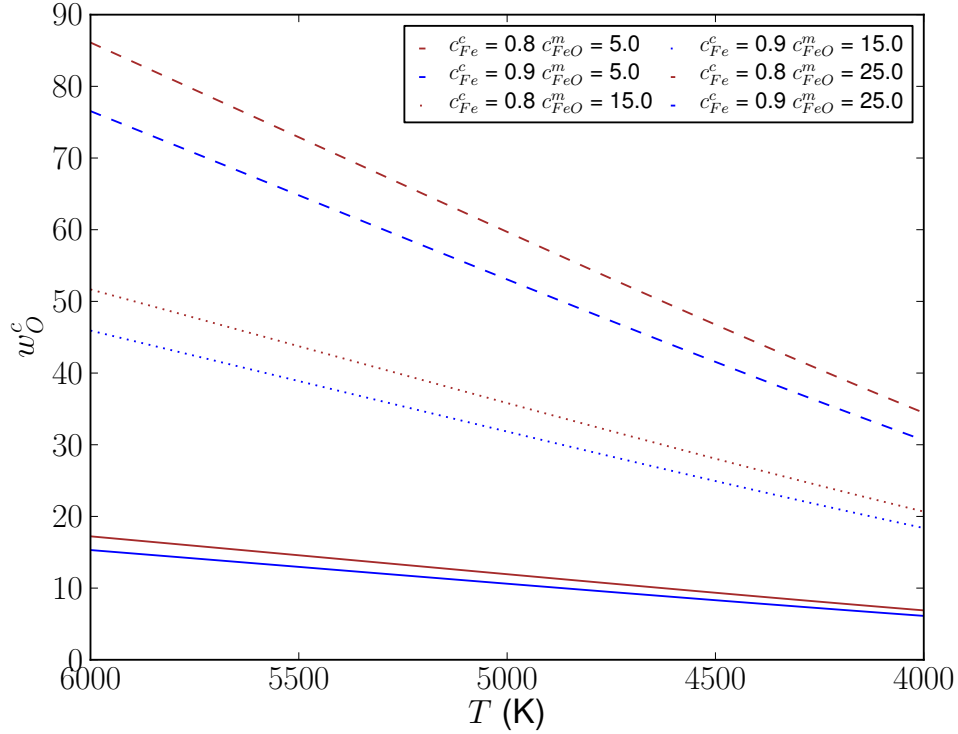


Figure 7: Equilibrium concentration of O in the core (wt %) as a function of temperature T for different concentrations of iron in the core, c_{Fe}^c , and FeO concentrations in the BMO, c_{FeO}^m .

630 range at high T ; higher K_d^{FeO} would therefore increase the equilibrium concentrations
 631 in Figure 7. The results clearly show that the equilibrium O concentration exceeds all
 632 estimates for the bulk core O concentration. Therefore, FeO is expected to partition
 633 strongly into liquid iron at high T , creating a stably stratified layer atop the core
 634 (Buffett and Seagle, 2010; Davies et al., 2018).

635 3.4. Partitioning of multiple species at the CMB

636 In general the CMB compositions of the four elements assumed to be in the core
 637 (Fe, Si, O, Mg) and the three oxides assumed to comprise the BMO (MgO, FeO, SiO₂)
 638 can vary over time. The seven equations required to solve the system are obtained
 639 from mass balance of the four elements and the equilibrium constants for the three

640 reactions (Rubie et al., 2011). These equations are nonlinear and hence both the
641 onset and rate of precipitation of a given chemical species will in general depend
642 sensitively on P , T , starting composition and the functional forms of the equilibrium
643 constants. In this section we will show how the onset and rate of precipitation depend
644 on these factors.

645 We calculate equilibrium concentrations following the method of Rubie et al.
646 (2011). The main limitation of this method is that it is not easily generalised to
647 include composition-dependence of the equilibrium constants. This is clearly an
648 important issue since we have shown above that the equilibrium concentration of
649 Mg is sensitive to the O and Mg concentration in the core. However, given the
650 complexity of multi-species partitioning and significant uncertainties on some of the
651 key parameters this is a necessary first step. It also simplifies the calculation of
652 precipitation rates, which are needed by core thermal history models. Rubie et al.
653 (2011) consider partitioning of Ni and assume a constant bulk Mg composition. Here
654 we transpose Ni and Mg in their equations (details are provided in Appendix 1). We
655 consider three different cases labelled according to whether the reaction governing
656 transfer of O, Si and Mg are respectively exchange (E) or dissociation (D):

1. DEE. This Case corresponds to that of Rubie et al. (2011), who model oxygen transfer as a dissociation reaction and Si and Ni (here Mg) transfer by exchange reactions. The distributions coefficients are:

$$\log \frac{c_{Fe}^c c_O^c}{c_{FeO}^m} = a_O^{ds} + \frac{b_O^{ds}}{T} + c_O^{ds} \frac{P}{T}, \quad (24)$$

$$\log \frac{(c_{FeO}^m)^2 c_{Si}^c}{(c_{Fe}^c)^2 c_{SiO2}^m} = a_{Si}^e + \frac{b_{Si}^e}{T} + c_{Si}^e \frac{P}{T}, \quad (25)$$

$$\log \frac{c_{FeO}^m c_{Mg}^c}{c_{Fe}^c c_{MgO}^m} = a_{Mg}^e + \frac{b_{Mg}^e}{T} + c_{Mg}^e \frac{P}{T}. \quad (26)$$

- 657 2. DED. This Case retains the same reactions for Si and O as in Case 1, but
658 employs a dissociation reaction for Mg as advocated by Badro et al. (2018) .
3. DDD. This Case employs dissociation reactions for all three species as done by
Mittal et al. (2020), with distribution coefficients given by

$$\log \frac{c_{Fe}^c c_O^c}{c_{FeO}^m} = a_O^{ds} + \frac{b_O^{ds}}{T} + c_O^{ds} \frac{P}{T}, \quad (27)$$

$$\log \frac{c_{Si}^c (c_O^c)^2}{c_{SiO_2}^m} = a_{Si}^{ds} + \frac{b_{Si}^{ds}}{T} + c_{Si}^{ds} \frac{P}{T}, \quad (28)$$

$$\log \frac{c_{Mg}^c c_O^c}{c_{MgO}^m} = a_{Mg}^{ds} + \frac{b_{Mg}^{ds}}{T} + c_{Mg}^{ds} \frac{P}{T}. \quad (29)$$

659 For Cases 2 and 3 the required modifications to the method of Rubie et al. (2011)
660 are explained in Appendix 1.

661 The dependence of $\log K_d$ on temperature used in this section is shown in Figure 8.
662 The a , b and c values are not the same as those in Table 4 because we ignore the
663 composition-dependence. We have therefore refit K_d^{MgO} using the Badro et al. (2018)
664 dataset as shown by the red lines in Figure 3, obtaining $a = -1.45$ and $b = -3596$ for
665 the exchange reaction and $a = -1.039$ and $b = -6151$ for the dissociation reaction.
666 We have also refit the a and b values from Du et al. (2019) based on a mean 15
667 mol% O in the core in order to account for the composition-dependence of their
668 parameterisation. For Fe we use the parameters from Fischer et al. (2015). For
669 reference, Figure 8 also shows K_d^{FeO} from Hirose et al. (2017); however, we were
670 unable to obtain solutions to the mass balance equations with this parameterisation.
671 For Si we use the exchange reaction parameterisation from Fischer et al. (2015) and
672 the dissociation parameterisation of Mittal et al. (2020), who refit the partitioning
673 data of Hirose et al. (2017).

674 Figure 9 shows two calculations using the initial compositions of Badro et al.

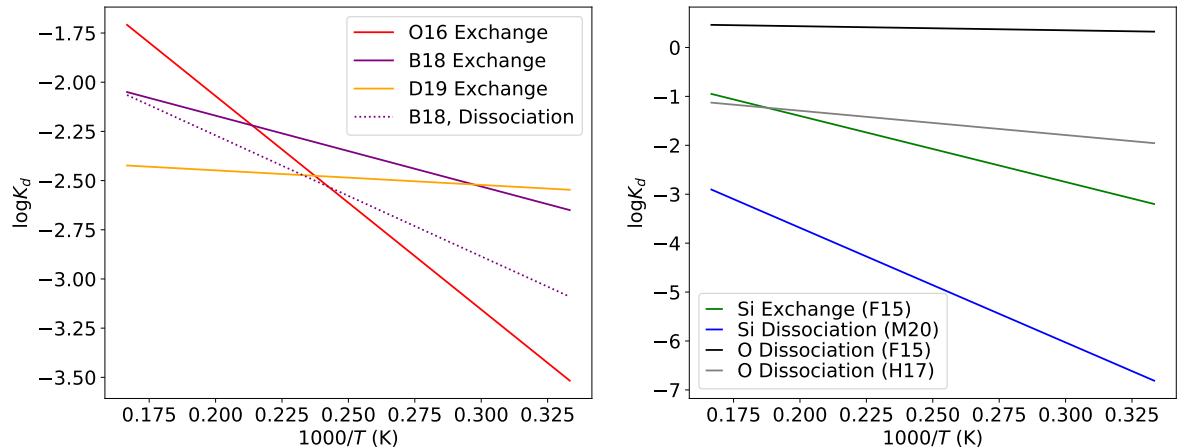


Figure 8: Distribution coefficients for Mg (left) and Si/O (right) used in comparison of multi-species precipitation.

675 (2018) for the DED and DEE cases respectively. The general behaviour in both cases
 676 is very similar to that described in O'Rourke and Stevenson (2016) and Liu et al.
 677 (2020) who used slightly different compositions and calculation methods: the core
 678 becomes gradually depleted in all light elements and the equilibrium oxide budget is
 679 dominated by MgO. Comparing DED to DEE, the only significant change is that the
 680 equilibrium Mg core composition and precipitation rate dw_{MgO}^c/dT are increased by
 681 a factor of 3 and 2 respectively. Indeed, for the DED case the results are very similar
 682 to those for pure Mg partitioning (Figure 4) because the larger MgO concentration
 683 preferred in the multi-component case is offset by the larger equilibrium core O
 684 concentration. The increased w_{MgO}^c in the exchange reaction arises because of the
 685 increased MgO content of the BMO, while the FeO concentration is about the same
 686 as assumed in Figure 4 when considering only MgO partitioning (see equation (26)).

687 Figure 9 also shows for each element the temperature T_o below which precipitation
 688 would begin given the assumed initial compositions. Since the core Mg content was
 689 assumed to be zero, Mg does not precipitate in this calculation. Si does precipitate,

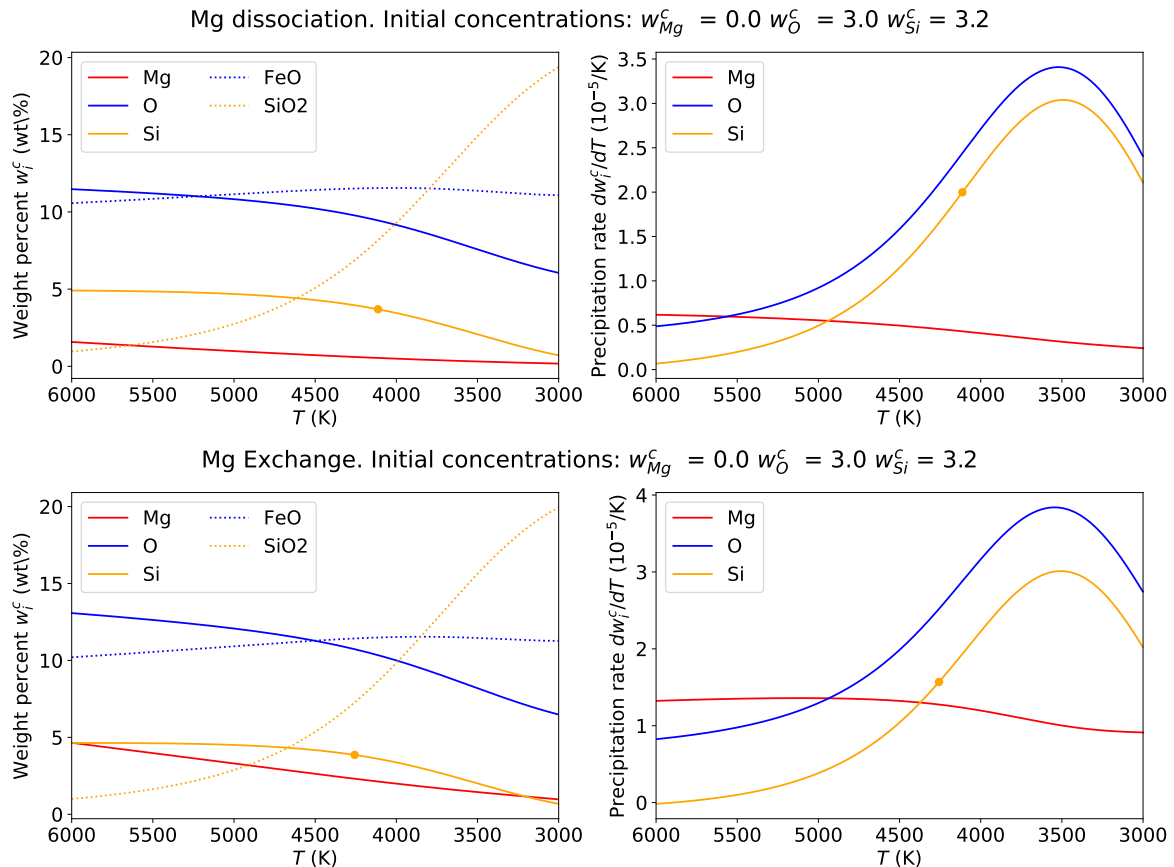


Figure 9: Equilibrium concentrations (left) and precipitation rate (right) for core elements and BMO oxides assuming the DED reaction set (top) and DEE reaction set (bottom). Dots mark the temperature at which the equilibrium core composition for element i falls below its concentration in the core.

690 but only once the CMB temperature has fallen below its current value of ~ 4000 K.

691 O never precipitates above 4000 K in all calculations we have undertaken.

692 Figure 10 compares equilibrium Mg concentrations and precipitation rates for
 693 three recent studies using the DEE Case. For direct comparison we have also re-
 694 produced a calculation where the O'Rourke and Stevenson (2016) parameters are all
 695 reduced by 0.25σ , where σ is the standard deviation quoted in their Extended Table
 696 1. The results for the Du et al. (2019) and O'Rourke and Stevenson (2016) 0.25σ

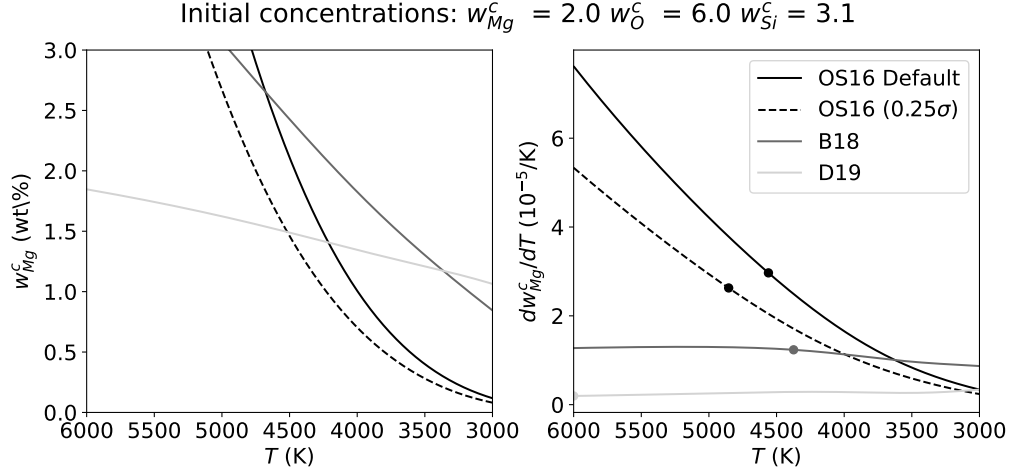


Figure 10: Equilibrium Mg concentration w_{Mg}^c (left) and Mg precipitation rate dw_{Mg}^c/dT (right) plotted as functions of temperature T for the DEE reaction set. Parameters are from O’Rourke and Stevenson (2016, O16), Badro et al. (2018, B18) and Du et al. (2019, D19). Also shown is a case where the O’Rourke and Stevenson (2016) parameters are all reduced by 0.25σ , where σ is the standard deviation quoted in their Extended Table 1. Dots mark the temperature at which the equilibrium core composition for element i falls below its concentration in the core.

697 parameters are very similar to those reported in Figure 3a of Du et al. (2019), which
 698 is encouraging as we have used different methods to compute the equilibrium con-
 699 centrations. The results using the Badro et al. (2018) parameters differ from those
 700 reported by Du et al. (2019), probably because we are considering the exchange
 701 reaction, which increases w_{Mg}^c as shown in Figure 9.

702 Figure 11 shows the equilibrium concentrations for Mg and Si and the Mg pre-
 703 cipitation rate for the three different Cases and three initial oxide compositions cor-
 704 responding to an MgO-rich, FeO-rich and SiO₂-rich BMO. There are three main
 705 messages from this Figure. First, the combination of reactions is crucial for deter-
 706 mining both T_o and dw_{Mg}^c/dT ; for certain BMO compositions dw_{Mg}^c/dT varies by
 707 over an order of magnitude, while Mg precipitation can begin anywhere between
 708 6000 K and 4000 K. Second, the initial BMO composition is generally less important

709 for determining dw_{Mg}^c/dT , with variations of up to a factor of 2 – 3, but is critical
710 for determining T_o . Third, dw_{Mg}^c/dT is not a monotonic function of T , though it
711 is usually close to its maximum value when $T = T_o$. Finally, note that changing
712 core composition does not significantly affect the basic evolution because all activity
713 coefficients have been set to 1, but it does change the precipitation time. However,
714 the results in Section 3 suggest this is not generally the case and more complex
715 behaviour can be expected when the effect of compositional variations on the distri-
716 bution coefficients are taken into account.

717 Figure 12 provides a synthesis of the multi-component precipitation results; it
718 shows the temperature T_o below which precipitation begins and the precipitation
719 rate at T_o for Mg and Si. In all calculations we have used an initial 2 wt% Mg in the
720 core and so the values of T_o are probably at the upper end of viable estimates based
721 on core formation studies. As shown by Mittal et al. (2020), the onset and rate of
722 precipitation depend sensitively on several factors including the initial compositions
723 and equilibrium constants. dw_{Mg}^c/dT spans the range $0.3 - 3 \times 10^{-5} \text{ K}^{-1}$, which
724 is broadly consistent with the results above considering pure Mg partitioning, while
725 dw_{Si}^c/dT spans the range $0.1 - 8 \times 10^{-5} \text{ K}^{-1}$. These rates are sufficient to provide
726 significant gravitational power to the dynamo as will be shown below. There is
727 a large spread of T_o values in both cases; however, most models favour onset of
728 Mg precipitation at or below 5000 K while Si precipitation tends to begin at or
729 below 4500 K. O’Rourke and Stevenson (2016) and Badro et al. (2016) also found a
730 delayed onset of precipitation. The results in Section 3.2 suggest that accounting for
731 composition-dependence reduces both T_o and dw_i^c/dT and so we regard the values in
732 Figure 12 as upper estimates based on presently available information. This suggests
733 that precipitation began after core formation; before this time, light elements would
734 have entered the core, providing a mechanism to stably stratify the upper core.

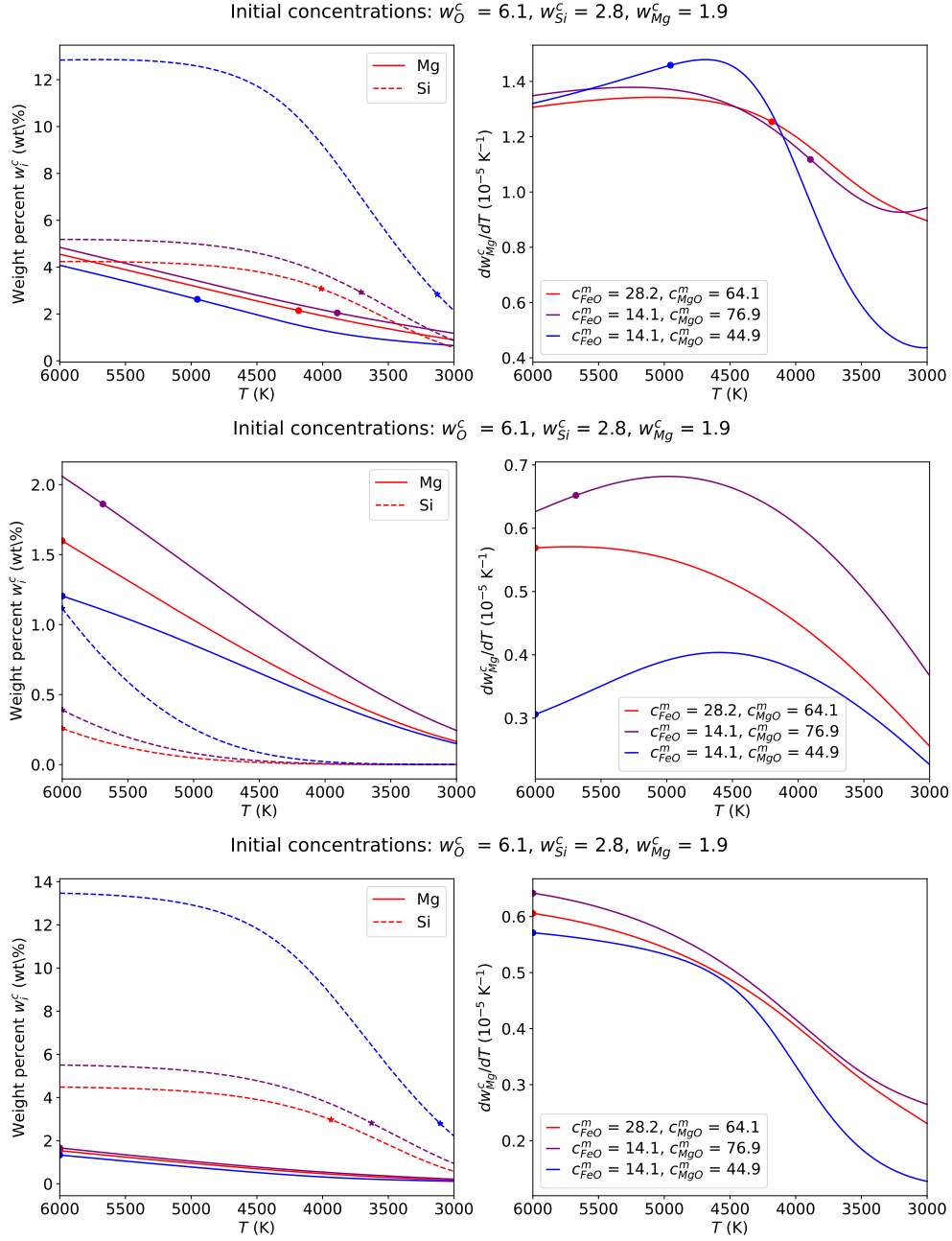


Figure 11: Equilibrium Mg and Si concentrations (left) and Mg precipitation rate dw_{Mg}^c/dT (right) plotted as functions of temperature for Cases DEE (top), DDD (middle) and DED (bottom) described in the text. Dots mark the temperature at which the equilibrium core composition for element i falls below its concentration in the core.

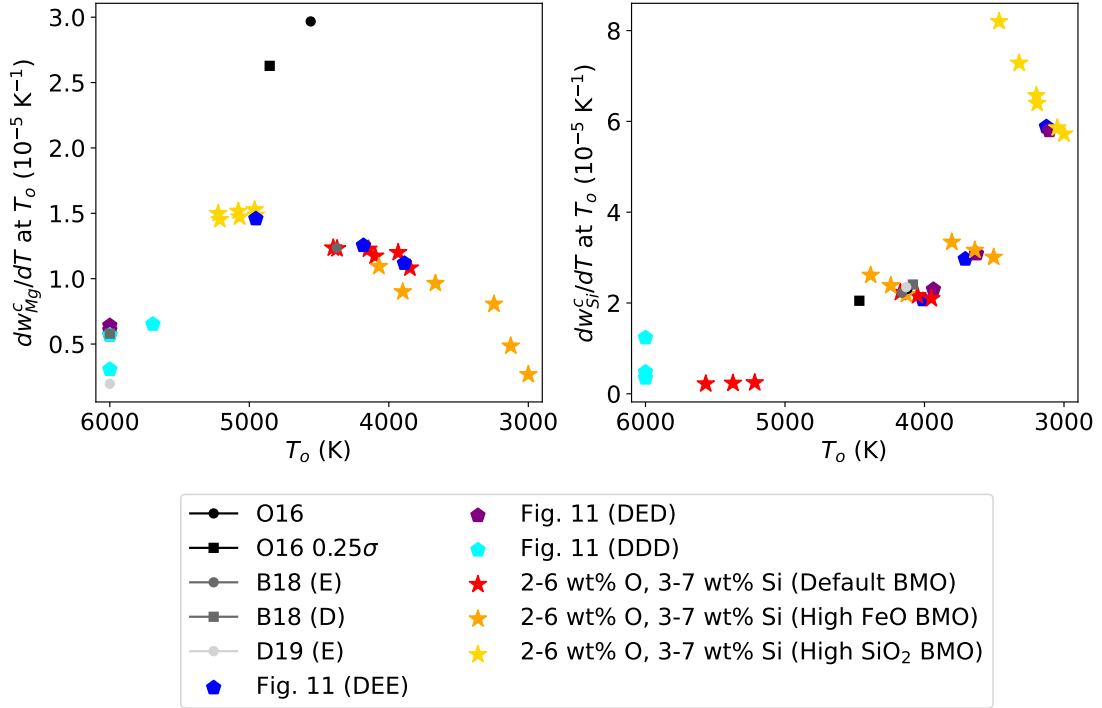


Figure 12: Precipitation rate of Mg (left) and Si (right) at the time T_o when precipitation began. The corresponding value of T_o is shown on the horizontal axis. All calculations have used an initial Mg core concentration of 2 wt%. Results for O'Rourke and Stevenson (2016, O16), Badro et al. (2018, B18) and Du et al. (2019, D19) are from Figure 10 except for the B18 Dissociation (D) case. The results denoted by stars have a default BMO composition of 28 mol% FeO, 64 mol% MgO and 8 mol% SiO₂. The results denoted by pentagons are from Figure 12.

735 4. Stratification below the CMB

736 4.1. Modern-day Observations of Stratification

737 Observational constraints on the presence of stratification at the top of the core
738 have primarily originated from seismic studies. A number of SmKS wave studies (Lay
739 and Young, 1990; Garnero et al., 1993; Helffrich and Kaneshima, 2010; Kaneshima,
740 2018) find a P-wave velocity reduction and steeper P-wave gradient relative to PREM
741 up to 400km deep into the core. The strength of stratification is often measured by
742 the Brunt-Väisälä period

$$T_{\text{BV}} = \frac{2\pi}{N} = 2\pi \left(-\frac{g}{\rho} \frac{\partial \rho'}{\partial r} \right)^{-1/2}, \quad (30)$$

743 which determines the period of oscillations that arise when a fluid parcel in a stratified
744 region is subjected to vertical displacement. Here the equation defines the Brunt-
745 Väisälä frequency N and a prime denotes the non-hydrostatic part of density ρ .
746 Matching a compositional model to the observed wavespeeds suggests $T_{\text{BV}} = 1.6-3.4$
747 hours, implying strong stratification (Helffrich and Kaneshima, 2010). Alexandrakis
748 and Eaton (2010) argued that stratification is absent at the top of the core; how-
749 ever, van Tent et al. (2020) showed that the Alexandrakis and Eaton (2010) data
750 do not conflict with a low velocity region in the uppermost core, suggesting that
751 methodological differences are responsible for the divergent conclusions. Irving et al.
752 (2018) have derived a new 1D core reference model using normal mode centre fre-
753 quencies, which provide a more direct constraint on density than body waves. The
754 model suggests a lower P-wave velocity and higher density than PREM throughout
755 the core thus reducing, though not eliminating, the stratification signal. van Tent
756 et al. (2020) recently conducted an extensive review and concluded that “both seis-
757 mological body-wave and normal mode observations require a low-velocity outermost

758 core with respect to PREM, as well as a steeper velocity gradient than PREM". Ev-
759 idently, there is now a reasonable degree of support for anomalous seismic velocity
760 structure in the uppermost core.

761 At present it is not clear whether low seismic velocities in the upper core are a
762 global or local feature. The SmKS data coverage is rather heterogeneous, with large
763 regions of the uppermost core (e.g. under North America and the Indian ocean) not
764 sampled by available raypaths (see Kaneshima, 2018). The distinction is crucial. Low
765 velocities (with respect to PREM) reflect variations in either density or bulk modulus.
766 If a global layer of anomalous fluid exists at the top of the core then this layer must
767 be light, otherwise it would mix back into the bulk core. This implies that the
768 velocities must reflect a greater decrease in bulk modulus than density, for example
769 due to enrichment in one or more light elements (Helfrich, 2012; Komabayashi, 2014;
770 Brodholt and Badro, 2017). On the other hand, if the velocity anomalies are local
771 then there is no stability requirement since the anomalies could sample part of a
772 large-scale circulation pattern (Mound et al., 2019). However, in both cases the
773 seismic velocities imply thermo-chemical anomalies greater than those associated
774 with core convection (Helfrich and Kaneshima, 2010) and so some other mechanism
775 is required to explain their existence.

776 Observations of the geomagnetic secular variation have been used to search for
777 radial motion near the top of the core, which is expected to be absent in a stable
778 layer. In purely horizontal flows, local extrema in the radial magnetic field are time
779 invariant (Whaler, 1980); however, this test for stratification renders inconclusive
780 results owing to large uncertainties on estimates of the CMB field at a point (Whaler,
781 1986). Gubbins et al. (2007) showed that the present evolution of the south Atlantic
782 anomaly, when attributed to flux expulsion, strongly suggests radial flow in the top
783 100 km of the core, while Amit (2014) argued that the mobility of high-latitude

784 flux patches is best explained by localised downwelling. Lesur et al. (2015) inverted
785 for the fluid flow at the top of the core and found that purely horizontal flow is not
786 compatible with satellite observations of recent field variations but that a very limited
787 amount of radial motion (comparable to diffusion, which was ignored) allows for
788 acceptable fits. All of these studies neglected magnetic diffusion (following Roberts
789 and Scott, 1965); however, diffusion is not necessarily negligible and potentially could
790 explain much of the observed variation (Metman et al., 2019), negating the need for
791 radial fluid flow to explain the temporal features of the field. Furthermore, steady
792 flow over CMB topography in a stably stratified layer can induce radial motion (Glane
793 and Buffett, 2018), complicating attempts to rule out stratification by searching for
794 radial flow.

795 Buffett (2014) has shown that simple combinations of axisymmetric Magneto-
796 Archimedian-Coriolis (MAC) waves in a stably stratified layer can explain a 60-yr
797 periodic variation of the dipole geomagnetic field and the recent time-dependent
798 evolution of zonal flow at the top of the core. The inferred stratified layer thickness
799 is 130 – 140 km with a maximum $N/\Omega \sim 1$ (Buffett et al., 2016) or $T_{\text{BV}} \sim 24$ hrs,
800 implying weaker stratification than inferred from seismology. Subsequent work has
801 shown that these waves can be generated by underlying core convection (Jaupart and
802 Buffett, 2017) and exchange some angular momentum with the mantle though not
803 enough to explain decadal variations in length-of-day (Holme and de Viron, 2013;
804 Buffett et al., 2016). Thus far, models based on MAC waves have assumed a global
805 stable layer at the top of the core.

806 Another approach to investigating present-day stratification is to calculate the
807 radial variation of buoyancy sources within the core (Davies and Gubbins, 2011;
808 Gomi et al., 2013; Nimmo, 2015a). This method uses energy and mass conservation
809 to balance the CMB heat flow against the sum of power sources inside the core (as

810 outlined in Section 2.2). The core is assumed to be 1D and so stratification implicitly
 811 arises in the form of a layer. Stratification requires that

$$\alpha_T \left(\frac{dT}{dr} - \frac{dT_a}{dr} \right) + \alpha_i^c \frac{dw_i^c}{dr} > 0, \quad (31)$$

812 (Landau and Lifshitz, 1987) which serves to define the base of the layer. Here r is
 813 radius, T and T_a are the temperature and adiabatic temperature respectively and
 814 barodiffusion has been ignored. The main challenge is approximating the gravita-
 815 tional energy since the spatial distribution of ohmic and viscous dissipation is not
 816 known (Jackson and Livermore, 2009), so various approaches have been used in the
 817 literature (see Davies and Gubbins, 2011; Gomi et al., 2013, for detailed discussion).
 818 Pozzo et al. (2012) used high k and found stable layers up to $O(1000)$ km thick
 819 depending on the imposed CMB heat flow. Gubbins et al. (2015) calculated a maxi-
 820 mum present-day stable layer thickness of 740 km assuming high k and no dissipation
 821 available to generate the magnetic field; however, they dismiss such thick layers as
 822 being incompatible with geomagnetic secular variation.

823 The “buoyancy” approach to assessing present-day stratification is sensitive to
 824 a number of uncertain parameters including the CMB heat flow and ICB density
 825 jump, but also the depth dependence of thermal conductivity. Labrosse et al. (2015)
 826 calculated convective heat flow using the k profiles from Gomi et al. (2013) and
 827 Pozzo et al. (2012), the latter of which has a slightly shallower gradient. For mildly
 828 superadiabatic Q^c the Gomi et al. (2013) $k(r)$ suggests a stratified region within
 829 the core, whereas the Pozzo et al. (2012) $k(r)$ predicts no stratification anywhere.
 830 The present uncertainty on $k(r_c)$ (Section 2.3), let along $k(r)$, currently prevents
 831 definitive conclusions on the presence of stratified regions within the bulk core.

832 Overall there is support from seismology for strongly stratified regions up to

833 400 km thick at the top of the core. The geomagnetic observations paint a more
834 complex picture and seem to prefer thinner stratified regions or no stratification at
835 all. The observations also do not determine whether the stratification is regional
836 or in the form of a global layer. We therefore turn to computational methods for
837 investigating core stratification. There are two main approaches: direct numerical
838 simulations (DNS, Section 4.2) represent the spatio-temporal interactions between
839 core flow, stratification and magnetic field on centennial to millennial timescales,
840 but have stable layers imposed; parameterised models (Section 4.3) investigate the
841 Gyr timescale formation and evolution of stable layers, but only determine the radial
842 thickness and strength of stratification. The stratification derives from some combi-
843 nation of thermal and chemical effects and so below we consider these possibilities
844 in turn, focusing on the key issues that will help distinguish between the myriad
845 scenarios. In particular we aim to shed light on the following questions: How did the
846 stratification form? How has the stratification evolved over time? What is the pre-
847 dicted present-day thickness and stratification strength? Is the stratification global
848 or local?

849 *4.2. Direct Numerical Simulations (DNS) and Theory*

850 There is a growing consensus from DNS that strong and thick stable layers are
851 incompatible with the morphology of the present magnetic field. Olson et al. (2017),
852 Olson et al. (2018), Christensen (2018) and Yan and Stanley (2018) performed DNS
853 with thermal and compositional effects combined into a single co-density (see Bra-
854 ginsky and Roberts, 1995) and imposed a variety of CMB co-density gradients, both
855 homogeneous and heterogeneous, promoting varying degrees of stabilising density
856 gradients. Olson et al. (2017) and Olson et al. (2018) examined over 60 dynamo
857 solutions and found that the high-latitude field morphology and the ratio of normal

858 to reversed CMB flux are sensitive to the degree of stratification. They concluded
 859 that a weakly stratified 400-km-thick layer layer with $N_0/\Omega \sim 0.5$ ($T_{\text{BV}} \sim 12$ hrs) is
 860 compatible with the simulation results, where

$$\frac{N_0}{\Omega} = \frac{1}{\Omega} \left(\alpha_{\text{T}} g \frac{\partial T'}{\partial r} \right)^{1/2} \quad (32)$$

861 is the Brunt-Väisälä frequency derived from thermal variations only. Christensen
 862 (2018) considered 26 simulations with N_0/Ω in the range 2.4 – 4. He applied the
 863 morphological criteria defined in Christensen et al. (2010) and found that simulations
 864 with 400-km-thick layers were only marginally compatible with the modern field.
 865 Yan and Stanley (2018) showed that the ratio of zonal dipole to octupole Gauss
 866 coefficients, g_3^0/g_1^0 , is sensitive to the presence of a stable layer. From 33 simulations
 867 they found that matching both Earth’s g_3^0/g_1^0 over the last 10 kyrs (obtained from
 868 the CALS10K.2 model of Constable et al., 2016) and the modern field (according
 869 to the Christensen et al. (2010) criteria) entails a trade-off between stratification
 870 strength and thickness. Their preferred solutions had layer thicknesses in the range
 871 60 – 130 km and $N_0/\Omega < 1$. Recently Gastine et al. (2020) modelled thermal
 872 stratification in a suite of 70 simulations with $0 \leq N_0/\Omega \leq 50$ and found that CMB
 873 fields become more dipolar and axisymmetric with increasing layer thickness, in
 874 line with previous studies (Christensen, 2006; Nakagawa, 2011), and hence generally
 875 do not match the modern geomagnetic field (again as assessed by the Christensen
 876 et al. (2010) criteria). They therefore argued against the presence of stratification in
 877 Earth’s core.

878 A number of the aforementioned studies combined an imposed stable layer with
 879 lateral heat flow variations on the CMB. When the stratification is weak the lateral
 880 variations can induce flow at the CMB (Olson et al., 2017), effectively overcoming

881 the mean stabilising codensity gradient in local regions where the CMB heat flow is
882 anomalously high. However, for thick imposed layers, as the stratification strength
883 increases the influence of the lateral variations is strongly diminished and the stable
884 layer behaviour is relatively unaffected by their presence (Christensen, 2018). Using
885 a simple model of non-magnetic thermal convection, Cox et al. (2019) showed that
886 the transition between these two regimes (boundary-dominated and stratification-
887 dominated) arises when the stratification parameter S , defined as the relative size of
888 boundary temperature gradients to imposed vertical temperature gradients, exceeds
889 unity. However, given uncertainties in estimating S for Earth they were unable to
890 conclude whether the core is currently in the high S or low S regime.

891 Lateral heat flow variations can induce regional stratification even when the mean
892 CMB heat flow is destabilising. Mound et al. (2019) found that thick localised stable
893 regions were ubiquitous in a large suite of non-magnetic simulations that access the
894 regime of rapid rotation and vigorous convection thought to be most relevant to
895 Earth’s core (Long et al., 2020). In these simulations the lateral extent of the stable
896 regions is set by the imposed boundary anomalies (which were derived from seismic
897 tomography) rather than the small scale motions associated with vigorous convection
898 in the bulk of the core. Interestingly, 1D averaging in these models can yield a net
899 stabilising temperature gradient, giving the impression of global stratification despite
900 the presence of motion in regions of the upper core. Using scaling analysis Mound
901 and Davies (2020) estimated that stable regions in Earth’s core could extend up to
902 350 km depth, similar to the thick layers inferred from seismology. They obtained
903 values of $N_0/\Omega \approx 2 - 5$, corresponding to $T_{\text{BV}} \sim 5 - 12$ hrs, lower than estimates
904 by Helffrich and Kaneshima (2010) but larger than that inferred from MAC waves
905 (Buffett et al., 2016).

906 A variety of processes besides lateral heat flow variations can act to disrupt or

907 even completely erode a pre-existing stable layer. It is well known from oceanography
908 and astrophysics (Turner, 1973; Garaud, 2018) that stable systems where thermal
909 and compositional fields have different diffusivities and adverse gradients are prone
910 to instabilities that can drastically change their behaviour. These “double-diffusive”
911 instabilities have recently begun to receive substantial attention in the planetary
912 core context (Monville et al., 2019; Bouffard et al., 2020; Mather and Simitev, 2020).
913 Heat diffuses faster than light elements in the core (Pozzo et al., 2013) and so the
914 double diffusive dynamics take the form of ‘oscillatory convection’ if the chemical
915 gradient is stabilising and the thermal gradient is destabilising; switching the signs
916 of the gradients gives ‘finger convection’ (Turner, 1973). The relevant configuration
917 for Earth’s core may have varied over time.

918 As described in more detail in Section 4.4 below, chemical stratification may
919 have originated early in Earth’s history, either due to incomplete mixing during core
920 formation (Landeau et al., 2016; Jacobson et al., 2017) or via enrichment in FeO from
921 the mantle (Buffett and Seagle, 2010; Davies et al., 2020, and also Section 3.3). In
922 the absence of precipitation, thermal convection was needed to power the geodynamo
923 prior to inner core formation 0.5 – 1 Gyrs ago (Nimmo, 2015a, and Table 1) and
924 so thermal stratification should be a relatively recent feature. The core may have
925 become thermally stratified below the CMB once precipitation began; however, the
926 assessment in Section 3.4 suggests this was after core formation and so thermal
927 convection would have been needed to power the dynamo before the core cooled
928 to ~ 5000 K. In this case the appropriate regime for modelling double diffusion in
929 the early core is “oscillatory” convection (Bouffard et al., 2020). Depending on the
930 strength of chemical stability and the Lewis number $Le = \kappa/D_i$, the ratio of thermal
931 and chemical diffusion coefficients, large-scale secondary instabilities can emerge in
932 the form of staircases or coherent vortices (Garaud, 2018; Monville et al., 2019).

933 The relevant configuration for the present day depends on the CMB heat flow
934 and the survival of any primordial chemical layer. The total heat Q extracted from
935 the core at present is estimated at 7 – 17 TW (Nimmo, 2015a) while the adiabatic
936 heat flow is around $Q_a = 14 - 16$ TW (Davies et al., 2015) and so both thermally
937 stable ($Q^c < Q_a^c$) and unstable ($Q^c > Q_a^c$) conditions are consistent with available
938 constraints. If chemical layers do survive then the configuration is either in the
939 oscillatory regime or is completely stratified if $Q^c < Q_a^c$, though the enrichment of
940 the liquid in light elements due to inner core growth provides a potential destabilising
941 mechanism. If chemical layers do not survive then any stable layer must be thermally
942 stratified ($Q^c < Q_a^c$), while composition is destabilising due to chemical convection
943 arising from inner core growth. This system is in the ‘finger’ regime and can exhibit
944 secondary instabilities in the form of large-scale zonal flows (Monville et al., 2019).

945 At present, it seems premature to apply the results of double-diffusive DNS stud-
946 ies to Earth’s core. The simulations are extremely challenging because the value of
947 $Le \sim 1000$ in Earth’s core (Pozzo et al., 2013), which induces a large scale disparity
948 between thermal and compositional fields. This difficulty has also prompted workers
949 to invoke further simplifications, such as omitting the magnetic field (Monville et al.,
950 2019) or imposing double diffusive conditions throughout the core (rather than just
951 near the CMB) (Mather and Simatev, 2020). Finally, all current simulations are far
952 from the rapidly rotating and low viscosity conditions of the core and robust scaling
953 relationships of the kind that have recently been devised for the single-component
954 system (Aubert et al., 2017; Wicht and Sanchez, 2019) have not yet been produced
955 for the double-diffusive case. This area of research will undoubtedly see significant
956 progress in the coming years.

957 Stable layers can be influenced by penetration from the underlying convection.
958 Takehiro and Lister (2001) studied penetration of rapidly rotating non-magnetic

959 convection underlying a stable layer and found that the penetration depth scales as
960 $\ell_s(N/\Omega)^{-1}$, where ℓ_s is the characteristic flow scale. Gastine et al. (2020) have found
961 good agreement with the Takehiro and Lister (2001) scaling in numerical simulations
962 when N is calculated as the mean over the stable region. At the layer interface
963 Gastine et al. (2020) found that ℓ_s is comparable to the lengthscale for the onset
964 of convection, in which case the penetration depth is only a few hundred metres.
965 Gubbins and Davies (2013) obtained a similar result by a different line of reasoning.

966 A related issue is whether turbulent convection can erode a stable layer by en-
967 training buoyant fluid into the bulk. This problem has been studied extensively
968 in oceanography (e.g. Levy and Fernando, 2002), but has only recently been stud-
969 ied in the context of Earth’s core. Bouffard et al. (2020) considered the erosion of a
970 thick (~ 700 km) pre-existing chemically enriched layer by thermal convection in non-
971 magnetic simulations representative of an early Earth (no inner core). They found
972 greater erosion in the equatorial plane than near the poles and estimated erosion rates
973 (represented as the rate of change of stable layer thickness) of only ~ 1 km Gyr $^{-1}$
974 or less, despite considering the end member case of zero chemical diffusion. Only in
975 a subset of their models do they find developed double diffusive convection, which
976 they propose would become more prevalent in their simulations as the Ekman num-
977 ber further lowers towards predicted values for Earth. Interestingly Bouffard et al.
978 (2020) find that an initial overshoot in kinetic energy in their simulations causes
979 massive entrainment of the layer. This could simply reflect transient evolution from
980 an arbitrary initial condition, though future work may consider whether physical
981 effects (e.g. a giant impact) could produce similar behaviour.

982 Gubbins and Davies (2013) considered whether a chemically stable layer could be
983 mixed by the Kelvin-Helmholtz instability. The sufficient condition for an inviscid
984 and non-magnetic stratified fluid to be stable to Kelvin-Helmholtz instability is that

985 the local Richardson number

$$986 \quad Ri = \frac{N^2}{(dU/dz)^2} > 1/4, \quad (33)$$

987 where U is the flow speed and z the vertical coordinate. Both N and the shear
988 (dU/dz) vary with depth and cannot be observed directly in Earth's core. Gubbins
989 and Davies (2013) assumed a constant value of (dU/dz) throughout the layer inferred
990 from core flow models (Holme, 2007) and used the approximately linear form of N
991 obtained for a layer formed by barodiffusion, concluding that the layer is stable
992 everywhere except in the bottom few km. We expect a similar result for other layer
993 formation mechanisms for which N is approximately linear across the layer (Buffett
994 and Seagle, 2010; Buffett, 2014).

995 Overall, numerical dynamo simulations incorporating global stratification that
996 have attempted to match geomagnetic observations tend to favour thinner and more
997 weakly stratified layers than those inferred from seismology. Some studies have also
998 argued against the presence of a stable layer. A clearer understanding of the role of
999 double diffusive instabilities, and particularly the attendant generation of large-scale
1000 flows, is necessary before more definitive conclusions can be drawn. Most current
1001 studies do agree that existing layers are stable to penetration, entrainment, inter-
1002 face instabilities and lateral variations in CMB heat flow. Regional stratification is
1003 another possibility, offering a plausible framework for producing both the significant
1004 compositional anomalies suggested by seismic studies and the upwelling flow near
the top of the core that is preferred by a number of geomagnetic studies.

1005 *4.3. Evolution of Thermal Stratification*

1006 The evolution of the core over the age of the Earth is usually investigated using
 1007 thermal history models. These models assume spherical symmetry and use global
 1008 conservation of energy and entropy to solve for the core cooling rate and hence the
 1009 power that is available to generate the magnetic field (see Nimmo, 2015a,b, for a de-
 1010 tailed review of the methodology and standard solutions). In this approach the bulk
 1011 of the core is assumed to be hydrostatic, adiabatic and compositionally well-mixed,
 1012 while within a stable layer diffusion is assumed to control the radial temperature
 1013 and compositional profiles. When small terms are neglected (see Gubbins et al.,
 1014 2004; Nimmo, 2015a; Davies, 2015, for details) the energy balance can be written
 1015 symbolically as

$$Q^c = Q_s + Q_L + Q_g + Q_p = A \frac{dT_c}{dt}, \quad (34)$$

1016 (see Section 2.2) where dT_c/dt is the core cooling rate at the CMB. This equation
 1017 states that the CMB heat flow Q^c is balanced by the heat Q_s stored in the core, the
 1018 latent heat Q_L due to inner core freezing, the gravitational energy Q_g released as
 1019 light elements are redistributed throughout the liquid as the inner core grows, and
 1020 the gravitational energy released due to precipitation, Q_p , which arises when heavy
 1021 residual liquid downward mixes into the bulk core. The magnetic field arises in the
 1022 entropy budget, which can be written symbolically (again neglecting small terms) as

$$E_J + E_\alpha + E_k = E_s + E_L + E_g + E_p = B \frac{dT_c}{dt}. \quad (35)$$

1023 Here E_α is the entropy due to molecular diffusion of light elements, E_k is the entropy
 1024 due to thermal conduction (which depends on the thermal conductivity) and E_J
 1025 is the entropy production by Ohmic dissipation. The term E_α is negligible in this

1026 section; however, it will be important when considering FeO dissolution in Section 4.4
1027 below. We have also neglected radiogenic heating since potassium 40 is not thought to
1028 partition significantly into the core (Xiong et al., 2018). In this section we also ignore
1029 Q_p and E_p , but will reintroduce them when considering precipitation in Section 5.

1030 The main uncertainties in the calculations using equations (34) and (35) are
1031 the time evolution of the CMB heat flow Q^c , the precipitation rate (see Section 3),
1032 and the ICB density jump $\Delta\rho$ (see Section 2). The main outputs are the time
1033 evolution of the radius of the inner core, stable layer thickness and strength, and
1034 E_J , which is required to be positive for dynamo action (Gubbins et al., 2003, 2004;
1035 Nimmo, 2015a). The vast majority of previous studies have assumed that the stable
1036 layer grows downwards from the CMB and so we also make this assumption in the
1037 remainder of this section.

1038 Most previous studies of core thermal stratification have assumed a prescribed
1039 Q^c and focused on the core evolution. The key methodological differences are the
1040 numerical scheme used to solve for the time dependent growth of the layer and
1041 the choice of boundary conditions coupling the stable layer and convective region
1042 at their interface, r_s . In an early study Gubbins et al. (1982) assumed continuity
1043 of thermal gradient at r_s and a constant CMB temperature, which ensured that
1044 sub-adiabatic conditions developed at the CMB. In a simple demonstration of the
1045 physical behaviour they found a ~ 1000 km thick layer formed over 4.5 Gyrs for
1046 $k = 15 \text{ W m}^{-1} \text{ K}^{-1}$. Labrosse et al. (1997) instead modelled the moving boundary
1047 problem with a solution to a Stefan problem, which allowed both the temperature
1048 and its gradient to be continuous at r_s and the interface velocity to be determined.
1049 Imposing a linearly decreasing $Q^c(t)$ that became sub-adiabatic at ~ 1.5 Ga they
1050 obtained a ~ 600 km thick stable layer at present. Although chemical effects were
1051 neglected within the stable layer, Labrosse et al. (1997) estimated the effects of

1052 changing composition due to inner core growth may lead to destabilising chemical
1053 gradients and potentially double-diffusive “finger” instabilities. Lister and Buffett
1054 (1998) assumed that finger convection mixes light elements uniformly throughout the
1055 layer and applied continuity of density at r_s (though the light element concentration is
1056 discontinuous). With a similar parameter choice to Labrosse et al. (1997) they found
1057 the deficit of light element in the layer limits the growth of the layer to ~ 400 km.

1058 Greenwood et al. (2021) recently examined the limits to present day thermal
1059 stratification in the high conductivity scenario (Table 1) using the data from Davies
1060 et al. (2015) and a similar setup to Labrosse et al. (1997), i.e. continuity of tem-
1061 perature and temperature gradient at r_s . In the absence of radiogenic heating and
1062 precipitation, thermal convection is required to generate the magnetic field prior
1063 to inner core nucleation and so high k implies that the time during which thermal
1064 stratification may grow is limited to the last 0.5 – 1 Gyrs. Like the studies discussed
1065 in the previous paragraph, Greenwood et al. (2021) did not solve for the mantle
1066 evolution, but instead imposed a linear variation in $Q^c(t)$ following inner core for-
1067 mation as suggested by recent coupled core-mantle evolution models (Driscoll and
1068 Bercovici, 2014; Nakagawa and Tackley, 2014; Patočka et al., 2020). Considering a
1069 wide range of present day heat flows and constant dQ^c/dt values, Greenwood et al.
1070 (2021) provide upper bounds on the present day size for the layer at 700 km, which
1071 is only achieved in the most extreme scenarios.

1072 Whilst the recent trend in CMB heat flow is approximately linear, the long-term
1073 (~ 3.5 Gyrs) variation in Q^c based on published coupled models instead shows an ex-
1074 ponential decrease (Figure 13). Extrapolating their short term linear heat flows back
1075 along an exponential to 3.5 Ga, Greenwood et al. (2021) find that scenarios produc-
1076 ing present-day layers thicker than ~ 400 km would require heat flows in the ancient
1077 Earth exceeding 70 TW, significantly larger than produced by coupled evolution

1078 models in the high conductivity scenario (Driscoll and Bercovici, 2014; Nakagawa
 1079 and Tackley, 2014; Patočka et al., 2020). Filtering out models predicting > 70 TW
 1080 in the ancient core Greenwood et al. (2021) obtain upper bounds of 400 km on the
 1081 layer thickness, with minimum Brunt-Väisälä periods (peak N_0) of $T_{\text{BV}} = 8 - 24$ hrs.

1082 Strictly, the long-term evolution of Q^c and the core temperature are coupled
 1083 and should be obtained self-consistently. The presence of a stable layer will alter
 1084 the feedback between the core and mantle, although given our models only produce
 1085 temperature anomalies of ~ 10 K, the effect is likely to be insignificant. Thermal
 1086 stratification raises the core temperature above the adiabat, which increases Q^c (all
 1087 else being the same) and reduces dQ^c/dt . The same effect arises when the inner
 1088 core forms, where latent heat and gravitational energy reduce the core cooling rate
 1089 [see equation (11)], reducing dQ^c/dt . Therefore, extrapolating along an exponential
 1090 curve tied to the present day dQ^c/dt likely under-estimates the ancient Q^c . Future
 1091 coupled models of a core-mantle evolution with core stratification may therefore find
 1092 further reductions to the 400 km limit proposed by Greenwood et al. (2021).

1093 We end this section by examining stable layer properties obtained using $k = 70$
 1094 $\text{W K}^{-1} \text{m}^{-1}$ at the CMB, the lower values proposed in the ‘high’ conductivity scenario
 1095 (Table 1), complementing the results of Greenwood et al. (2021) who considered the
 1096 upper range of $k = 100 \text{ W K}^{-1} \text{m}^{-1}$ at the CMB. We repeat both the methodology
 1097 and analysis of Greenwood et al. (2021), using the same depth dependence on k given
 1098 in Davies et al. (2015) for ICB density jumps of $\Delta\rho = 600, 800$ and 1000 kg m^{-3} and a
 1099 wide range of dQ^c/dt values. A full list of parameter values is given in Table 2. Figure
 1100 14 shows the resulting present day layer thickness; grey shaded regions indicate a
 1101 super-adiabatic core and hence no stable layers, while white regions indicate models
 1102 that are rejected for not producing a magnetic field ($E_J > 0$) at all times. A wedge
 1103 in the parameter space remains where the heat flow is sub-adiabatic at present,

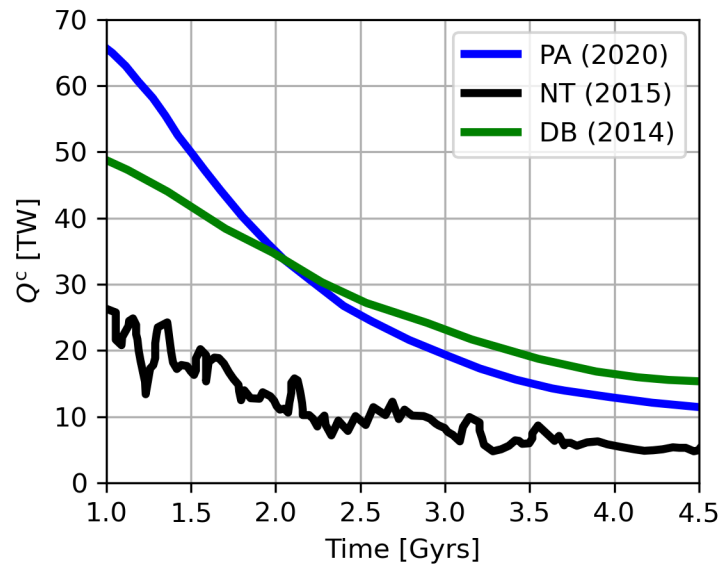


Figure 13: Published CMB heat flows from coupled core and mantle thermal history models. In the legend, PA (2020), NT (2015), and DB (2014) refer to the studies of Patočka et al. (2020, their Figure 12), Nakagawa and Tackley (2014, their Figure 9), and Driscoll and Bercovici (2014, their Figure 5) respectively.

1104 producing thermal stratification, but with a fast enough dQ^c/dt to enable super-
1105 adiabatic heat flows prior to inner core formation.

1106 Figure 14 shows that viable solutions maintaining $E_J > 0$ and matching the
1107 present ICB radius are obtained with lower values of the present day Q^c for $k =$
1108 $70 \text{ W m}^{-1} \text{ K}^{-1}$ compared to $k = 100 \text{ W m}^{-1} \text{ K}^{-1}$ due to a lower E_k in the entropy
1109 balance. Filtering out solutions that produce ancient heat flows exceeding 70 TW
1110 (see contours in Figures 14) gives a maximum layer thickness of ~ 500 km with
1111 $k = 70 \text{ W m}^{-1} \text{ K}^{-1}$ or ~ 700 km when $\Delta\rho = 1000 \text{ kg m}^{-3}$, significantly larger
1112 than the maximum thickness of ~ 400 km when $k = 100 \text{ W m}^{-1} \text{ K}^{-1}$ since the
1113 lower value of k permits lower heat flows which are proportionally further below the
1114 isentropic value. The minimum Brunt-Väisälä period (peak N_0), shown in Figure
1115 15, is not significantly different to the range in Greenwood et al. (2021) (8 – 24
1116 hours). Lowering k to $70 \text{ W m}^{-1} \text{ K}^{-1}$ shifts the value of Q^c at which stratification
1117 begins to grow; however, T_{BV} for a given ratio of Q^c/Q_a^c remains the same. Despite
1118 the range of core properties and $dQ^c(t)/dt$ values used, the strength of stratification
1119 depends predominantly on the ratio Q^c/Q_a^c at present day. Models that are mildly
1120 sub-adiabatic ($Q^c/Q_a^c > 0.8$) give periods similar to those inferred from MAC waves
1121 (Buffett et al., 2016) and comparisons of dynamo models with the magnetic field
1122 (Olson et al., 2017). Periods inferred from seismology of 1.3 – 3.5 hours (Helffrich
1123 and Kaneshima, 2010) lie outside the ranges produced by thermal stratification,
1124 which given the trend in Figure 15 would require unrealistically low heat flows.

1125 4.4. *Evolution of Chemical Stratification*

1126 Chemical stratification arises when fluid at the top of the core is enriched in one
1127 or more light elements, thus reducing the fluid density. The source for this light ele-
1128 ment enrichment must be either an internal mechanism redistributing light element

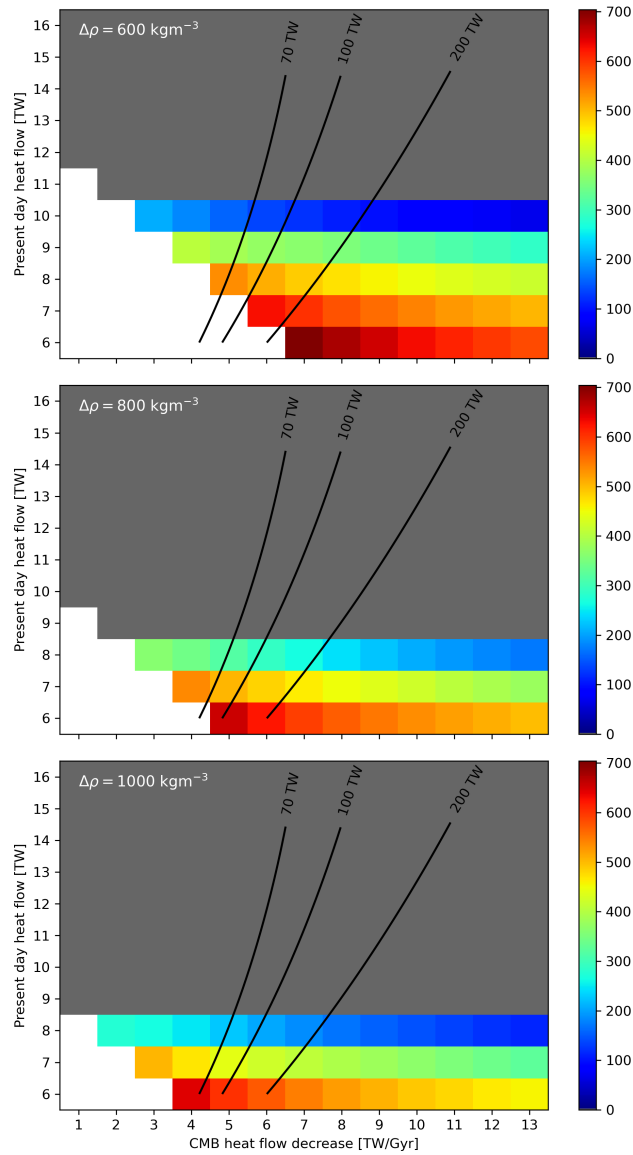


Figure 14: Present day thickness of thermally stratified layers for a parameter search across linear CMB heat flow trends and $\Delta\rho = 600, 800$ and 1000 kg m^{-3} , assuming $k = 70 \text{ W m}^{-1} \text{ K}^{-1}$ at the CMB. Grey regions are super-adiabatic at present and so produce no thermal stratification. White regions indicate solutions where positive dynamo entropy was not maintained across the duration of the run. Contours indicate the CMB heat flow at 3.5 Ga (beyond the simulation time) by extrapolating along an exponential fitted to the present day Q^c and dQ^c/dt .

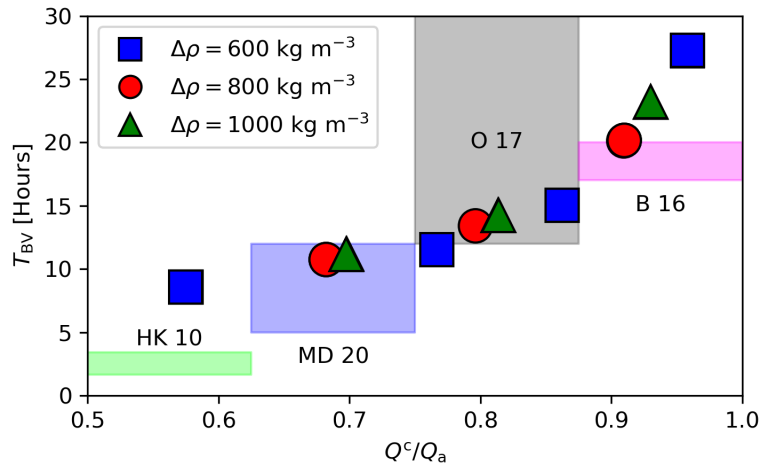


Figure 15: Buoyancy period, T_{BV} , for all models producing a stable layer, plotted as a function of the ratio Q^c/Q_a^c . Squares, circles and triangles denote the ICB density jump used as indicated in the legend. Many models of the same $\Delta\rho$ plot on top of each other since the dominant control on T_{BV} is Q^c/Q_a^c . Also shown are T_{BV} values from other studies (offset such that they do not overlap; they have no relation to the x -axis): HK 10 (Helffrich and Kaneshima, 2010), MD 20 (Mound and Davies, 2020), O 17 (Olson et al., 2017), and B 16 (Buffett et al., 2016). Note that the upper bound provided by Olson et al. (2017) stretches to infinity since they also promote models with no stratification.

1129 within the core, or an external mechanism that enables the addition of material from
1130 the mantle. Internal mechanisms include the barodiffusion of light elements along
1131 the core pressure gradient (Fearn and Loper, 1981; Gubbins and Davies, 2013), im-
1132 miscibility in the Fe-Si-O system at high pressure and temperature (Arveson et al.,
1133 2019), or the accumulation of light fluid parcels emitted from the inner core bound-
1134 ary (Moffatt and Loper, 1994; Bouffard et al., 2019). Komabayashi (2014) found
1135 that an increase in O concentration could decrease the seismic velocity in line with
1136 observations; however, Brodholt and Badro (2017) found that these simple accumu-
1137 lation mechanisms do not produce layers that are light and slow as required for a
1138 global stable layer. Instead Brodholt and Badro (2017) argue that an exchange of
1139 elements is required, for example by decreasing the Si concentration and increasing
1140 the O concentration compared to the bulk core. If one instead considers regional
1141 stratification then simple light element accumulation may not be incompatible with
1142 observations, though it is not clear how these internal mechanisms could generate
1143 enhanced chemical concentration on the scales suggested by the seismic observations.
1144 Clearly more work is required here; however, in the following we focus on external
1145 mechanisms.

1146 Two external mechanisms for chemical stratification have been proposed. Lan-
1147 deau et al. (2016) used analogue experiments to argue that a stable layer of compa-
1148 rable thickness to seismic inferences could have been emplaced towards the end of
1149 core formation due to turbulent mixing between a light-element-enriched impactor
1150 and the proto-core. Jacobson et al. (2017) showed that changing equilibrium condi-
1151 tions during multi-stage core formation can lead to the formation of stable chemical
1152 layering. Their results indicate that the stable layer could be erased by a late giant
1153 impact, such as the hypothesised moon-forming event, though Bouffard et al. (2020)
1154 argue based on the results of Landeau et al. (2016) that the mixing efficiencies as-

1155 sumed by Jacobson et al. (2017) are too high and hence the stratification would
1156 have survived. A resolution to this issues awaits improved physical descriptions and
1157 observational constraints on core formation processes.

1158 The second external mechanism for stratifying the upper core is through chemical
1159 interactions with the mantle. As established in Section 3 and originally shown by
1160 Frost et al. (2010) and Buffett and Seagle (2010), the core has likely been under-
1161 saturated in oxygen for much of its history and has therefore become progressively
1162 enriched in O at the CMB. Other elements such as Si and Mg may also have entered
1163 the core following its formation; however, the uncertainties are currently significant
1164 (see Section 3) and so here we focus on FeO partitioning.

1165 The early core was probably susceptible to “oscillatory” double diffusive insta-
1166 bilities whereby radial oscillations develop into distinct convecting staircases (see
1167 Turner, 1973, and Section 4.2). Buffett and Seagle (2010) modelled the long term
1168 evolution of an oxygen enriched layer arising from a balance of the diffusive growth
1169 and convective entrainment due to staircases. They show that the amount of light
1170 element entrained into the bulk core is small relative to the inward diffusive flux of
1171 O at the CMB, which leads to the chemical layer growing to around 70 km in 4.5
1172 Gyrs for a diffusivity of $D_O = 3 \times 10^{-9} \text{ m}^2 \text{ s}^{-1}$. The growth is interrupted when the
1173 inner core forms since release of O at the ICB enriches the convecting fluid, however
1174 this only reduces the layer size by ~ 10 km. Buffett and Seagle (2010) assumed a
1175 prescribed thermal evolution for the bulk core comprising a linear decrease in T and
1176 inner core growth $\propto \sqrt{t}$ which, whilst reasonable choices for their initial study, omits
1177 any feedback from the stable layer evolution on the evolution of the bulk core. In par-
1178 ticular, Buffett and Seagle (2010) did not estimate the dynamo entropy E_J , which is
1179 important for ensuring that the calculated core history complies with paleomagnetic
1180 constraints.

1181 Nakagawa (2018) adapted the model of Buffett and Seagle (2010), coupling it to
1182 the evolution of the bulk core, allowing feedback between the two regions. They found
1183 similar layer thicknesses to Buffett and Seagle (2010) since the enhanced oxygen
1184 concentrations give large density anomalies that are relatively insensitive to the heat
1185 loss of the core. Since it is assumed that diffusion primarily controls the evolution of
1186 the layer, the layer size is approximately $\propto \sqrt{D_O t}$, which Nakagawa (2018) confirms
1187 using a range of O diffusivities up to $D_O = 4.8 \times 10^{-8} \text{ m}^2 \text{ s}^{-1}$. They obtained
1188 positive E_J using the entropy balance formulation of Labrosse et al. (2015) for layer
1189 thicknesses up to 270 km. In Labrosse et al. (2015), the entropy change due to mass
1190 diffusion, E_α , is not included which is reasonable when considering just the well-
1191 mixed core (Gubbins et al., 2004); however, strong gradients in chemically enriched
1192 layers mean that E_α is no longer negligible as we will show below.

1193 Buffett and Seagle (2010) and Nakagawa (2018) both assume that mantle convec-
1194 tion continually enriches the CMB in oxygen, such that the appropriate boundary
1195 condition is an imposed (time-varying) O concentration at the CMB. On the other
1196 hand, it seems plausible that either advection or diffusion in the mantle limit the
1197 replenishment of O-depleted material at the CMB (Davies et al., 2018). Taking op-
1198 timistic estimates of $D_{FeO}^m = 10^{-12} \text{ m}^2 \text{ s}^{-1}$ for the diffusion coefficient of FeO in
1199 the solid mantle (Ammann et al., 2010) and a 20 mol% change in FeO composition
1200 across the chemical boundary layer in the lower mantle, Davies et al. (2018) obtained
1201 a chemical mass flux of $I_{FeO} \sim 1000 \text{ kg s}^{-1}$. This value is comparable to the flux
1202 due to barodiffusion (Gubbins and Davies, 2013), which produces a $\sim 10\%$ change
1203 in concentration at the top of the core over 4.5 Gyrs, a relatively small effect. A
1204 similar result is obtained when considering the (Stokes) rise time of a buoyant parcel
1205 of mantle material away from the CMB. The actual timescale for the Rayleigh-Taylor
1206 instability is more complex and depends on various uncertain quantities such as the

1207 lengthscale of the instability and the viscosity contrast between enriched and de-
 1208 pleted layers (Ribe, 1998). Nevertheless, existing studies suggest that it is difficult
 1209 to produce significant FeO flux through the solid mantle.

1210 The high early core temperatures suggested by thermal history models with $k \sim$
 1211 $100 \text{ W m}^{-1} \text{ K}^{-1}$ (Nimmo, 2015a; Davies, 2015; Labrosse et al., 2015) suggest that
 1212 the presence of melting in a BMO should significantly enhance chemical exchange
 1213 with the core (Brodholt and Badro, 2017). Davies et al. (2020) used the data of
 1214 Pozzo et al. (2019) to model FeO exchange between the upper core and a BMO,
 1215 extending the model of Labrosse et al. (2007). They found that the upper core could
 1216 become strongly enriched in FeO (sometimes reaching a pure FeO composition) with
 1217 stable layers of 70 – 80 km thickness growing in the first 1 Gyr of evolution before
 1218 reaching up to 150 km thickness at the present day. Furthermore, they found that
 1219 FeO loss increased the freezing rate of the BMO in order to keep the region on the
 1220 liquidus. Complete freezing of the BMO occurred in the first 1 – 3 Gyrs following
 1221 core formation and hence the BMO did not survive to the present day, contrasting
 1222 with the original results of Labrosse et al. (2007).

1223 Davies et al. (2020) did not calculate the entropy production E_J in the core
 1224 and hence could not show that their FeO evolution models were consistent with the
 1225 existence of a dynamo for the past 3.5 Gyrs. In order to calculate E_J it is important
 1226 to account for the entropy E_α due to molecular diffusion, which is given by

$$E_\alpha = \int \frac{i^2}{\alpha_i^D T} dV, \quad (36)$$

1227 (Gubbins et al., 2004). All else being equal, equation (35) shows that an increase in
 1228 E_α reduces E_J , limiting the power available to the geodynamo. We have repeated
 1229 the calculations from Davies et al. (2020), using the same formulation for the BMO

1230 evolution (following Labrosse et al., 2007), but with an altered core model. In Davies
 1231 et al. (2020), the stable layer evolution was found by calculating oxygen diffusion in
 1232 the top 400 km of the core subject to equation (3) at r_c (with no barodiffusion) and
 1233 a Neumann condition at r_s given by , i.e. $\partial w_O/\partial r = -(\alpha_T/\alpha_O^c)\partial T/\partial r$ (Buffett and
 1234 Seagle, 2010). Here we use the same approach but additionally calculate the change
 1235 in layer size over time following Buffett and Seagle (2010). Treating the stable layer
 1236 in this way makes little difference to the overall layer thickness but allows us to
 1237 self-consistently partition energy and entropy between convecting and stable regions
 1238 using the methodology in Greenwood et al. (2021) (note thermal stratification is not
 1239 considered). Strictly the method of Buffett and Seagle (2010) is valid only when
 1240 $Q^c > Q_a^c$ as described above; however, in practice the layer evolution is set by the
 1241 inward FeO flux, which dominates the downward entrainment at the base of the
 1242 layer, and so the lower boundary condition (and hence the details of the double
 1243 diffusive instability) have little effect. The upper boundary condition on Q^c is given
 1244 by equation (2) with R given in Table 2 and the FeO flux calculated by the boundary
 1245 layer model of Davies et al. (2020).

1246 We first consider 2 example solutions that are identical except that one includes
 1247 FeO transfer to the core while the other does not. We use the default BMO param-
 1248 eters in Labrosse et al. (2007) (as did Davies et al. (2020)) a partition coefficient of
 1249 $P = K_d^{\text{FeO}}/c_{Fe}^c = 10$ for the FeO dissolution reaction (Pozzo et al., 2019), a mantle
 1250 FeO molar fraction of $c_{\text{FeO}}^m = 0.05$, core oxygen molar fraction of $c_O^c = 0.05$ and
 1251 $k = 100 \text{ W m}^{-1} \text{ K}^{-1}$. These 2 solutions correspond to Figure 2 of Davies et al.
 1252 (2020), where the case without FeO transfer is equivalent to the results of Labrosse
 1253 et al. (2007). Our results differ from these mentioned studies only by the modifica-
 1254 tions to the core model, which does not affect the BMO evolution in this formulation.
 1255 Core properties not already specified are taken from Davies et al. (2015) assuming

1256 an inner core density jump of 800 kg m^{-3} .

1257 Figure 16 shows the energy and entropy sources from the 2 example solutions.
1258 The energy balance follows the behaviour described in Labrosse et al. (2007). The
1259 key observation is that radioactivity and release of latent heat in the BMO stifle the
1260 early CMB flow, which is reduced even further by the negative heat of reaction Q_h
1261 at the CMB [equation (2)]. In both examples, E_J is negative for the entire duration,
1262 indicating an absence of dynamo action. FeO transfer into the core initially produces
1263 an $E_\alpha > 1000 \text{ MW K}^{-1}$, which quickly falls to between $250\text{-}500 \text{ MW K}^{-1}$, comparable
1264 to the entropy from thermal conduction E_k even in this high k scenario. Since $E_k \propto k$
1265 the thermal conductivity would need to be more than halved throughout the core in
1266 order to promote dynamo action in the case without FeO transfer. In the case with
1267 FeO transfer the geodynamo cannot operate for any k since E_α is sufficiently larger
1268 than E_s at all times. Finally, in this example the lifetime of the BMO is reduced
1269 from ~ 4.5 Gyrs to less than 2 Gyrs with FeO loss, which causes the growth of a
1270 ~ 100 km-thick chemically stable layer atop of the core.

1271 We have found that none of the models in the ranges $P = 1 - 10$, $c_{\text{FeO}}^m = 0.1 - 0.2$
1272 and $c_{\text{O}}^c = 0.05 - 0.13$ considered by Davies et al. (2020) produce a positive E_J during
1273 the lifetime of the BMO. We therefore made three plausible modifications to the
1274 Labrosse et al. (2007) model setup. First, we solve for the evolution of the solid
1275 mantle using the methodology of Driscoll and Bercovici (2014). Doing so allows
1276 us to produce a self-consistent heat flow out the top of the BMO and continue the
1277 calculation through to the present day once the BMO fully crystallises. The only
1278 modification to the solid mantle evolution from Driscoll and Bercovici (2014) is that
1279 the lower boundary is the time-dependent interface with the BMO, $r_{\text{bmo}}(t)$. The
1280 heat flow into the solid mantle is defined using the difference in temperature between
1281 the BMO and the solid mantle and when the BMO fully freezes, the procedure is

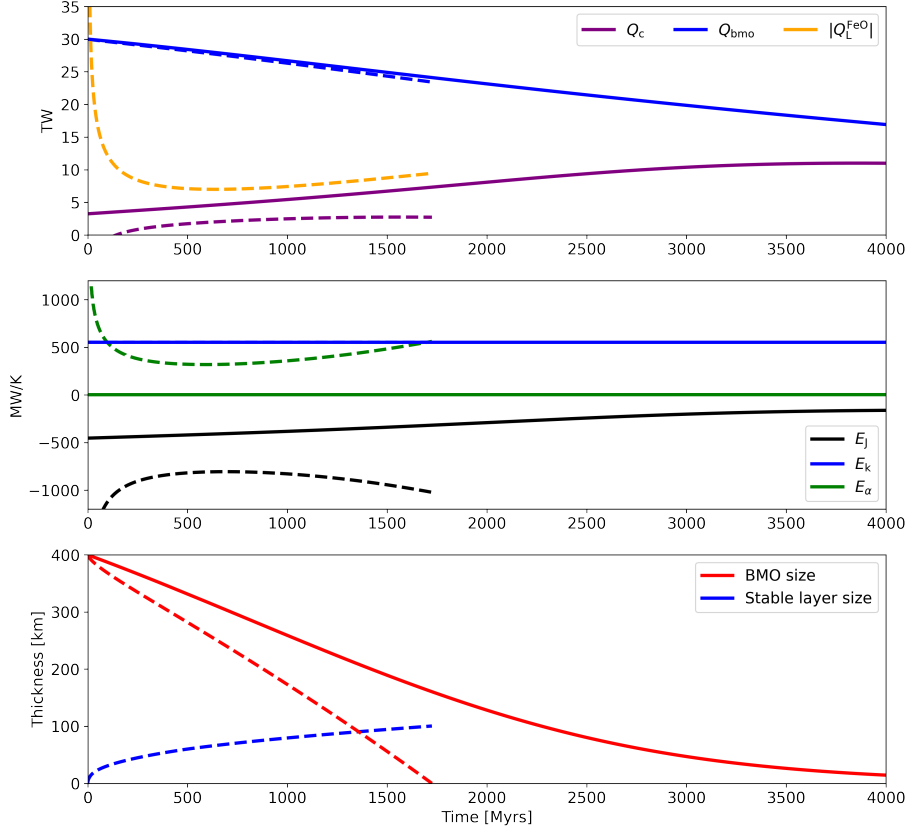


Figure 16: Examples of BMO evolution without (solid lines) and with (dashed lines) FeO transfer to the core, equivalent to those shown in Figure 2 of Davies et al. (2020). A partition coefficient of $P = 10$, a mantle FeO molar fraction of 0.05 and oxygen molar fraction of 0.05 in the core are used (see Davies et al. (2020) for a full set of parameters used for the BMO calculation). Top panel shows the energy sources within the BMO, middle panel shows the entropy sources within the core, and bottom panel shows the evolution of BMO and core stable layer thickness.

1282 identical to that laid out in Driscoll and Bercovici (2014) for Earth. This modification
1283 produces a heat flow at r_{bmo} that is initially larger than that of Labrosse et al. (2007),
1284 but decreases more rapidly with time, which is more conducive for dynamo action.

1285 Second, we raised the CMB temperature to 5500 K, the melting temperature of
1286 Bridgmanite at CMB pressure, which is the liquidus phase in the deep mantle (see
1287 review in Andrault et al., 2017). The presence of impurities would depress the melting
1288 point, perhaps by several hundred Kelvin, though this is still potentially within
1289 the significant uncertainties on the Bridgmanite melting point at these conditions
1290 (Stixrude et al., 2009). Higher initial temperatures allows sufficient cooling of the
1291 core to enable a dynamo since ~ 4 whilst retaining the correct ICB radius. Finally,
1292 we increased the initial thickness of the BMO from 400 km (Labrosse et al., 2007) to
1293 600 km, which increases the BMO lifetime, insulating the core from excessive heat
1294 loss to the solid mantle, particularly in the first 1 Gyrs. The initial thickness of the
1295 BMO is poorly constrained; however, values up to $\mathcal{O}(1000)$ km have been suggested
1296 (Stixrude et al., 2009; Blanc et al., 2020).

1297 Figure 17 shows a suite of calculations with $P = 1 - 5$ and $c_{\text{FeO}}^m = 0.1 - 0.2$, similar
1298 to the ranges considered by Davies et al. (2020). Higher P produces a larger FeO flux
1299 into the core, a larger E_α , and hence lower E_J . E_J is initially negative in all models,
1300 but becomes positive around 4 Ga before declining towards inner core nucleation
1301 (ICN) and subsequently rising during inner core growth. Figure 17a shows that only
1302 models towards the lower range of P or c_{FeO}^m produce a positive E_J just prior to ICN.
1303 Figure 17b shows that at 4 Ga, approximately the earliest time where the presence
1304 of the geodynamo is constrained (Tarduno et al., 2015), only solutions with $P = 1$
1305 and $c_{\text{FeO}}^m < 0.2$ give $E_J > 0$. The decrease of E_J with P is more significant at 4 Ga
1306 since oxygen is actively being transferred to the core, producing steeper chemical
1307 gradients that have not yet been smoothed out by diffusion. By ICN, the BMO has

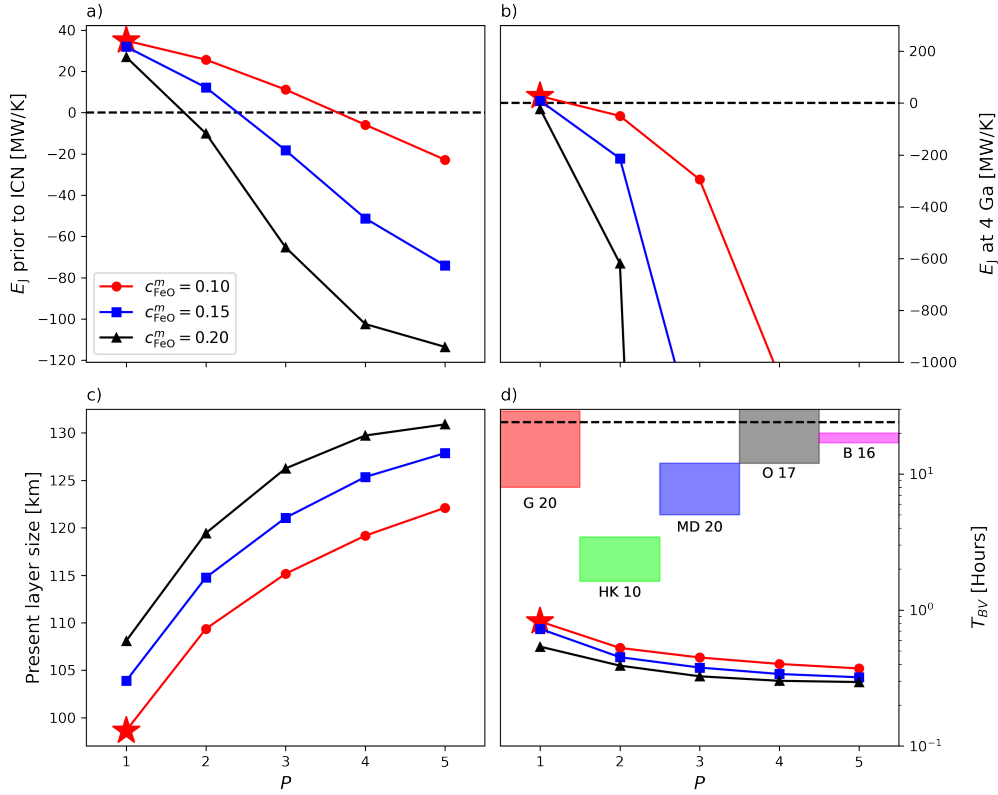


Figure 17: Results from the suite of models calculating the coupled evolution of the isentropic core, chemical stable layer, BMO, and solid mantle. All data are plotted with $P = 1 - 5$ on the horizontal axis, with varying mantle FeO concentrations shown by the colours that are consistent across each panel. Panels show values for E_J immediately prior to ICN (a) and at 4 Ga respectively (b), present-day chemical layer thickness at the top of the core (c), and the minimum Brunt-Väisälä period (peak N), T_{BV} , for the present day layer (d) [equation (30)]. Also in panel (d) are T_{BV} values from other studies (offset such that they do not overlap; they have no relation to the x -axis): G 20 (Greenwood et al., 2021) (also equivalent to our results in section 4.3), HK 10 (Helfrich and Kaneshima, 2010), MD 20 (Mound and Davies, 2020), O 17 (Olson et al., 2017), and B 16 (Buffett et al., 2016). The dashed lines in (a) and (b) show $E_J = 0$ and in (d) they show $T_{\text{BV}} = 24$ hrs. Note the log scale in (d). Stars indicate the model which produces positive E_J for the last 4 Gyrs, which is discussed further in Section 6.

1308 long since solidified, leading to a significant reduction in E_α .

1309 Figure 17c plots the present day stable layer thickness, where as expected thicker
1310 layers are attained for larger P or c_{FeO}^m . However, the impact of varying input param-
1311 eters causes thickness variations of only ~ 30 km because the layer growth is limited
1312 by the small molecular diffusivity. Finally, Figure 17d shows the shortest T_{BV} within
1313 the layer at the present day. All models exhibit periods under 1 hour, indicating a
1314 very strong density stratification. There is a rapid increase in the periods as P is
1315 lowered and so achieving periods within the 1.45 – 3.5 hours inferred from seismology
1316 (Helfrich and Kaneshima, 2010) would require a value of P of 1 or less. Other stud-
1317 ies quoted on Figure 17d (Greenwood et al., 2021; Mound and Davies, 2020; Olson
1318 et al., 2017; Buffett et al., 2016) all favour much longer periods consistent instead
1319 with our previous results on thermal stratification.

1320 In summary, the chemical stratification mechanisms that appear the most likely
1321 candidates to explain a thick and strongly stratified layer at the top of Earth’s core
1322 are incomplete mixing during core formation (Landeau et al., 2016) and FeO exchange
1323 with the mantle (Buffett and Seagle, 2010; Brodholt and Badro, 2017). Whether a
1324 primordial layer can survive mixing due to late-stage impacts is a key issue that will
1325 benefit from improved models of core formation. We find that models of FeO transfer
1326 between a BMO and the core require relatively weak partitioning ($P \sim 1$) in order
1327 to enable dynamo action in the early core that continues to the present day while
1328 also producing present-day stable layers of similar strength to inferences from seismic
1329 models. These calculations are limited because they only include FeO partitioning
1330 with a constant value of P . Future work will need to couple the reactions of SiO_2 and
1331 MgO ; however, as with the precipitation case it seems premature to move down this
1332 path owing to the significant uncertainties in the equilibrium calculations explained
1333 in Section 3. The multi-element calculations in Section 3.4 suggest that the core is

1334 strongly under-saturated in O, while P does not vary significantly when the BMO
1335 lifetime is short (and hence there is little variation in T). Therefore the calculations
1336 presented in this section hopefully represent a reasonable starting point for further
1337 investigations into coupled chemical core-mantle evolution.

1338 It is notable that thermal stratification produces layers that match the thickness
1339 but not the stability inferred from seismology, instead predicting T_{BV} values more
1340 in line with inferences from geomagnetism. Conversely, FeO transfer produces lay-
1341 ers that approximate the stability but not the thickness of the seismic observations,
1342 instead predicting layer thicknesses comparable to inferences from DNS and geomag-
1343 netism. One potential resolution is that the top of Earth’s core comprises a strongly
1344 chemically stratified region embedded within and thicker and more weakly stratified
1345 layer. This scenario would require high T_{BV} values confined close to the CMB, with
1346 geomagnetic observations sampling an average stratification signal in the upper core.

1347 5. Chemical Precipitation

1348 In this section we discuss the effect of precipitation on the thermal and magnetic
1349 evolution of the core. The efficiency of precipitation in powering the geodynamo de-
1350 pends crucially on the precipitation rate dw_i^c/dT of oxide i . Simple models assuming
1351 high conductivity and constant precipitation rates have shown that precipitation of
1352 MgO with $dw_{\text{MgO}}^c/dT = 5 \times 10^{-5} \text{ K}^{-1}$ (O’Rourke and Stevenson, 2016) or precipita-
1353 tion of SiO₂ with $dw_{\text{SiO}_2}^c/dT = 4 \times 10^{-5} \text{ K}^{-1}$ (Hirose et al., 2017) can maintain the
1354 geomagnetic field over the past 4 Gyrs with similar cooling rates and heat flows to
1355 those inferred from conventional low conductivity calculations. On the other hand,
1356 Du et al. (2019) found that high heat flows and cooling rates were still required to
1357 drive the dynamo using precipitation rates of $dw_{\text{MgO}}^c/dT = 6 \times 10^{-6} \text{ K}^{-1}$ obtained
1358 from their experiments. Additional power provided by precipitation reduces the core

1359 cooling rate required to meet a given entropy production and hence predicts an older
1360 inner core age; however thermal history models with precipitation still predict super-
1361 solidus temperatures for the first $\sim 1 - 3$ Gyr after core formation (O’Rourke et al.,
1362 2017; Mittal et al., 2020) and so suggest the existence of a BMO at least in early
1363 times.

1364 O’Rourke et al. (2017) conducted a large number of coupled core-mantle evolu-
1365 tion models using a standard core setup (Labrosse et al., 2015) with the addition of
1366 precipitation (described in O’Rourke and Stevenson, 2016). Their mantle evolution
1367 model is from Korenaga (2006), which produces a much flatter CMB heat flow evolu-
1368 tion compared to conventional mantle evolution models based on standard boundary
1369 layer theory (e.g. Driscoll and Bercovici, 2014; Jaupart et al., 2015, and Figure 13).
1370 O’Rourke et al. (2017) focused on the case where $k \approx 90 \text{ W m}^{-1} \text{ K}^{-1}$ at the CMB
1371 and varied dw_{MgO}^c/dT between 0 and $8 \times 10^{-5} \text{ K}^{-1}$. For their nominal setup they
1372 found a preferred value of $dw_{MgO}^c/dT \sim 2 \times 10^{-5}$ to ensure E_J is sufficiently large to
1373 maintain dynamo action since core formation.

1374 Mittal et al. (2020) modelled the simultaneous precipitation of Mg, Si and O. They
1375 coupled the evolution of the core and solid mantle to an intermediate ‘interaction
1376 layer’ comprising precipitated material (MgO, FeO and SiO₂) together with MgSiO₃
1377 and FeSiO₃. In this model the interaction layer evolution is governed by a balance
1378 between growth due to precipitation and erosion by mantle flow. Mittal et al. (2020)
1379 found that a wide range of evolutionary scenarios are possible with different oxides
1380 precipitating at different times depending on the properties of the interaction layer
1381 (its thickness and erosion rate), the initial compositions and the parameters defining
1382 the equilibrium constants. This behaviour is consistent with the simple mass balance
1383 calculations presented in Section 3.

1384 The large number of poorly constrained parameters mean that it is difficult to

1385 make general statements regarding the thermal and magnetic evolution of the core
 1386 when precipitation is included. We therefore consider simple scenarios whereby MgO
 1387 precipitation begins at core formation and proceeds at a constant rate in the range
 1388 $0.3 - 1.5 \text{ K}^{-1}$ as shown in Figure 12. For simplicity we neglect the effects of SiO₂
 1389 and FeO and seek the minimum CMB heat flow that will enable dynamo action for
 1390 the past 3.5 Gyrs. To do this we follow Nimmo (2015a) and Davies et al. (2015)
 1391 and prescribe $E_J = 0$ before inner core formation and specify Q^c during inner core
 1392 growth, which produces conservative estimates of the cooling rate, core temperature
 1393 and inner core age and avoids the nonphysical behaviour that arises when E_J is fixed
 1394 for all time (Nimmo, 2015a; Labrosse et al., 2015).

1395 Figure 18 shows the predicted inner core age and the CMB temperature and
 1396 CMB heat flow at 3.5 Ga, corresponding to the age of the paleointensity determi-
 1397 nations of Tarduno et al. (2010). The shaded temperature range of $4150 \pm 150 \text{ K}$
 1398 corresponds to present estimates of the lower mantle solidus temperature (Fiquet
 1399 et al., 2010; Andrault et al., 2011); core temperatures exceeding this range sug-
 1400 gest partial melting in the past. Calculations are performed for the three values of
 1401 $\Delta\rho = 600, 800$ and 1000 kg m^{-3} using parameters in Table 2 and core conductivity
 1402 values of $k = 70 \text{ W m}^{-1} \text{ K}^{-1}$ and $k = 100 \text{ W m}^{-1} \text{ K}^{-1}$ (see Section 2.3). Also shown
 1403 are favoured models from Labrosse et al. (2015), Driscoll and Bercovici (2014), Nak-
 1404 agawa and Tackley (2014) and Nimmo (2015a), who also consider high k but use
 1405 different model setups and constraints on CMB heat flow.

1406 Figure 18 shows that lower k values imply an older inner core and require lower
 1407 CMB heat flow and core cooling rates to maintain the dynamo. Increasing $\Delta\rho$ from
 1408 600 kg m^{-3} to 1000 kg m^{-3} can produce a 600–800 K decrease in the early core
 1409 temperature and a 200–400 Myr increase in the inner core age, depending on the
 1410 details on the model. With $dw_{Mg}^c/dt \leq 0.3 \times 10^{-5} \text{ K}^{-1}$ we find an inner core age of

1411 at most 300 – 600 Gyrs (400 – 800 Gyrs) and minimum CMB heat flows at 3.5 Ga in
1412 the range 14 – 22 TW (10 – 15 TW) for $k = 100 \text{ W m}^{-1} \text{ K}^{-1}$ ($k = 70 \text{ W m}^{-1} \text{ K}^{-1}$).
1413 With a precipitation rate of $1.5 \times 10^{-5} \text{ K}^{-1}$ the maximum inner core age rises to
1414 800 – 1100 Gyrs (1100 – 1500 Gyrs) and required CMB heat flows at 3.5 Ga decrease
1415 to 8 – 9 TW ($\sim 6 \text{ TW}$) for $k = 100 \text{ W m}^{-1} \text{ K}^{-1}$ ($k = 70 \text{ W m}^{-1} \text{ K}^{-1}$). The vast
1416 majority of models predict an inner core age of at most 700 million years and early
1417 core temperatures exceeding the lower mantle solidus.

1418 Davies et al. (2015) considered how uncertainties in a number of input param-
1419 eters could affect predictions of inner core age and early core temperature. Within
1420 plausible ranges they varied the thermal expansivity, latent heat coefficient, spe-
1421 cific heat capacity and core melting curve and found that the combined variations
1422 produced uncertainties on the inner core age of $\pm 150 \text{ Myr}$ and the early tempera-
1423 ture of $\pm 400 \text{ K}$. These uncertainties are comparable to the uncertainty in $\Delta\rho$ alone.
1424 When combined with the fact that the temperatures and inner core ages in Figure 18
1425 are lower bounds this suggests that while MgO precipitation undoubtedly helps to
1426 relax the power requirements for the dynamo, some key implications of high core
1427 conductivity such as the existence of an early BMO remain even in the presence of
1428 precipitation. The inner core is also certainly much younger than the core, though
1429 its age is evidently rather uncertain. In particular these models cannot differentiate
1430 between paleomagnetic inferences of inner core nucleation at $\sim 0.5 \text{ Ga}$ (Bono et al.,
1431 2019) and $\sim 1.3 \text{ Ga}$ (Biggin et al., 2015).

1432 6. Towards Resolving the New Core Paradox

1433 Over the last few years various proposals have been put forth to resolve the new
1434 core paradox. Driscoll and Bercovici (2014) argued for 2 TW of heat produced by
1435 ^{40}K , which slows the core cooling rate for a given mantle heat flow and hence helps

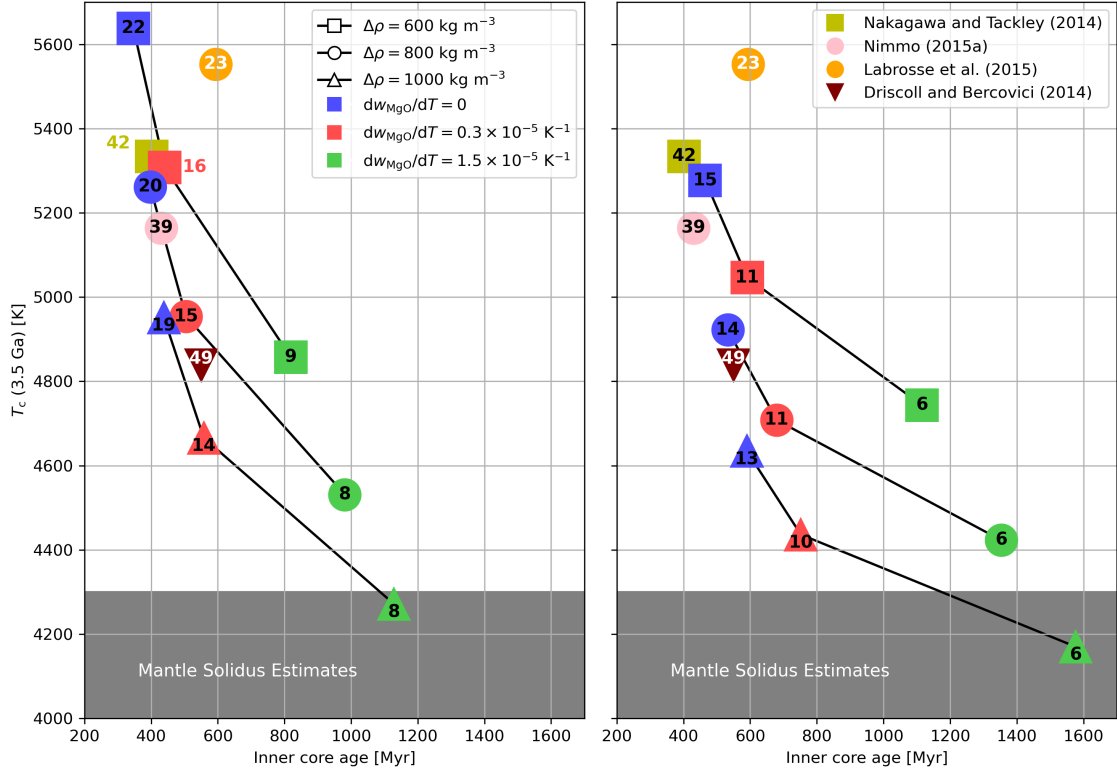


Figure 18: Effect on the inner core age and early CMB temperatures of MgO precipitation. Left panel shows our results using a CMB conductivity of $k = 100 \text{ W m}^{-1} \text{ K}^{-1}$ and the right panel shows our results using $k = 70 \text{ W m}^{-1} \text{ K}^{-1}$. Symbols denote different core properties based on density jumps at the ICB of 600 (squares), 800 (circles), 1000 kg m^{-3} (triangles). Colours indicate no MgO precipitation (blue), and at a fixed rate of $0.3 \times 10^{-5} \text{ K}^{-1}$ (red) and $1.5 \times 10^{-5} \text{ K}^{-1}$ (green) as derived from Figure 12. Solid lines link models with the same core properties but varying rates of MgO precipitation. Numbers show the CMB heat flow in TW at 3.5 Ga. Results from other studies using a high thermal conductivity are also shown, replicated on both panels for comparison to each of our datasets. Based on Figure 3 in Davies et al. (2015).

1436 to enable positive E_J before inner core formation. The drawback here is that ex-
1437 periments and simulations suggest that little ^{40}K partitioned into the core during
1438 formation (Chidester et al., 2017; Xiong et al., 2018). Precipitation provides another
1439 potential solution, though as we have seen it introduces a number of uncertain pa-
1440 rameters and is difficult to constrain from available observations (though see Helffrich
1441 et al., 2018). Laneuville et al. (2018) suggested a compositionally stratified BMO,
1442 which helps to retain heat in the core; however, their model still suggests that the
1443 dynamo shuts off prior to inner core formation.

1444 Here we present another possible resolution to the new core paradox that does
1445 not rely on precipitation or radiogenic heating. The approach is to retain the mini-
1446 mum number of physical processes (and hence poorly constrained parameters) while
1447 maintaining consistency with the basic predictions of core evolution with high con-
1448 ductivity. The early evolution involves coupled thermo-chemical interactions between
1449 the core and BMO, as expected from the high temperatures that arise in the high k
1450 scenario (Section 5). We allow exchange of FeO with the core, which actually lowers
1451 the available entropy (Section 4.4), but is suggested by a large range of core-mantle
1452 equilibrium calculations (Section 3.3). Consequently, a chemically stratified layer
1453 grows from the start of our model. FeO enrichment may enhance or be suppressed
1454 by a stratified layer was emplaced at core formation (Landeau et al., 2016), though
1455 we have not included this latter effect. Indeed, since erosion of chemical layers is
1456 expected to be weak (Bouffard et al., 2020) and layer growth is governed by diffu-
1457 sion we may anticipate similar long-term behaviour in the two cases. After complete
1458 freezing of the BMO the solid mantle follows the classical boundary-layer evolution
1459 described in the model of Driscoll and Bercovici (2014), with no further mass flux
1460 between core and mantle (Section 4.4). A “successful” model is required to produce
1461 positive E_J for all time and match the present-day ICB radius.

1462 Figure 19 shows the results of one calculation that matches the constraints using
1463 $k = 70 \text{ W m}^{-1} \text{ K}^{-1}$ and $\Delta\rho = 800 \text{ kg m}^{-3}$, corresponding to the model denoted by
1464 a star in Figure 17. The BMO is initialised at 600 km thick and persists for 2 Gyrs
1465 producing a large flux of FeO into the core. The enhanced heat flux out of the BMO
1466 arising from our revisions to the original Labrosse et al. (2007) model (Section 4.4)
1467 enable the onset of dynamo action around 4 Ga with high k . Once the BMO freezes,
1468 the chemical layer continues to thicken by diffusion before the initiation and growth
1469 of the inner core around 0.8 Ga begins to erode it back towards the CMB. Prior
1470 to inner core formation E_J remains just above zero and hence the model predicts
1471 continuous dynamo action for the last 4 billion years. The present day heat flow and
1472 potential temperature at the top of the convecting mantle are respectively 35 TW
1473 and 1653 K, within current constraints of 35 – 41 TW and $\sim 1550 - 1750$ K (Jaupart
1474 et al., 2015), while the current inner core size is 1221 km as in Earth.

1475 The results in Figures 19 are sensitive to the parameter choices as is evident by
1476 the fact that E_J remains just positive prior to inner core nucleation. In particular,
1477 increasing k above $k = 70 \text{ W m}^{-1} \text{ K}^{-1}$, which is on the lower end of the estimates
1478 presented in Section 2.3, causes E_J to fall below zero. We have not conducted
1479 an exhaustive search of the solution space, but did not obtain viable solutions in
1480 the absence of a BMO, using the original BMO setup of Labrosse et al. (2007), or
1481 with strong FeO partitioning ($P > 1$). However, while the solution might appear
1482 somewhat specialised, there are a large number of parameter combinations that have
1483 yet to be tested. Moreover, a large range of successful solutions are clearly available
1484 with only a modest additional amount of entropy due to precipitation or radiogenic
1485 heating that are within current observational or modelling uncertainties. Assuming
1486 precipitation of Mg and/or Si begins at a CMB temperature of 5000 K (Figure 12),
1487 the corresponding onset time for the solution in Figure 19 is 2.8 Ga. Prior to this

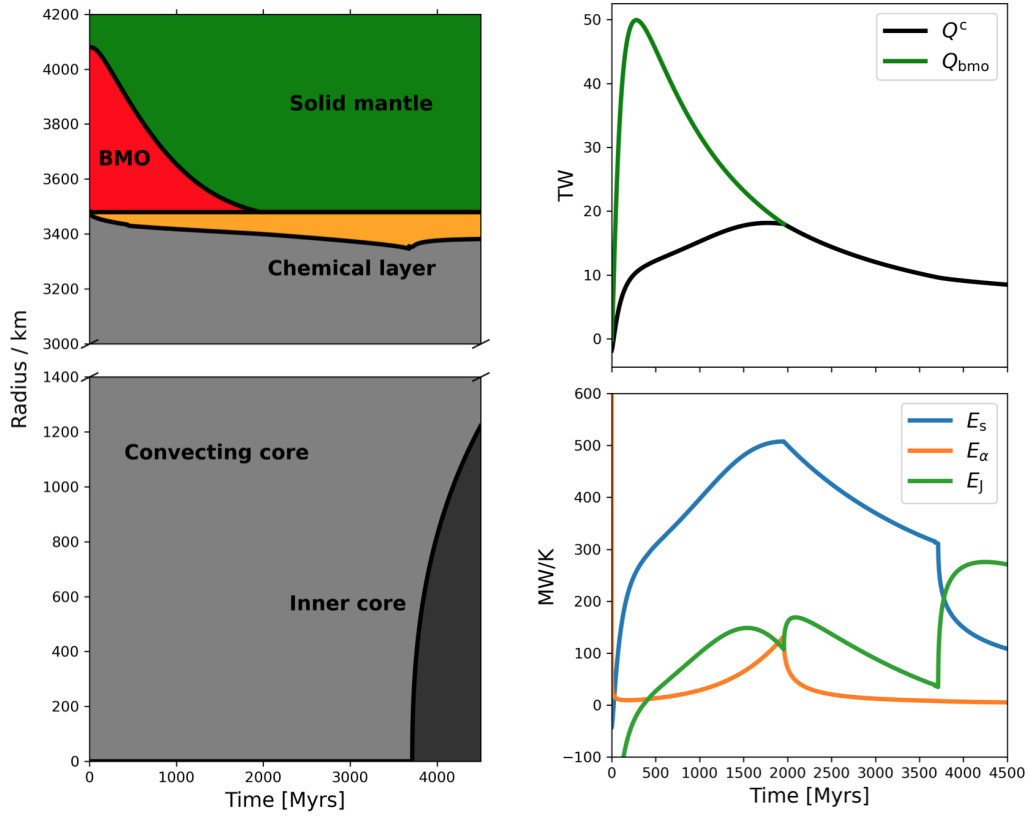


Figure 19: Results from our best model, indicated by the stars on Figure 17. On the left shows a radial cross section through time of the coupled Earth evolution. The inner core and convecting outer core are represented by the dark and light grey respectively. The chemically stratified layer is in orange, whilst the BMO and solid mantle are shown in red and green. Note the break in the y-axis and that both halves of the figure are to scale with each other. The right panels show energy (top) and entropy (bottom) sources from the calculation.

1488 the dynamo would remain reliant on rapid cooling.

1489 The solution in Figure 19 provides a number of predictions that can be tested with
1490 past and present observations. First, the Ohmic dissipation displays local minima
1491 just prior to inner core formation and completion of BMO freezing and a global min-
1492 imum around 4 Ga. Since the magnetic field strength is thought to be proportional
1493 to E_J (Aubert et al., 2009) these minima might be observable in paleointensity data,
1494 though care is needed when translating E_J to an equivalent virtual dipole moment
1495 (Driscoll, 2016; Landeau et al., 2017; Driscoll and Wilson, 2018). The inner core age
1496 is 800 Myrs, which sits between the paleointensity changes inferred at ~ 0.5 Ga by
1497 Bono et al. (2019) and ~ 1.3 Ga by Biggin et al. (2015), while the delayed onset of
1498 dynamo action appears (perhaps coincidentally) close to the still debated Hadean
1499 paleointensity data of Tarduno et al. (2015). Nevertheless, the results will hope-
1500 fully motivate future attempts to link paleointensity variations to abrupt changes in
1501 core evolution. Second, the present-day strength of stratification is strong enough
1502 to match the estimates derived from seismic observations (Helffrich and Kaneshima,
1503 2010), but larger than inferences from MAC wave studies and geodynamo simula-
1504 tions. The stable layer thickness is 100 km, which is thinner than some seismic studies
1505 (Section 4.1) but more in line with inferences from geomagnetism and geodynamo
1506 simulations (Section 4.2). Finally, the present-day CMB heat flow is 8.5 TW, which
1507 is within the range of 7 – 17 TW estimated by Nimmo (2015a) and the 5 – 15 TW
1508 suggested by Lay et al. (2009). The core is actually mildly sub-adiabatic at present
1509 ($Q_a^c = 9.4$ TW), though we did not include this effect in the model. A potential
1510 resolution to the contrasting observational constraints on chemical vs thermal layers
1511 may be that a strongly stratified chemical sub-layer exists within a broader weakly
1512 stratified thermal layer.

1513 It is worth noting that our preferred evolution scenario requires significant core

1514 cooling, with the CMB temperature falling from 5500 K to 4360 K over 4.5 Gyrs.
1515 Other scenarios have been proposed where the CMB temperature drop is much less
1516 dramatic, ~ 300 K (Andrault et al., 2016). With high core conductivity we find rapid
1517 cooling is ubiquitous in our models and have not found a way to match the available
1518 constraints on core and mantle evolution with such slow cooling rates.

1519 Many avenues for future work remain, as have been mentioned throughout this re-
1520 view. Systematic studies of core thermal conductivity approaching CMB conditions
1521 are needed to provide robust methods for extrapolating from lower $P - T$ conditions,
1522 while the effects of composition and the discordant results from direct experimental
1523 and computational determinations of k needs to be resolved. Improved constraints on
1524 the temperature- and composition-dependence of partitioning at CMB conditions as
1525 well as further systematic comparisons of candidate thermodynamic models (Badro
1526 et al., 2018) will help reduce the range of viable precipitation rates and onset times
1527 (Figure 12). Future seismic and geomagnetic observations together with high res-
1528 olution DNS conducted in dynamical regions approaching Earth’s core conditions
1529 (Aubert et al., 2017; Wicht and Sanchez, 2019) can help to constrain the existence,
1530 thickness, and global vs local nature of stable regions below the CMB. Finally, it is
1531 crucial to continue to seek observational evidence for the existence of a basal magma
1532 ocean, for example through its potential links to LLVPs and ultra-low velocity zones
1533 (Labrosse et al., 2015), and also for precipitation, perhaps in the form of a thin layer
1534 at the CMB or the incorporation of precipitation products into the mantle (Helffrich
1535 et al., 2018).

1536 Improved constraints on the ICB density jump $\Delta\rho$ are also clearly needed. Wong
1537 et al. (2021) have made a potentially promising step in this direct by combining a
1538 theoretical model of a slurry region above the ICB (the so-called F-layer Souriau and
1539 Calvet, 2015) with seismic observations of 1D compressional wave-speed variations.

1540 From a large suite of models that span uncertainties in the main input parameters,
1541 Wong et al. (2021) constrain $\Delta\rho \approx 530 \text{ kg m}^{-3}$, on the lower end of the range of
1542 values obtained from normal modes (Masters and Gubbins, 2003). This model also
1543 yields an independent constraint on the CMB heat flow that is consistent with our
1544 preferred model.

1545 Finally, we note that the structure, dynamics and evolution of layers within the
1546 core depends crucially on the role of myriad instabilities that can lead to partial or
1547 complete mixing. Parameterisations of these processes in thermal history models
1548 are rather crude (Greenwood et al., 2021), but rely heavily on results from DNS. In
1549 particular, future DNS studies will hopefully shed light on the role of double-diffusive
1550 instabilities and penetrative convection in the formation and survival of layering in
1551 the rapidly rotating, turbulent and magnetic environment that characterises the core.

1552 7. Conclusions

1553 We have reviewed the high thermal conductivity scenario for core evolution, which
1554 predicts a young inner core and early temperatures consistent with the existence of
1555 a basal magma ocean (Table 1). The main conclusions are:

- 1556 • Consistent extrapolation of thermal and electrical conductivity estimates from
1557 a number of recent studies suggests $k = 70\text{--}110 \text{ W m}^{-1} \text{ K}^{-1}$ at CMB conditions
1558 of 4000 K, 135 GPa and ~ 10 mole percent light element;
- 1559 • Both the onset time and rate of MgO and SiO₂ precipitation are uncertain and
1560 depend on a number of factors including temperature, compositions on both
1561 sides of the CMB, and the nature of the reactions that govern the equilibrium;
- 1562 • MgO precipitation may begin anywhere between 3000 – 6000 K with rates
1563 between $0.3 - 1.5 \times 10^{-5} \text{ K}^{-1}$. The majority of our calculations suggest a

- 1564 narrower range of onset between 4000 – 5000 K with rates between $1.0 - 1.5 \times$
 1565 10^{-5} K^{-1} ;
- 1566 • SiO_2 precipitation may begin anywhere between 3000 – 6000 K with rates
 1567 between $0.1 - 8 \times 10^{-5} \text{ K}^{-1}$. The majority of our calculations suggest a narrower
 1568 range of onset between 3000 – 4500 K with rates between $2 - 8 \times 10^{-5} \text{ K}^{-1}$;
 - 1569 • The core is always undersaturated in O in our calculations, which causes FeO
 1570 dissolution at all times;
 - 1571 • Our results suggest light elements dissolved into the core after its formation,
 1572 forming a stably stratified chemical layer below the CMB. Precipitation was
 1573 delayed, but once initiated would supply ample power for sustaining the geo-
 1574 dynamo;
 - 1575 • Viable core evolution scenarios predict thermally stable layers at most 400 –
 1576 700 km thick. The strength of stratification can match some inferences from
 1577 geomagnetism but not values derived from seismic observations;
 - 1578 • The minimum requirements for maintaining the dynamo over the last 3.5 Gyrs
 1579 suggest an inner core age of at most 300 – 600 Gyrs (400 – 800 Gyrs) for
 1580 $k = 100 \text{ W m}^{-1} \text{ K}^{-1}$ ($k = 70 \text{ W m}^{-1} \text{ K}^{-1}$) and an MgO precipitation rate
 1581 $\leq 0.3 \times 10^{-5} \text{ K}^{-1}$. With a precipitation rate of $1.5 \times 10^{-5} \text{ K}^{-1}$ the maximum
 1582 inner core age is 800 – 1100 Gyrs (1100 – 1500 Gyrs) for $k = 100 \text{ W m}^{-1} \text{ K}^{-1}$
 1583 ($k = 70 \text{ W m}^{-1} \text{ K}^{-1}$). The temperature of the early core almost always ex-
 1584 ceeds present estimates of the mantle solidus, suggesting a BMO event with
 1585 precipitation.
 - 1586 • We present a solution that overcomes the new core paradox by enabling con-

1587 tinuous dynamo generation from 4 Ga to present. This model uses $k =$
1588 $70 \text{ W m}^{-1} \text{ K}^{-1}$ and matches the present inner core size and heat flow and
1589 temperature at the top of the convecting mantle. It predicts a present-day
1590 CMB heat flow of 8.5 TW, chemically stable layer of 100 km produced by FeO
1591 exchange with the mantle, and a BMO lifetime of 2 Gyrs.

1592 **Acknowledgements**

1593 SG is supported by NSF-NERC grant NE/T003855/1. CD acknowledges support
1594 via NERC grant NE/T000228/1. The authors are indebted to Prof. James Badro
1595 for detailed discussions and assistance benchmarking code used to calculate CMB
1596 equilibria. We are also grateful to Dr. Jon Mound, Dr. Alfred Wilson and Prof.
1597 Dario Alfè for commenting on various aspects of the article.

1598 **References**

- 1599 Adjaoud, O., Steinle-Neumann, G., Jahn, S., 2011. Transport properties of Mg_2SiO_4
1600 liquid at high pressure: Physical state of a magma ocean. *Earth Planet. Sci. Lett.*
1601 312 (3-4), 463–470.
- 1602 Alexandrakis, C., Eaton, D., 2010. Precise seismic-wave velocity atop Earth’s core:
1603 No evidence for outer-core stratification. *Phys. Earth Planet. Int.* 180, 59–65.
- 1604 Alfè, D., Gillan, M., Price, G., 2002a. Composition and temperature of the Earth’s
1605 core constrained by combining *ab initio* calculations and seismic data. *Earth*
1606 *Planet. Sci. Lett.* 195, 91–98.
- 1607 Alfè, D., Gillan, M., Price, G., 2002b. *Ab initio* chemical potentials of solid and liquid
1608 solutions and the chemistry of the Earth’s core. *J. Chem. Phys.* 116, 7127–7136.

1609 Alfè, D., Price, G., Gillan, M., 2002c. Iron under Earth's core conditions: Liquid-
1610 state thermodynamics and high-pressure melting curve from *ab initio* calculations.
1611 Phys. Rev. B 65, 165118.

1612 Amit, H., 2014. Can downwelling at the top of the Earth's core be detected in the
1613 geomagnetic secular variation? Phys. Earth Planet. Int. 229, 110–121.

1614 Ammann, M., Brodholt, J., Wookey, J., Dobson, D., 2010. First-principles con-
1615 straints on diffusion in lower-mantle minerals and a weak D". Nature 465, 462–465.

1616 Andrault, D., Bolfan-Casanova, N., Bouhifd, M. A., Boujibar, A., Garbarino, G.,
1617 Manthilake, G., Mezouar, M., Monteux, J., Parisiades, P., Pesce, G., 2017. Toward
1618 a coherent model for the melting behavior of the deep Earth's mantle. Phys. Earth
1619 Planet. Int. 265, 67–81.

1620 Andrault, D., Bolfan-Casanova, N., Lo Nigro, G., Bouhifd, M., Garbarinho, G.,
1621 Mezouar, M., 2011. Solidus and liquidus profiles of chondritic mantle: Implication
1622 for melting of the Earth across its history. Earth Planet. Sci. Lett. 304, 251–259.

1623 Andrault, D., Monteux, J., Le Bars, M., Samuel, H., 2016. The deep Earth may not
1624 be cooling down. Earth Planet. Sci. Lett. 443, 195–203.

1625 Anzellini, S., Dewaele, A., Mezouar, M., Loubeyre, P., Morard, G., 2013. Melting of
1626 iron at Earth's inner core boundary based on fast x-ray diffraction. Science 340,
1627 464–466.

1628 Arveson, S. M., Deng, J., Karki, B. B., Lee, K. K., 2019. Evidence for Fe-Si-O liquid
1629 immiscibility at deep Earth pressures. Proc. Natl. Acad. Sci. 116 (21), 10238–
1630 10243.

- 1631 Aubert, J., Amit, H., Hulot, G., 2007. Detecting thermal boundary control in surface
1632 flows from numerical dynamos. *Phys. Earth Planet. Int.* 160, 143–156.
- 1633 Aubert, J., Gastine, T., Fournier, A., 2017. Spherical convective dynamos in the
1634 rapidly rotating asymptotic regime. *J. Fluid Mech.* 813, 558–593.
- 1635 Aubert, J., Labrosse, S., Poitou, C., 2009. Modelling the palaeo-evolution of the
1636 geodynamo. *Geophys. J. Int.* 179, 1414–1428.
- 1637 Badro, J., Aubert, J., Hirose, K., Nomura, R., Blanchard, I., Borensztajn, S., Siebert,
1638 J., 2018. Magnesium partitioning between Earth’s mantle and core and its potential
1639 to drive an early exsolution geodynamo. *Geophys. Res. Lett.* 45, 13–24.
- 1640 Badro, J., Brodholt, J., Piet, H., Siebert, J., Ryerson, F., 2015. Core formation
1641 and core composition from coupled geochemical and geophysical constraints. *Proc.*
1642 *Natl. Acad. Sci.* 112, 12310–12314.
- 1643 Badro, J., Côté, A., Brodholt, J., 2014. A seismologically consistent compositional
1644 model of Earth’s core. *Proc. Natl. Acad. Sci.* 111, 7542–7545.
- 1645 Badro, J., Siebert, J., Nimmo, F., 2016. An early geodynamo driven by exsolution
1646 of mantle components from Earth’s core. *Nature* 536 (7616), 326.
- 1647 Biggin, A., Piispa, E., Pesonen, L., Holme, R., Paterson, G., Veikkolainen, T., Tauxe,
1648 L., 2015. Palaeomagnetic field intensity variations suggest Mesoproterozoic inner-
1649 core nucleation. *Nature* 526 (7572), 245.
- 1650 Blanc, N., Stegman, D., Ziegler, L., 2020. Thermal and magnetic evolution of a
1651 crystallizing basal magma ocean in Earth’s mantle. *Earth Planet. Sci. Lett.* 534,
1652 116085.

- 1653 Bloxham, J., Jackson, A., 1990. Lateral temperature variations at the core-mantle
1654 boundary deduced from the magnetic field. *Geophys. Res. Lett.* 17, 1997–2000.
- 1655 Bono, R. K., Tarduno, J. A., Nimmo, F., Cottrell, R. D., 2019. Young inner core
1656 inferred from Ediacaran ultra-low geomagnetic field intensity. *Nat. Geosci.* 12 (2),
1657 143–147.
- 1658 Bouffard, M., Choblet, G., Labrosse, S., Wicht, J., 2019. Chemical convection and
1659 stratification in the Earth’s outer core. *Frontiers in Earth Science* 7, 99.
- 1660 Bouffard, M., Landeau, M., Goument, A., 2020. Convective erosion of a primordial
1661 stratification atop Earth’s core. *Geophys. Res. Lett.* 47 (14), e2020GL087109.
- 1662 Bouhifd, M., Jephcoat, A., 2011. Convergence of Ni and Co metal-silicate partition
1663 coefficients in the deep magma-ocean and coupled silicon-oxygen solubility in iron
1664 melts at high pressures. *Earth Planet. Sci. Lett.* 307 (3), 341 – 348.
- 1665 Braginsky, S., 1999. Dynamics of the stably stratified ocean at the top of the core.
1666 *Phys. Earth Planet. Int.* 111, 21–34.
- 1667 Braginsky, S., Roberts, P., 1995. Equations governing convection in Earth’s core and
1668 the geodynamo. *Geophys. Astrophys. Fluid Dyn.* 79, 1–97.
- 1669 Brodholt, J., Badro, J., 2017. Composition of the low seismic velocity E’ layer at the
1670 top of Earth’s core. *Geophys. Res. Lett.* 44, 2017GL074261.
- 1671 Buffett, B., 2014. Geomagnetic fluctuations reveal stable stratification at the top of
1672 the Earth’s core. *Nature* 507, 484–487.
- 1673 Buffett, B., 2015. Core-mantle interactions. In: Schubert, G. (Ed.), *Treatise on Geo-*
1674 *physics, Vol. 8: Core Dynamics.* Elsevier, Amsterdam, pp. 213–224.

- 1675 Buffett, B., Huppert, H., Lister, J., Woods, A., 1996. On the thermal evolution of
1676 the Earth's core. *J. Geophys. Res.* 101, 7989–8006.
- 1677 Buffett, B., Knezek, N., Holme, R., 2016. Evidence for MAC waves at the top of
1678 Earth's core and implications for variations in length of day. *Geophys. J. Int.* 204,
1679 1789–2000.
- 1680 Buffett, B., Seagle, C., 2010. Stratification of the top of the core due to chemical
1681 interactions with the mantle. *J. Geophys. Res.* 115, B04407.
- 1682 Caracas, R., Hirose, K., Nomura, R., Ballmer, M. D., 2019. Melt–crystal density
1683 crossover in a deep magma ocean. *Earth Planet. Sci. Lett.* 516, 202–211.
- 1684 Chester, G., Thellung, A., 1961. The law of Wiedemann and Franz. *Proc. Phys. Soc.*
1685 London 77, 1005–1013.
- 1686 Chidester, B. A., Rahman, Z., Richter, K., Campbell, A. J., 2017. Metal-silicate
1687 partitioning of U: Implications for the heat budget of the core and evidence for
1688 reduced U in the mantle. *Geochimica et Cosmochimica Acta* 199, 1 – 12.
- 1689 Christensen, U., 2018. Geodynamo models with a stable layer and heterogeneous
1690 heat flow at the top of the core. *Geophys. J. Int.* 215 (2), 1338–1351.
- 1691 Christensen, U., Aubert, J., Hulot, G., 2010. Conditions for Earth-like geodynamo
1692 models. *Earth Planet. Sci. Lett.* 296, 487–496.
- 1693 Christensen, U. R., 2006. A deep dynamo generating Mercury's magnetic field. *Nature*
1694 444 (7122), 1056–1058.
- 1695 Constable, C., Korte, M., Panovska, S., 2016. Persistent high paleosecular variation

1696 activity in southern hemisphere for at least 10 000 years. *Earth Planet. Sci. Lett.*
1697 453, 78–86.

1698 Cox, G., Davies, C., Livermore, P., Singleton, J., 2019. Penetration of boundary-
1699 driven flows into a rotating spherical thermally-stratified fluid. *J. Fluid Mech.*
1700 864, 519–553.

1701 Davies, C., 2015. Cooling history of Earth’s core with high thermal conductivity.
1702 *Phys. Earth Planet. Int.* 247, 65–79.

1703 Davies, C., Gubbins, D., 2011. A buoyancy profile for the Earth’s core. *Geophys. J.*
1704 *Int.* 187, 549–563.

1705 Davies, C., Pozzo, M., Gubbins, D., Alfè, D., 2015. Constraints from material prop-
1706 erties on the dynamics and evolution of Earth’s core. *Nat. Geosci.* 8, 678–687.

1707 Davies, C., Pozzo, M., Gubbins, D., Alfè, D., 2018. Partitioning of oxygen between
1708 ferropicliase and Earth’s liquid core. *Geophys. Res. Lett.* 45, 6042–6050.

1709 Davies, C., Pozzo, M., Gubbins, D., Alfè, D., 2020. Transfer of oxygen to Earth’s
1710 core from a long-lived magma ocean. *Earth Planet. Sci. Lett.* 538, 116208.

1711 de Koker, N., Steinle-Neumann, G., Vojtech, V., 2012. Electrical resistivity and
1712 thermal conductivity of liquid Fe alloys at high P and T and heat flux in Earth’s
1713 core. *Proc. Natl. Acad. Sci.* 109, 4070–4073.

1714 Driscoll, P., 2016. Simulating 2 Ga of geodynamo history. *Geophys. Res. Lett.* 43 (11),
1715 5680–5687.

1716 Driscoll, P., Bercovici, D., 2014. On the thermal and magnetic histories of Earth and

- 1717 Venus: Influences of melting, radioactivity, and conductivity. *Phys. Earth Planet.*
1718 *Int.* 236, 36–51.
- 1719 Driscoll, P. E., Du, Z., 2019. Geodynamo conductivity limits. *Geophys. Res. Lett.*
1720 46 (14), 7982–7989.
- 1721 Driscoll, P. E., Wilson, C., 2018. Paleomagnetic biases inferred from numerical dy-
1722 namos and the search for geodynamo evolution. *Frontiers in Earth Science* 6, 113.
- 1723 Du, Z., Boujibar, A., Driscoll, P., Fei, Y., 2019. Experimental constraints on an MgO
1724 exsolution-driven geodynamo. *Geophys. Res. Lett.* 46 (13), 7379–7385.
- 1725 Du, Z., Jackson, C., Bennett, N., Driscoll, P., Deng, J., Lee, K., Greenberg, E.,
1726 Prakapenka, V., Fei, Y., 2017. Insufficient energy from MgO exsolution to power
1727 early geodynamo. *Geophys. Res. Lett.* 4, 2017GL075283.
- 1728 Dumberry, M., 2018. Earth Rotation, Excitation, Core. In: Grafarend, E. (Ed.),
1729 *Encyclopedia of Geodesy*. Springer International Publishing, Cham, pp. 1–5.
- 1730 Dziewonski, A., Anderson, D., 1981. Preliminary Reference Earth Model. *Phys. Earth*
1731 *Planet. Int.* 25, 297–356.
- 1732 Egginis, S., Rudnick, R., McDonough, W., 1998. The composition of peridotites and
1733 their minerals: a laser-ablation ICP–MS study. *Earth Planet. Sci. Lett.* 154 (1-4),
1734 53–71.
- 1735 Fearn, D., Loper, D., 1981. Compositional convection and stratification of Earth’s
1736 core. *Nature* 289, 393–394.
- 1737 Fiquet, G., Auzende, A., Siebert, J., Corgne, A., Bureau, H., Ozawa, H., Garbarino,
1738 G., 2010. Melting of peridotite to 140 gigapascals. *Science* 329, 1516–1518.

- 1739 Fischer, R. A., Campbell, A. J., Ciesla, F. J., 2017. Sensitivities of Earth’s core and
1740 mantle compositions to accretion and differentiation processes. *Earth Planet. Sci.*
1741 *Lett.* 458, 252–262.
- 1742 Fischer, R. A., Cottrell, E., Hauri, E., Lee, K. K., Le Voyer, M., 2020. The carbon
1743 content of Earth and its core. *Proc. Natl. Acad. Sci.* 117 (16), 8743–8749.
- 1744 Fischer, R. A., Nakajima, Y., Campbell, A. J., Frost, D. J., Harries, D., Langen-
1745 horst, F., Miyajima, N., Pollok, K., Rubie, D. C., 2015. High pressure metal-
1746 silicate partitioning of Ni, Co, V, Cr, Si, and O. *Geochimica et Cosmochimica*
1747 *Acta* 167 (Supplement C), 177 – 194.
- 1748 Frost, D., Asahara, Y., Rubie, D., Miyajima, N., Dubrovinsky, L. S., Holzapfel, C.,
1749 Ohtani, E., Miyahara, M., Sakai, T., 2010. Partitioning of oxygen between the
1750 Earth’s mantle and core. *J. Geophys. Res.* 115, B02202.
- 1751 Garaud, P., 2018. Double-diffusive convection at low Prandtl number. *Annual Review*
1752 *of Fluid Mechanics* 50, 275–298.
- 1753 Garnero, E., McNamara, A., Shim, S.-H., 2016. Continent-sized anomalous zones
1754 with low seismic velocity at the base of Earth’s mantle. *Nat. Geosci.* 9, 481–489.
- 1755 Garnero, E. J., Helmberger, D. V., Grand, S. P., 1993. Constraining outermost core
1756 velocity with SmKS waves. *Geophys. Res. Lett.* 20 (22), 2463–2466.
- 1757 Gastine, T., Aubert, J., Fournier, A., 2020. Dynamo-based limit to the extent of a
1758 stable layer atop Earth’s core. *Geophys. J. Int.* 222 (2), 1433–1448.
- 1759 Glane, S., Buffett, B., 2018. Enhanced core-mantle coupling due to stratification at
1760 the top of the core. *Frontiers in Earth Science* 6, 171.

- 1761 Gomi, H., Ohta, K., Hirose, K., Labrosse, S., Caracas, R., Verstraete, V., Hernlund,
1762 J., 2013. The high conductivity of iron and thermal evolution of the Earth's core.
1763 Phys. Earth Planet. Int. 224, 88–103.
- 1764 Greenwood, S., Davies, C., Mound, J., 2021. On the evolution of thermally stratified
1765 layers at the top of Earth's core. Phys. Earth Planet. Int. Preprint available on
1766 arXiv.
- 1767 Gubbins, D., 2003. Thermal core-mantle interactions: theory and observations. In:
1768 Dehant, V., Creager, K., Karato, S., Zatman, S. (Eds.), Earth's core: Dynamics,
1769 Structure, Rotation. Geodynamics Series 31. American Geophysical Union, pp.
1770 162–179.
- 1771 Gubbins, D., Alfè, D., Davies, C., Pozzo, M., 2015. On core convection and the geo-
1772 dynamo: Effects of high electrical and thermal conductivity. Phys. Earth Planet.
1773 Int. 247, 56–64.
- 1774 Gubbins, D., Alfe, D., Masters, G., Price, G., Gillan, M., 2003. Can the Earth's
1775 dynamo run on heat alone? Geophys. J. Int. 155, 609–622.
- 1776 Gubbins, D., Alfè, D., Masters, G., Price, G., Gillan, M., 2004. Gross thermodynam-
1777 ics of two-component core convection. Geophys. J. Int. 157, 1407–1414.
- 1778 Gubbins, D., Davies, C., 2013. The stratified layer at the core-mantle boundary
1779 caused by barodiffusion of Oxygen, Sulphur and Silicon. Phys. Earth Planet. Int.
1780 215, 21–28.
- 1781 Gubbins, D., Thomson, C., Whaler, K., 1982. Stable regions in the Earth's liquid
1782 core. Geophys. J. R. Astr. Soc. 68, 241–251.

- 1783 Gubbins, D., Willis, A., Sreenivasan, B., 2007. Correlation of Earth's magnetic field
1784 with lower mantle thermal and seismic structure. *Phys. Earth Planet. Int.* 162,
1785 256–260.
- 1786 Hardy, C. M., Livermore, P. W., Niesen, J., 2020. Enhanced magnetic fields within
1787 a stratified layer. *Geophys. J. Int.* 222 (3), 1686–1703.
- 1788 Helffrich, G., 2012. How light element addition can lower core liquid wave speeds.
1789 *Geophys. J. Int.*, 1065–1070.
- 1790 Helffrich, G., Ballmer, M. D., Hirose, K., 2018. Core-exsolved SiO₂ dispersal in the
1791 Earth's mantle. *J. Geophys. Res.* 123 (1), 176–188.
- 1792 Helffrich, G., Hirose, K., Nomura, R., 2020. Thermodynamical Modeling of Liquid
1793 Fe-Si-Mg-O: Molten Magnesium Silicate Release From the Core. *Geophys. Res.*
1794 *Lett.* 47 (21), e2020GL089218.
- 1795 Helffrich, G., Kaneshima, S., 2010. Outer-core compositional stratification from ob-
1796 served core wave speed profiles. *Nature* 468, 807–809.
- 1797 Hernlund, J., McNamara, A., 2015. The Core-Mantle Boundary Region. In: Schu-
1798 bert, G. (Ed.), *Treatise on Geophysics Vol. 7*. Elsevier, pp. 461–519.
- 1799 Hirose, K., Labrosse, S., Hernlund, J., 2013. Compositional state of Earth's core.
1800 *Annual Review of Earth and Planetary Sciences* 41, 657–691.
- 1801 Hirose, K., Morard, G., Sinmyo, R., Umemoto, K., Hernlund, J., Helffrich, G.,
1802 Labrosse, S., 2017. Crystallization of silicon dioxide and compositional evolution
1803 of the Earth's core. *Nature* 543 (7643), 99–102.

- 1804 Holme, R., 2007. Large-scale flow in the core. In: Schubert, G. (Ed.), *Treatise on*
1805 *Geophysics* Vol. 8. Elsevier, pp. 107–130.
- 1806 Holme, R., de Viron, O., 2013. Characterization and implications of intradecadal
1807 variations in length of day. *Nature* 499, 202–204.
- 1808 Hsieh, W.-P., Goncharov, A. F., Labrosse, S., Holtgrewe, N., Lobanov, S. S., Chu-
1809 vashova, I., Deschamps, F., Lin, J.-F., 2020. Low thermal conductivity of iron-
1810 silicon alloys at Earth’s core conditions with implications for the geodynamo. *Nat.*
1811 *Commun.* 11 (1), 1–7.
- 1812 Inoue, H., Suehiro, S., Ohta, K., Hirose, K., Ohishi, Y., 2020. Resistivity saturation
1813 of hcp Fe-Si alloys in an internally heated diamond anvil cell: A key to assessing
1814 the Earth’s core conductivity. *Earth Planet. Sci. Lett.* 543, 116357.
- 1815 Irving, J. C., Cottaar, S., Lekić, V., 2018. Seismically determined elastic parameters
1816 for Earth’s outer core. *Science advances* 4 (6), eaar2538.
- 1817 Jackson, A., Livermore, P., 2009. On Ohmic heating in the Earth’s core I: nutation
1818 constraints. *Geophys. J. Int.* 177, 367–382.
- 1819 Jacobson, S., Rubie, D., Herlund, J., Morbidelli, A., Nakajima, M., 2017. Formation,
1820 stratification, and mixing of the cores of Earth and Venus. *Earth Planet. Sci. Lett.*
1821 474, 375–386.
- 1822 Jaupart, C., Labrosse, S., Mareschal, J.-C., 2015. Temperatures, heat and energy in
1823 the mantle of the Earth. In: Schubert, G. (Ed.), *Treatise on Geophysics*, Vol. 7.
1824 Elsevier, Amsterdam, pp. 223–270.
- 1825 Jaupart, E., Buffett, B., 2017. Generation of MAC waves by convection in Earth’s
1826 core. *Geophys. J. Int.* 209 (2), 1326–1336.

- 1827 Kaneshima, S., 2018. Array analysis of SmKS waves and stratification of Earth's
1828 outermost core. *Phys. Earth Planet. Int.* 276, 234–246.
- 1829 Koelemeijer, P., Deuss, A., Ritsema, J., 2017. Density structure of Earth's lowermost
1830 mantle from Stoneley mode splitting observations. *Nat. Commun.* 8 (1), 1–10.
- 1831 Komabayashi, T., 2014. Thermodynamics of melting relations in the system Fe-FeO
1832 at high pressure: Implications for oxygen in the Earth's core. *J. Geophys. Res.*
1833 119 (5), 4164–4177.
- 1834 Konôpková, Z., McWilliams, R., Gómez-Pérez, N., Goncharov, A., 2016. Direct mea-
1835 surement of thermal conductivity in solid iron at planetary core conditions. *Nature*
1836 534, 99–101.
- 1837 Korenaga, J., 2006. Archean geodynamics and the thermal evolution of Earth. *Geo-*
1838 *physical Monograph-American Geophysical Union* 164, 7.
- 1839 Labrosse, S., Hernlund, J., Coltice, N., 2007. A crystallizing dense magma ocean at
1840 the base of the Earth's mantle. *Nature* 450, 866–869.
- 1841 Labrosse, S., Hernlund, J. W., Hirose, K., 2015. Fractional melting and freezing in
1842 the deep mantle and implications for the formation of a basal magma ocean. In:
1843 Badro, J., Walter, M. (Eds.), *The early Earth: accretion and differentiation*. AGU,
1844 Ch. 7, pp. 123–142.
- 1845 Labrosse, S., Poirier, J.-P., Le Moeul, J.-L., 1997. On cooling of the Earth's core.
1846 *Phys. Earth Planet. Int.* 99, 1–17.
- 1847 Labrosse, S., Poirier, J.-P., Le Moeul, J.-L., 2001. The age of the inner core. *Earth*
1848 *Planet. Sci. Lett.* 190, 111–123.

- 1849 Landau, L., Lifshitz, E., 1987. Fluid mechanics (course of theoretical physics, volume
1850 6), 2nd Edition. Pergamon Press.
- 1851 Landeau, M., Aubert, J., Olson, P., 2017. The signature of inner-core nucleation on
1852 the geodynamo. *Earth Planet. Sci. Lett.* 465, 193–204.
- 1853 Landeau, M., Olson, P., Deguen, R., Hirsh, B. H., 2016. Core merging and stratifi-
1854 cation following giant impact. *Nat. Geosci.* 1 (September), 1–5.
- 1855 Laneuville, M., Hernlund, J., Labrosse, S., Guttenberg, N., 2018. Crystallization of a
1856 compositionally stratified basal magma ocean. *Phys. Earth Planet. Int.* 276, 86–92.
- 1857 Lau, H. C., Mitrovica, J. X., Davis, J. L., Tromp, J., Yang, H.-Y., Al-Attar, D., 2017.
1858 Tidal tomography constrains Earth’s deep-mantle buoyancy. *Nature* 551 (7680),
1859 321–326.
- 1860 Lay, T., Hernlund, J., Buffett, B., 2009. Core-mantle boundary heat flow. *Nat.*
1861 *Geosci.* 1, 25–32.
- 1862 Lay, T., Young, C., 1990. The stably-stratified outermost core revisited. *Geophys.*
1863 *Res. Lett.* 71, 2001–2004.
- 1864 Lesur, V., Whaler, K., Wardinski, I., 2015. Are geomagnetic data consistent with
1865 stably stratified flow at the core-mantle boundary? *Geophys. J. Int.*, 929–946.
- 1866 Levy, M., Fernando, H., 2002. Turbulent thermal convection in a rotating stratified
1867 fluid. *Journal of Fluid Mechanics* 467, 19.
- 1868 Li, Y., Vočadlo, L., Alfè, D., Brodholt, J., 2019. Carbon partitioning between the
1869 Earth’s inner and outer core. *J. Geophys. Res.* 124 (12), 12812–12824.

- 1870 Lister, J., Buffett, B., 1998. Stratification of the outer core at the core-mantle bound-
1871 ary. *Phys. Earth Planet. Int.* 105, 5–19.
- 1872 Liu, W., Zhang, Y., Yin, Q.-Z., Zhao, Y., Zhang, Z., 2020. Magnesium partitioning
1873 between silicate melt and liquid iron using first-principles molecular dynamics:
1874 Implications for the early thermal history of the Earth’s core. *Earth Planet. Sci.*
1875 *Lett.* 531, 115934.
- 1876 Long, R., Mound, J., Davies, C., Tobias, S., 2020. Scaling behaviour in spherical shell
1877 rotating convection with fixed-flux thermal boundary conditions. *J. Fluid Mech.*
1878 889.
- 1879 Masters, G., Gubbins, D., 2003. On the resolution of density within the Earth. *Phys.*
1880 *Earth Planet. Int.* 140, 159–167.
- 1881 Mather, J. F., Simitev, R. D., 2020. Regimes of thermo-compositional convection
1882 and related dynamos in rotating spherical shells. *Geophys. Astrophys. Fluid Dyn.*,
1883 1–24.
- 1884 Metman, M. C., Livermore, P. W., Mound, J. E., Beggan, C. D., 2019. Modelling
1885 decadal secular variation with only magnetic diffusion. *Geophysical Journal Inter-*
1886 *national* 219 (Supplement_1), S58–S82.
- 1887 Mittal, T., Knezek, N., Arveson, S. M., McGuire, C. P., Williams, C. D., Jones,
1888 T. D., Li, J., 2020. Precipitation of multiple light elements to power Earth’s early
1889 dynamo. *Earth Planet. Sci. Lett.* 532, 116030.
- 1890 Moffatt, H., Loper, D., 1994. The magnetostrophic rise of a buoyant parcel in the
1891 Earth’s core. *Geophys. J. Int.* 117, 394–402.

- 1892 Monville, R., Vidal, J., Cébron, D., Schaeffer, N., 2019. Rotating double-diffusive
1893 convection in stably stratified planetary cores. *Geophys. J. Int.* 219 (Supple-
1894 ment_1), S195–S218.
- 1895 Mound, J., Davies, C., Rost, S., Aurnou, J., 2019. Regional stratification at the top
1896 of Earth’s core due to core-mantle boundary heat flux variations. *Nat. Geosci.*
- 1897 Mound, J. E., Davies, C. J., 2020. Scaling Laws for Regional Stratification at the
1898 Top of Earth’s Core. *Geophys. Res. Lett.* 47 (16), e2020GL087715.
- 1899 Nakagawa, T., 2011. Effect of a stably stratified layer near the outer boundary in
1900 numerical simulations of a magnetohydrodynamic dynamo in a rotating spherical
1901 shell and its implications for Earth’s core. *Phys. Earth Planet. Int.* 187, 342–352.
- 1902 Nakagawa, T., 2018. On the thermo-chemical origin of the stratified region at the
1903 top of the Earth’s core. *Phys. Earth Planet. Int.* 276, 172–181.
- 1904 Nakagawa, T., 2020. A coupled core-mantle evolution: review and future prospects.
1905 *Progress in Earth and Planetary Science* 7 (1), 1–17.
- 1906 Nakagawa, T., Tackley, P., 2014. Influence of combined primordial layering and
1907 recycled MORB on the coupled thermal evolution of Earth’s mantle and core.
1908 *Geochem. Geophys. Geosys.* 15, 619–633.
- 1909 Nimmo, F., 2015a. Energetics of the core. In: Schubert, G. (Ed.), *Treatise on Geo-*
1910 *physics* 2nd Edn, Vol. 8. Elsevier, Amsterdam, pp. 27–55.
- 1911 Nimmo, F., 2015b. Thermal and compositional evolution of the core. In: Schubert, G.
1912 (Ed.), *Treatise on Geophysics* 2nd Edn, Vol. 9. Elsevier, Amsterdam, pp. 209–219.

- 1913 Nimmo, F., Price, G., Brodholt, J., Gubbins, D., 2004. The influence of potassium
1914 on core and geodynamo evolution. *Geophys. J. Int.* 156, 363–376.
- 1915 Ohta, K., Kuwayama, Y., Hirose, K., Shimizu, K., Ohishi, Y., 2016. Experimental
1916 determination of the electrical resistivity of iron at Earth’s core conditions. *Nature*
1917 534 (7605), 95.
- 1918 Olson, P., Deguen, R., Rudolph, M., Zhong, S., 2015. Core evolution driven by
1919 mantle global circulation. *Phys. Earth Planet. Int.* 243, 44–55.
- 1920 Olson, P., Landeau, M., Reynolds, E., 2017. Dynamo tests for stratification below
1921 the core-mantle boundary. *Phys. Earth Planet. Int.* 271, 1–18.
- 1922 Olson, P., Landeau, M., Reynolds, E., 2018. Outer core stratification from the high
1923 latitude structure of the geomagnetic field. *Frontiers in Earth Science* 6, 140.
- 1924 O’Rourke, J., Korenaga, J., Stevenson, D., 2017. Thermal evolution of Earth with
1925 magnesium precipitation in the core. *Earth Planet. Sci. Lett.* 458, 263–272.
- 1926 O’Rourke, J. G., Stevenson, D. J., 2016. Powering Earth’s dynamo with magnesium
1927 precipitation from the core. *Nature* 529 (7586), 387–389.
- 1928 Ozawa, H., Hirose, K., Mitome, M., Bando, Y., Sata, N., Ohishi, Y., 2008. Chemical
1929 equilibrium between ferropicicase and molten iron to 134 GPa and implications
1930 for iron content at the bottom of the mantle. *Geophys. Res. Lett.* 35, L05308.
- 1931 Patočka, V., Šrámek, O., Tosi, N., 2020. Minimum heat flow from the core and
1932 thermal evolution of the Earth. *Phys. Earth Planet. Int.* 305, 106457.
- 1933 Posner, E. S., Schmickler, B., Rubie, D. C., 2018. Self-diffusion and chemical diffusion

- 1934 in peridotite melt at high pressure and implications for magma ocean viscosities.
1935 *Chemical Geology* 502, 66–75.
- 1936 Pourovskii, L., Mravlje, J., Pozzo, M., Alfe, D., 2020. Electronic correlations and
1937 transport in iron at Earth’s core conditions. *Nat. Commun.* 11 (1), 1–8.
- 1938 Pozzo, M., Alfè, D., 2016. Saturation of electrical resistivity of solid iron at earth’s
1939 core conditions. *SpringerPlus* 5 (1), 1–6.
- 1940 Pozzo, M., Davies, C., Gubbins, D., Alfè, D., 2012. Thermal and electrical conduc-
1941 tivity of iron at Earth’s core conditions. *Nature* 485, 355–358.
- 1942 Pozzo, M., Davies, C., Gubbins, D., Alfè, D., 2013. Transport properties for liquid
1943 silicon-oxygen-iron mixtures at Earth’s core conditions. *Phys. Rev. B* 87, 014110.
- 1944 Pozzo, M., Davies, C., Gubbins, D., Alfè, D., 2019. The FeO Content of Earth’s
1945 Core. *Phys. Rev. X* 9, 041018.
- 1946 Ribe, N., 1998. Spouting and planform selection in the Rayleigh–Taylor instability
1947 of miscible viscous fluids. *J. Fluid Mech.* 377, 27–45.
- 1948 Roberts, P., Scott, S., 1965. On analysis of the secular variation. I. a hydromagnetic
1949 constraint: Theory. *J. Geomagn. Geoelectr.* 17, 137–151.
- 1950 Rubie, D., Nimmo, F., Melosh, H., 2015a. Formation of Earth’s Core. In: Schubert,
1951 G. (Ed.), *Treatise on Geophysics* 2nd Edn, Vol. 9. Elsevier, Amsterdam, pp. 43–79.
- 1952 Rubie, D. C., Frost, D. J., Mann, U., Asahara, Y., Nimmo, F., Tsuno, K., Kegler,
1953 P., Holzheid, A., Palme, H., 2011. Heterogeneous accretion, composition and core-
1954 mantle differentiation of the Earth. *Earth Planet. Sci. Lett.* 301, 31–42.

- 1955 Rubie, D. C., Jacobson, S. A., Morbidelli, A., O'Brien, D. P., Young, E. D., de Vries,
1956 J., Nimmo, F., Palme, H., Frost, D. J., 2015b. Accretion and differentiation of
1957 the terrestrial planets with implications for the compositions of early-formed Solar
1958 System bodies and accretion of water. *Icarus* 248, 89–108.
- 1959 Secco, R. A., 2017. Thermal conductivity and Seebeck coefficient of Fe and Fe-Si
1960 alloys: Implications for variable Lorenz number. *Phys. Earth Planet. Int.* 265,
1961 23–34.
- 1962 Siebert, J., Badro, J., Antonangeli, D., Ryerson, F. J., 2012. Metal-silicate partition-
1963 ing of Ni and Co in a deep magma ocean. *Earth Planet. Sci. Lett.* 321 (Supplement
1964 C), 189 – 197.
- 1965 Sinmyo, R., Hirose, K., Ohishi, Y., 2019. Melting curve of iron to 290 GPa determined
1966 in a resistance-heated diamond-anvil cell. *Earth Planet. Sci. Lett.* 510, 45–52.
- 1967 Solomatov, V., 2015. Magma oceans and primordial mantle differentiation. In: Schu-
1968 bert, G. (Ed.), *Treatise on Geophysics 2nd Edn*, Vol. 10. Elsevier, Amsterdam, pp.
1969 81–104.
- 1970 Souriau, A., Calvet, M., 2015. Deep Earth structure – the Earth's cores. In: Schu-
1971 bert, G., Romanowicz, B., Dziewonski, A. (Eds.), *Treatise on geophysics*. Vol. 1.
1972 Elsevier, Amsterdam, Ch. 23, pp. 725–757.
- 1973 Stevenson, D., 1987. Limits on lateral density and velocity variations in the Earth's
1974 outer core. *Geophys. J. Int.* 88, 311–319.
- 1975 Stixrude, L., de Koker, N., Sun, N., Mookherjee, M., Karki, B. B., 2009. Thermo-
1976 dynamics of silicate liquids in the deep Earth. *Earth Planet. Sci. Lett.* 278 (3-4),
1977 226–232.

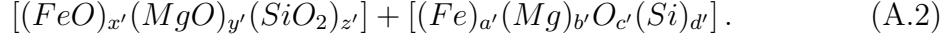
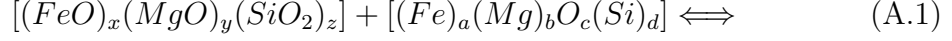
- 1978 Suer, T.-A., Siebert, J., Remusat, L., Menguy, N., Fiquet, G., 2017. A sulfur-poor
1979 terrestrial core inferred from metal-silicate partitioning experiments. *Earth Planet.*
1980 *Sci. Lett.* 469 (Supplement C), 84 – 97.
- 1981 Takafuji, N., Hirose, K., Mitome, M., Bando, Y., 2005. Solubilities of O and Si in
1982 liquid iron in equilibrium with (Mg,Fe)SiO₃ perovskite and the light elements in
1983 the core. *Geophys. Res. Lett.* 32 (6), L06313.
- 1984 Takehiro, S.-i., Lister, J. R., 2001. Penetration of columnar convection into an outer
1985 stably stratified layer in rapidly rotating spherical fluid shells. *Earth Planet. Sci.*
1986 *Lett.* 187 (3-4), 357–366.
- 1987 Tang, F., Taylor, R. J., Einsle, J. F., Borlina, C. S., Fu, R. R., Weiss, B. P., Williams,
1988 H. M., Williams, W., Nagy, L., Midgley, P. A., et al., 2019. Secondary magnetite
1989 in ancient zircon precludes analysis of a Hadean geodynamo. *Proc. Natl. Acad.*
1990 *Sci.* 116 (2), 407–412.
- 1991 Tarduno, J., Cottrell, R., Bono, R., Oda, H., Davis, W., Fayek, M., van't Erve,
1992 O., Nimmo, F., Huang, W., Thern, E., et al., 2020. Paleomagnetism indicates
1993 that primary magnetite in zircon records a strong Hadean geodynamo. *Proc. Natl.*
1994 *Acad. Sci.* 117 (5), 2309–2318.
- 1995 Tarduno, J., Cottrell, R., Watkeys, M., Hofmann, A., Doubrovine, P., Mamajek, E.,
1996 Liu, D., Sibeck, D., Neukirch, L., Usui, Y., 2010. Geodynamo, solar wind, and
1997 magnetopause 3.4 to 3.45 billion years ago. *Science* 327, 1238–1240.
- 1998 Tarduno, J. A., Cottrell, R. D., Davis, W. J., Nimmo, F., Bono, R. K., 2015. A
1999 Hadean to Paleoproterozoic geodynamo recorded by single zircon crystals. *Science*
2000 349, 521–524.

- 2001 Tauxe, L., Yamazaki, T., 2015. 5.13-paleointensities. In: *Treatise on Geophysics*.
2002 Elsevier, pp. 461–509.
- 2003 Tilgner, A., 2015. Rotational Dynamics of the Core. In: Schubert, G. (Ed.), *Treatise*
2004 *on Geophysics*, 8.07. Elsevier, Amsterdam, pp. 183–212.
- 2005 Tsuno, K., Frost, D. J., Rubie, D. C., 2013. Simultaneous partitioning of silicon
2006 and oxygen into the Earth’s core during early Earth differentiation. *Geophys. Res.*
2007 *Lett.* 40, 66–71.
- 2008 Turner, J., 1973. *Buoyancy effects in fluids*. Cambridge University Press.
- 2009 Umemoto, K., Hirose, K., 2020. Chemical compositions of the outer core examined
2010 by first principles calculations. *Earth Planet. Sci. Lett.* 531, 116009.
- 2011 van Tent, R., Deuss, A., Kaneshima, S., Thomas, C., 2020. The signal of outermost-
2012 core stratification in body-wave and normal-mode data. *Geophys. J. Int.* 223 (2),
2013 1338–1354.
- 2014 Whaler, K. A., 1980. Does the whole of the Earth’s core convect? *Nature* 287,
2015 528–530.
- 2016 Whaler, K. A., 1986. Geomagnetic evidence for fluid upwelling at the core-mantle
2017 boundary. *Geophys. J. R. Astr. Soc.* 86, 563–588.
- 2018 Wicht, J., Sanchez, S., 2019. Advances in geodynamo modelling. *Geophys. Astrophys.*
2019 *Fluid Dyn.* 113 (1-2), 2–50.
- 2020 Williams, Q., 2018. The thermal conductivity of Earth’s core: a key geophysical
2021 parameter’s constraints and uncertainties. *Annual Review of Earth and Planetary*
2022 *Sciences* 46, 47–66.

- 2023 Wong, J., Davies, C. J., Jones, C. A., 2021. A regime diagram for the slurry F-layer
2024 at the base of Earth’s outer core. *Earth Planet. Sci. Lett.* 560, 116791.
- 2025 Xiong, Z., Tsuchiya, T., Taniuchi, T., 2018. Ab initio prediction of potassium parti-
2026 tioning into Earth’s core. *J. Geophys. Res.* 123 (8), 6451–6458.
- 2027 Xu, J., Zhang, P., Haule, K., Minar, J., Wimmer, S., Ebert, H., Cohen, R., 2018.
2028 Thermal conductivity and electrical resistivity of solid iron at Earth’s core condi-
2029 tions from first principles. *Phys. Rev. Lett.* 121 (9), 096601.
- 2030 Yan, C., Stanley, S., 2018. Sensitivity of the geomagnetic octupole to a stably strat-
2031 ified layer in the Earth’s core. *Geophys. Res. Lett.* 45 (20), 11–005.
- 2032 Zhang, K., 1992. Convection in a rapidly rotating spherical shell at infinite Prandtl
2033 number: transition to vacillating flows. *Phys. Earth Planet. Int.* 72, 236–248.
- 2034 Zhang, Y., Hou, M., Liu, G., Zhang, C., Prakapenka, V. B., Greenberg, E., Fei, Y.,
2035 Cohen, R., Lin, J.-F., 2020. Reconciliation of experiments and theory on transport
2036 properties of iron and the geodynamo. *Phys. Rev. Lett.* 125 (7), 078501.

2037 **Appendix A. Mass Balance Between the Core and Magma Ocean**

2038 We implement three differences compared to the algorithm presented in Rubie
2039 et al. (2011): 1) Mg replaces Ni in the reaction set; 2) distribution coefficients for
2040 Si and Mg are defined by dissociation reactions rather than exchange reactions. We
2041 start by considering the reaction



which is essentially the reaction considered by Rubie et al. (2011), ignoring elements that do not partition and replacing Ni with Mg. Mass conservation demands

$$a' = x + a - x', \quad (A.3)$$

$$b' = y + b - y', \quad (A.4)$$

$$c' = x + y + 2z + c - x' - y' - 2z', \quad (A.5)$$

$$d' = z + d - z'. \quad (A.6)$$

The distribution coefficients are given in this notation by

$$K_D^O = \frac{c_{FeCO}}{c_{FeO}} = \frac{a'c'}{x'(a' + b' + c' + d')^2} \quad (A.7)$$

$$K_D^{Mg} = \frac{c_{MgCO}}{c_{MgO}} = \frac{b'c'}{y'(a' + b' + c' + d')^2} \quad (A.8)$$

$$K_D^{Si} = \frac{c_{SiCO}^2}{c_{SiO_2}} = \frac{d'(c')^2}{z'(a' + b' + c' + d')^3}. \quad (A.9)$$

2042 The procedure of Rubie et al. (2011) starts by guessing a value for x' , which gives
 2043 a' from equation (A.3). Next y' is obtained from the definition of K_D^{Mg} . We note
 2044 that

$$\frac{K_D^{Mg}}{K_D^O} = \frac{x'b'}{y'a'}, \quad (A.10)$$

2045 which is the same result as equation S12 in Rubie et al. (2011) despite the fact
 2046 that we are considering different reactions. This arises since the FeO and MgO

2047 concentrations in the silicate are determined by the amount of Fe and Mg respectively.
 2048 Equation (A.10) allows us to determine y' from an initial guess at x' . Using the
 2049 definitions of b' and y' gives

$$y' = \frac{x'(y + b)}{(x + a - x')K_D^{Mg}/K_D^O + x'}. \quad (\text{A.11})$$

2050 and hence b' is also determined from equation (A.4).

To obtain z' substitute equations (A.5) and (A.6) into the definition of K_D^O/K_D^{Si} ,
 obtaining

$$\frac{K_D^O}{K_D^{Si}} = \frac{a'c'z'(a' + b' + c' + d')}{x'd'(c')^2}, \quad (\text{A.12})$$

$$= \frac{a'z'(a' + b' + x + y + 3z + c - x' - y' - 3z' + d)^2}{x'(z + d - z')(x + y + 2z + c - x' - y' - 2z')}. \quad (\text{A.13})$$

Defining

$$\alpha = z + d, \quad (\text{A.14})$$

$$\gamma = a' + b' + x + y + 3z + c - x' - y' + d, \quad (\text{A.15})$$

$$\sigma = x + y + 2z + c - x' - y', \quad (\text{A.16})$$

2051 we can write

$$\frac{K_D^O}{K_D^{Si}} = \frac{a'z'(\gamma - 3z')}{x'(\alpha - z')(\sigma - 2z')}, \quad (\text{A.17})$$

2052 which turns in to a quadratic equation for z' :

$$(z')^2 \left[3a' + 2x' \frac{K_D^O}{K_D^{Si}} \right] - z' \left[(2\alpha x') + x'\sigma \right] \frac{K_D^O}{K_D^{Si}} + a'\gamma + \frac{K_D^O}{K_D^{Si}} x' \alpha \sigma = 0. \quad (\text{A.18})$$

2053 We note here an analytical solution for the special case where exchange of Fe and

2054 Si is disallowed. We require that

$$x = x', a = a', z = z', d = d'. \quad (\text{A.19})$$

The mass balance equations reduce to

$$b' = y + b - y' \quad (\text{A.20})$$

$$c' = y - y' + c, \quad (\text{A.21})$$

while the distribution coefficients are

$$K_D^O = \frac{ac'(x + y' + z)}{x(a + b' + c' + d)^2}, \quad (\text{A.22})$$

$$K_D^{Mg} = \frac{b'c'(x + y' + z)}{y'(a + b' + c' + d)^2}, \quad (\text{A.23})$$

$$K_D^{Si} = \frac{d(c')^2(x + y' + z)}{z(a + b' + c' + d)^3}, \quad (\text{A.24})$$

$$\frac{K_D^{Mg}}{K_D^O} = \frac{xb'}{a(y + b - b')}, \quad (\text{A.25})$$

$$\frac{K_D^O}{K_D^{Si}} = \frac{az(a + b' + c' + d)}{xdc'}. \quad (\text{A.26})$$

2055 From the first ratio we find a solution for b' as

$$b' = \frac{a(y + b)K_{Mg}/K_O}{x + aK_{Mg}/K_O} \quad (\text{A.27})$$

2056 and from the second ratio we get

$$b' = \left[az(a + c - b + d) - \frac{K_O}{K_{Si}}xd(c - b) \right] \left(\frac{K_O}{K_{Si}}xd - 2az \right). \quad (\text{A.28})$$

²⁰⁵⁷ Equating these two expressions gives a constraint on the input compositions.